High-Speed Conducting Polymer Actuators for Thin, Flexible Vibrotactile Displays:

Fabrication, Electro-chemo-mechanical Characterization, and Feasibility

by

Freya Hik

B.Sc., University of Alberta, Edmonton, 2018

A THESIS SUBMITTED IN PARTIAL FULFILLMENT OF

THE REQUIREMENTS FOR THE DEGREE OF

MASTER OF APPLIED SCIENCE

in

THE FACULTY OF GRADUATE AND POSTDOCTORAL STUDIES

(Biomedical Engineering)

THE UNIVERSITY OF BRITISH COLUMBIA

(Vancouver)

June 2022

The following individuals certify that they have read, and recommend to the Faculty of Graduate and Postdoctoral Studies for acceptance, the thesis entitled:

High-speed conducting polymer actuators for thin, flexible vibrotactile displays: fabrication, electro-chemo-mechanical characterization, and feasibility

submitted by Freya Hik in partial fulfilment of the requirements for

the degree of Master of Applied Science

in Biomedical Engineering

Examining Committee:

John D. W. Madden, Professor, Electrical and Computer Engineering, UBC
Supervisor

Dena Shahriari, Professor, Biomedical Engineering, UBC
Supervisory Committee Member

Karon MacLean, Professor, Computer Science, UBC
Supervisory Committee Member

Abstract

Fast-acting, thin, flexible, bending-type actuators are an emerging technology for applications, such as in tactile feedback devices. Conducting polymer (CP) tri-layer actuators are a category of electroactive material that exhibit relatively high strain (>1 %), high work density, operate at low voltages (< 1 V), are thin (microns), and biocompatible. Strain is proportional to charge in the CP; therefore, the faster charge moves through of the system, the faster the tri-layer actuates. Our objective was to optimize the electrical, ionic, and material properties of PEDOT:PSS/PVDF/PEDOT:PSS actuators to increase charge storage and transfer capabilities. The goal was to increase the actuation speed of these devices, such that they achieved sufficient displacements and forces at physiologically relevant frequencies for vibrotactile feedback. We hypothesized that we could optimize the electro-chemo-mechanical properties of the PEDOT:PSS-based actuators using polar solvents and ionic liquid, to increase actuation speed. We soaked samples in methanol, methanol mixed with EMITFSI (50%v/v), ethylene glycol, ethylene glycol mixed with EMITFSI (50%v/v), or dimethyl sulfoxide.

These treatments improved both electrical and ionic conductivity of PEDOT:PSS. Our results suggested that diffusion of ions through the CP layers was the largest source of impedance. Therefore, ionic resistance dictated the RC time constants. Treatment with polar solvent combined with ionic liquid resulted in the largest actuation speed, with a cut-off frequency of 4-Hz. We measured resonant frequency at ~300-Hz for a 5-mm long beam treated with MeOH and EMITFSI.

We then investigated designs for vibrotactile displays. We applied a viscoelastic model to predict the skin deflection our actuators achieved. Results showed that force generation was the primary limiting factor. Free beam deflection exceeded the frequency-dependent minimum perception threshold by up to two orders of magnitude. However, this deflection decreased

substantially when the actuators were mechanically impeded by the fingertip. The model predicted that our actuators just barely exceeded the absolute threshold of human perception on the hand. In future work we plan to further optimize the fabrication process and design of these conducting polymer tactors for applications such as in non-invasive biomedical, wearable, and communication devices.

Lay Summary

Vibration as a form of communication from computers to humans, generated by devices called "vibrotactile actuators", is a common mechanism that has been incorporated into biomedical, wearable, and communication devices. Current technologies typically use rigid, bulky materials, and designs. In this work we developed high-speed, thin, flexible artificial muscle from a polymer material that is intrinsically conductive, both electrically and ionically. Human skin is highly sensitive and can detect displacements as small as 100 nm at frequencies between 100 to 200 Hz. We showed that by increasing the speed of our devices, we could generate vibrations within this frequency range above the minimum perception threshold. This dissertation describes the design, characterization, and analysis of this technology.

Preface

This research serves as an extension of the work previously conducted by Dr. Saeedeh Ebrahimi Takalloo on conducting polymer tri-layer actuators and was conducted under the supervision of Dr. John D. W. Madden. This work was largely conducted independently with contributions from Dr. Saeedeh Ebrahimi Takalloo and Erfan Taatizdeh (PhD candidate in the school of biomedical engineering at the University of British Columbia). Dr. Madden provided technical guidance and editorial feedback.

In Chapter 1, the literature review on conducting polymer tri-layer actuators was conducted by Betty Cai (UBC APSC, SBME). She conducted this research over the summer of 2020 and created Figure 1-3.

In Chapter 2, Dr. Saeid Soltanian (Research Associate and manager of CFET, UBC) provided technical support for all instruments used in the Centre for Flexible Electronics and Textiles (mainly the spray coater and profilometer). All fabrication and characterization processes were carried out by the author. XPS experiments were carried out by the author, with the help of Dr. Sebastián Madrano (Shared Facility Manager of AMPEL, UBC). Dr. Giorgio Levy de Castro (Research Associate, AMPEL, UBC) provided guidance with analysis of these data; however, development of the optimization model used in this work was done by the author.

In Chapter 3, the Actuatool model used to predict force generation was previously developed and described by Dr. Saeedeh Ebrahimi Takalloo as part of her PhD dissertation (UBC, ECE). Experimental data measuring blocking force and validation of the model was also collected and performed by Dr. Saeedeh Takalloo. Analysis of the results generated specifically for the tri-layer properties described in this work was carried out by the author.

In Chapter 4, design of the vibrotactile displays was conducted primarily by the author. Dr. Chan Ge (Postdoctoral Researcher, UBC) developed the laser cutting recipe and performed this fabrication step. Erfan Taatizdeh assisted with 3D printing the tactor holders. Sadan Wani (UBC, MASc, SBME), Jian (Johnson) Gao (UBC, MASc, SBME), Erfan Taatizdeh, Dr. John Madden, and Dr Karon MacLean (Professor, Dept. of Computer Science, UBC) provided feedback on the viability of the described vibrotactile displays.

Part of the research described in Chapter 2 and 3 on the electro-chemo-mechanical behavior of PEDOT:PSS/PVDF/PEDOT:PSS tri-layer actuators treated with methanol and/or ionic liquid was published in the conference proceedings and presented by the author at the Electroactive Polymer Actuators and Devices SPIE conference (Long Beach, CA, 2022). The author collected all the data and wrote the manuscript for this publication:

Freya Hik, Erfan Taatizadeh, Saeedeh Ebrahimi Takalloo, John Madden, "The effects of improved conductivity on actuation," Proc. SPIE 12042, Electroactive Polymer Actuators and Devices (EAPAD) XXIV, 1204204 (20 April 2022); https://doi.org/10.1117/12.2615228

Table of Contents

List of Tables

List of Figures

List of Abbreviations

Ag/AgCl	Silver/silver chloride
AR	Augmented reality
DCA	1-allyl-3-methylimidazolium dicyanamide
AMPEL	Advanced materials and process engineering laboratory
AR	Augmented reality
Au	Gold
CFET	Centre for flexible electronics and textiles
CNS	Central nervous system
CP	Conducting polymer
CV	Cyclic voltammetry
DEA	Dielectric elastomer
DEM	Diffusive elastic metal
DI	Deionized water
DMSO	Dimethyl sulfoxide
EAP	Electroactive polymer
EDOT	3,4-ethylenedioxythiophene
EG	Ethylene glycol
EIS	Electrochemical impedance spectroscopy
EMIM DCA	1-ethyl-3-methylimidazolium dicyanamide
EMIM TCB	1-Ethyl-3-methylimidazolium tetracyanoborate
EMIM TFSI	Ethyl-3-methylimidazolium bis(trifluoromethylsulfonyl)imide
ERM	Eccentric rotating mass motor
EW	Electrochemical window
GIWAXS	Grazing-incidence wide-angle x-ray scattering
GUI	Graphical user-interface
H_2SO_4	Sulfuric acid
IL	Ionic liquid
ITO	Indium tin oxide

KOH	Potassium hydroxide
LiTFSI	Lithium bis(trifluoromethanesulfonyl)imid
LRA	Linear resonant actuator
MC	Meissner corpuscle
MeOH	Methanol
Na4SO4	Sodium sulfate
PANi	Polyaniline
PC	Pacinian corpuscle
PDMS	Polydimethylsiloxane
PEDOT	Poly(3,4-ethylenedioxythiophene)
PEO	Poly(ethylene oxide)
PEO:NBR	Poly(ethylene oxide): nitrile butadiene rubber
Ppy	Polypyrrole
PSS	Polystyrene sulfonate
Pt	Platinum
PVC	Polyvinyl chloride
PVDF	Polyvinylidene fluoride
RA	Rapid adapting
RFID	Radio frequency identification devices
SA	Slow adapting
Si	Silicon
SIBS	Poly(styrene-b-isobutylene-b-styrene)
SOP	Standard operating procedure
TMR	Targeted muscle reinnervation
UBC	University of British Columbia
UV	Ultraviolet
VR	Virtual reality
XPS	X-ray photoelectron spectroscopy
XRD	X-ray diffraction

Acknowledgements

I would first like to thank my supervisor, Dr. John Madden, for his support and mentorship. I feel incredibly lucky to have had the opportunity to work with him. He has both challenged and inspired me with his scientific curiosity that culminated in many interesting discussions throughout the last two years. I also want to thank Dr. Saeedeh Ebrahimi Takalloo, whose guidance, especially at the beginning of my degree, set me up for successful research project. Erfan Taatizadeh has been a wonderful colleague and teammate as we worked to develop our actuators together. I would also like to thank the rest of Molecular Mechatronics lab for creating a wonderful work environment. Every day I come into work I am amazed at the innovation and creativity on such a wide range of topics, from sensors to batteries, this group achieves.

Next, I would like to acknowledge the enduring support of my family. My parents have always encouraged me in my academic pursuits; I would not be where I am today without their love and support. I also want to thank my partner, Tryggvi, who shared many highs and lows of graduate school with me during a global pandemic in our basement home office. He never hesitated to pull out the whiteboard marker to help me think through a math, physics, or Matlab problem. I wish him the best of luck as he also wraps up his master's thesis shortly.

Dedication

This dissertation is dedicated to my Grandpa (Pop-pop), Bill Hik. He graduated from Electrical Engineering from UBC in 1957 and worked as a Professional Engineer for his entire career, pioneering electro-mechanical automation. He was so clearly passionate for his chosen profession and incredibly proud of me when I chose to follow in his footsteps. His patience was unwavering as he worked through my elementary school math books with me, which was perhaps the genesis of my interest in STEM. I feel incredibly lucky that he got to present me with my iron ring in 2018. Although he is no longer here today, I know he would be incredibly proud of my accomplishments and wish the best for me in my future endeavors, whatever those may be.

Chapter 1: Introduction

In this chapter, we first outline the motivation, aims and hypothesis that drive this work. Next, we provide an overview of conducting polymer (CP) actuators as a category of artificial muscle and alternative to conventional actuators. We then describe the electro-chemo-mechanical mechanisms that drive actuation of CP tri-layer actuators. Previously developed models describe the charge storage and actuation mechanisms that allow use to predict rate limiting factors impeding high-speed actuation of tri-layer actuator devices. These mechanisms correlate to characteristic RC time constants and cut-off frequencies. Next, we provide a brief literature review on previous developments of CP tri-layer actuators. We also provide an overview of conducting polymers, with a focus on specifically poly(3,4-ethylenedioxythiophene) polystyrene sulfonate (PEDOT:PSS), which is the active material we use in our technology. Previous work has investigated how to increase the electrical conductivity of PEDOT:PSS; we provide a brief overview of this literature and how it fits into the context of our work on CP tri-layer actuators. Finally, we discuss the scope of work covered in this thesis and give a brief overview of the layout of this thesis.

1.1 Motivation

Fast-acting, thin, flexible, bending-type actuators are a promising emerging technology for applications such as tactile feedback [8, 9], microgrippers [10], image scanning catheters [11], CP driven textiles [12], micro-injection and pump systems [13, 14], micro-autofocus lenses [15], robotic fish [16], and controllable drug delivery systems [17]. Actuators are devices that convert external stimuli – such as electrical, thermal, or optical energy – into mechanical energy [18]. Conventional actuators are typically composed of bulky, rigid components, such as motors, gear boxes, and pneumatic or hydraulic piston systems. Artificial muscles are a class of materials and

devices that reversibly generate actuation (i.e., contraction, expansion, or rotation) within one component [19]. Electroactive polymers (EAP) actuators exhibit muscle-like properties and so fall into this category of artificial-muscle. They serve as a potential alternative to conventional actuators due to their lightweight, compliant properties, high work density, biocompatibility, ability to operate in air and fluid, lack of need for external gears or motors, and simple fabrication [20-22].

CP tri-layer actuators are a category of EAP actuators that show promise for many of these applications. However, they suffer challenges of low bandwidth (<1 Hz). Recent work by Maziz *et al.* showed that miniaturizing CP tri-layer actuators increases speed, but sacrifices absolute displacement amplitude [23]. In our research, we show methods of chemically increasing the electronic and ionic conductivities of the PEDOT:PSS to improve the high-speed capabilities of these actuators. Applications such as vibrotactile displays and active scanning catheters require thin, flexible, biocompatible materials.

In this thesis, we specifically explore vibrotactile feedback applications for haptic devices, in depth (Chapter 4). Figure 1-1 illustrates the development of conducting polymer tri-layer actuators described in this thesis for the high-speed application of vibrotactile displays. We initially characterized the electrochemical and mechanical performance of our chemically treated actuators. We then analyzed if the improved charging speed of PEDOT:PSS allowed us to design vibrotactile displays that exceeded the minimum skin displacement and force thresholds required for human perception. The energy flow diagram shows how adjusting different properties of PEDOT:PSS results in benefits and trade-offs, which we need to specifically consider and optimize for our intended application.

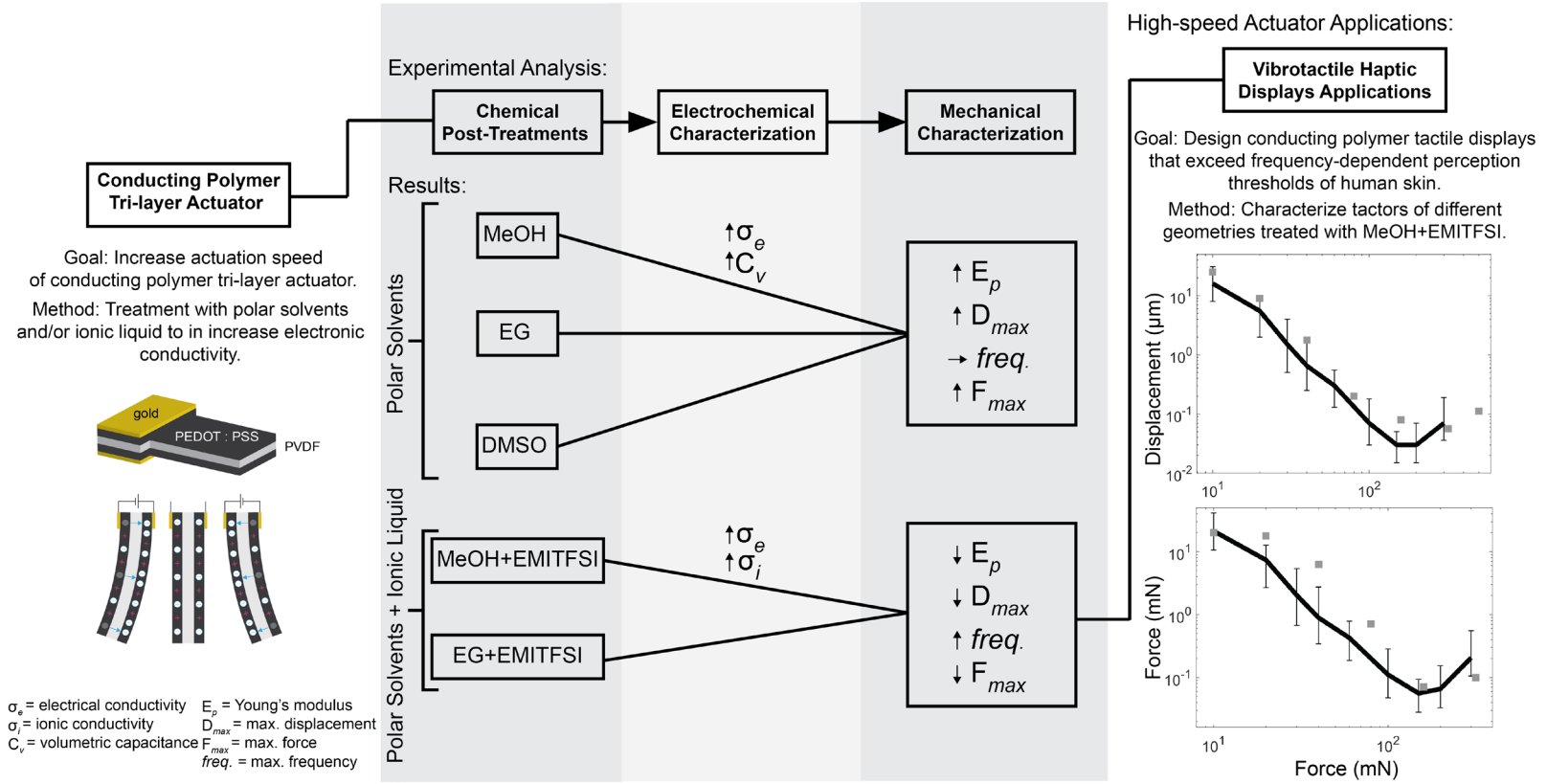

Figure 1-1 Energy flow diagram of the work completed in this thesis. PEDOT:PSS/PVDF/PEDOT:PSS tri-layer actuators were post-treated with the following polar solvents and/or ionic liquid: methanol (MeOH), ethylene glycol (EG), dimethyl sulfoxide (DMSO), methanol mixed with Ethyl-3-methylimidazolium bis(trifluoromethylsulfonyl)imide (50% v/v; MeOH+EMITFSI), or ethylene glycol mixed with EMITFSI (50% v/v; EG+EMITFSI). Actuators were electro-chemo-mechanically characterized to identify how improving conductivity increased strain, blocking force, and speed; these results are described in Chapter 2 (electrochemical characterization) and Chapter 3 (mechanical characterization). High speed actuators were designed as vibrotactile displays to exceed the minimum force and perception thresholds of glabrous skin on the fingertip. Perception thresholds, shown in panel 3 frequency response graphs, were previously described by Brisben *et al.* (1999; black line) and Israr *et al.* (2006; grey points). Vibrotactile actuator characterization is described in Chapter 4.

1.2 Objective

The overall objective of this work was to optimize the electrical, ionic, and material properties of PEDOT:PSS to increase the charge storage capabilities of the material, and reduce the overall impedance of the system. The end goal was to increase the actuation speed of these CP tri-layer devices such that they achieved sufficient displacements and forces at physiologically relevant frequencies.

1.2.1 Specific Aims

This project includes:

1. Electrochemical characterization of the PEDOT:PSS/PVDF/PEDOT:PSS tri-layer actuators following chemical post-treatment with polar solvents and ionic liquid to determine how these processes affect charge storage and time constants related to charging/discharging of the active material (Chapter 2).
2. Mechanical characterization of PEDOT:PSS/PVDF/PEDOT:PSS tri-layer actuators following chemical post-treatment with polar solvents and ionic liquid to determine how these processes affect the Young's modulus, actuation-frequency response, and blocking force (Chapter 3).
3. Investigation of the chemically post-treated PEDOT:PSS/PVDF/PEDOT:PSS tri-layer actuators for the specific application of vibrotactile displays, to assess how we can design thin flexible CP tactors that exceed the required displacement, force, and frequency thresholds for perception (Chapter 4).

1.3 Hypothesis

We hypothesize that we will be able to optimize the electro-chemo-mechanical properties of the conducting polymer actuators, such that we can increase actuation speed and incorporate this technology into viable vibrotactile displays.

1.4 Background

Conducting Polymers (CPs) are a category of ionic EAPs that transduce electrical energy into mechanical energy through electrochemical processes. Baughman first proposed the idea of using CP to convert electrochemical energy to mechanical energy in 1990 [24]. Subsequently, most of the early research on CP actuators examined single-layer or bi-layer structures, which require a liquid electrolyte environment to operate [25].

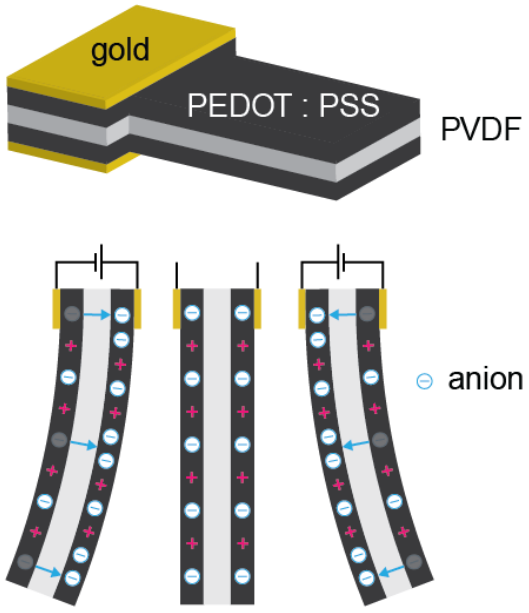

Figure 1-2 Schematic of the actuation mechanism for a PEDOT:PSS/PVDF/PEDOT:PSS tri-layer actuator. These devices are composed of two layers of PEDOT:PSS (dark grey) that sandwich a porous PVDF membrane (light grey). Under the influence of a potential difference, charges diffuse through the structure, which causes the structure to bend. Red '+' and blue '-' symbols represent these charges. In the closed circuit configurations, the faded negative charge symbols indicate that those ions have left one electrode and migrated to the counter electrode.

More recently, tri-layer structures have drawn particular interest due to their ability to operate in air [8, 21, 22, 26-32]. These tri-layer actuators consist of two layers of electronically and ionically conducting polymer (CP), such as Polypyrrole (PPy), Polyaniline (PANi), or PEDOT:PSS. These CP electrodes sandwich an ionically conducting and electronically insulating layer, such as a solid polymer electrolyte, poly(ethylene oxide): nitrile butadiene rubber (PEO:NBR) or a porous polyvinylidene fluoride (PVDF) membrane. When operated electrochemically, the whole structure is charged like a capacitor, and a reversible redox reaction takes place in the two CP layers. This leads to the transport of ions from one electrode to the other through the separator. As a result, the CP electrode with excess ions expands, while the counter electrode actively contracts, due to a lack of ions. This causes an internally induced bending moment, allowing for displacement along the length of the device. Figure 1-2 schematically depicts this actuation mechanism. In this image, red '+' and blue '-' symbols represent the balanced positive and negative charges. In the closed-circuit configurations, the faded negative charge symbols indicate that those ions have left one electrode and migrated to the counter electrode. These devices have a 100-200 μm thick planar configuration and experience up to 10 % strain [33, 34]. They are also fabricated from low-cost materials and have a low actuation voltage (<2 V). Challenges with these CP actuators include lack of large force generation capabilities, high power requirements, and slow speeds (due to low cut-off frequencies) [8, 22]. The focus of this research is to increase the speed of tri-layer conducting polymer actuators fabricated from PEDOT:PSS.

1.5 Fundamental Principles of Actuation

Madden *et al.* developed an analytical electro-chemo-mechanical model based on the diffusive elastic metal (DEM) to describe the charging process of tri-layer actuators that results in actuation [35]. This model likens the actuators to a 2D transmission line and links mechanical

deformation through the experimentally derived strain-to-charge ratio (α) [3, 8, 28, 32, 36, 37]. Figure 1-3 shows the equivalent circuit for this model. Here, an RC equivalent circuit explains the diffusion of ions through the electrode and separator thicknesses and the electrical resistance along the length of the device. Successive capacitors (C_V) and ionic resistors (R_{iP}), electrical resistance (R_{eP}) in series define the diffusion line. Separator resistance (R_g) and contact resistance (R_c) also contribute to the overall resistance of the system. Leakage resulting in short circuit resistance (R_{short}) between the CP layers is also possible. Double layer capacitance (C_{dl}) forms at the interfaces between CP electrode and electrolyte.

1.5.1 Cut-off Frequency

Actuation speed depends on rate of charge insertion, which is most significantly determined by impedances resulting from the following:

(1) Resistance to the transport of electrons along the length of the CP layer (R_{eP}).
(2) Resistance to the transport of ions through the thickness of the CP layer (R_{iP}).
(3) Resistance to the transport of ions through the thickness of the separator (R_g).
(4) Capacitance due to charging of the electrical double-layer at the surface of each electrode (C_{dl}).
(5) volumetric capacitance due to ion storage within the material (C_V)
(6) contact resistance (R_C)
(7) leakage (R_{short})

These mechanisms establish time constants, described by Equations (1-1)-(1-3), and limit performance:

$$\tau_e = R_{eP}C = C_V \frac{L^2}{\sigma_e}, \tag{1-1}$$

$$\tau_{iP} = R_{iP}C = C_V \frac{h_P^2}{\sigma_{iP}}, \tag{1-2}$$

$$\tau_g = R_g C = C_V \frac{h_P h_g}{2\sigma_g}, \qquad (1\text{-}3)$$

where τ_e is the electrical time constant correlated to charging along the length (L) of the device, τ_{iP} is the diffusion time constant correlated to migration of ions through the thickness of the CP electrodes (h_P), and τ_g refers to the diffusion time constant of ions through the thickness of the separator layer (h_P). The parameters σ_e, σ_{iP}, and σ_g refer to the electrical polymer ionic and separator ionic conductivities, respectively.

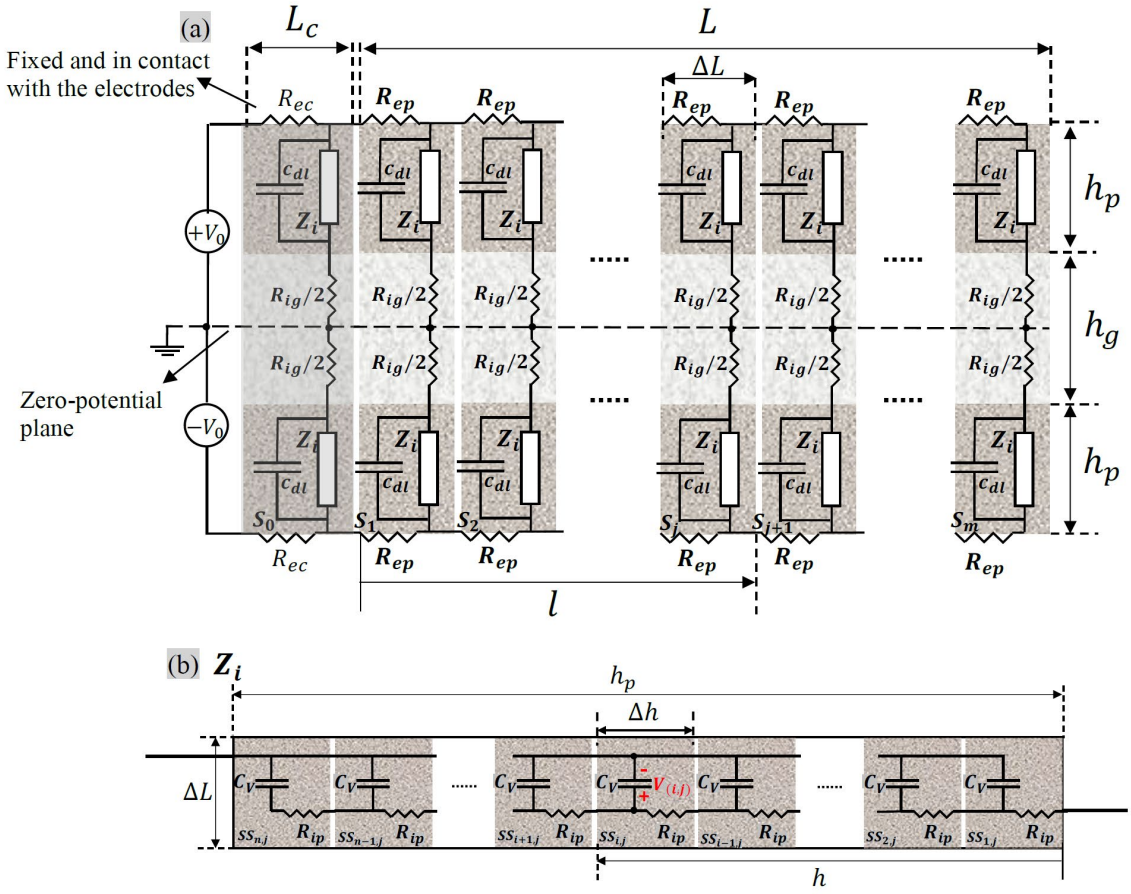

Figure 1-3 a) Equivalent transmission line circuit used to model the electrochemical behavior along the length and through the thickness of the CP tri-layer actuators. The initial faded segment closest to the power source is fixed between two electrodes. The neutral plane (dashed line) has zero potential, since we assume the tri-layer is symmetric. b) Equivalent RC transmission line circuit of the element Z_i, which models the diffusion of ions through the though the thickness of the CP layers (Information obtained from © 2019 Ebrahimi T. UBC [3]).

The RC time constant of the whole system is inversely proportional to the cut-off frequency (f_c). This refers to the frequency at which the energy flowing through the system begins to decrease such that each CP layer does not have sufficient time to fully charge/discharge, and is expressed by Equation (1-4):

$$f_c = \frac{1}{2\pi\tau}. \tag{1-4}$$

A major challenge to developing fast actuating CP tri-layers is reducing the impedance of the system, such that we achieve high f_c. This frequency defines how fast the device can actuate at close to its maximum strain with unform curvature. If the frequency of the applied voltage is smaller than the cut-off frequency of the tri-layer, the CP layer is fully charged at peak voltage and the beam demonstrates uniform curvature at maximum displacement. Actuation speed is a function of device dimensions and material properties.

1.5.2 External and Free Strain

Peak-to-peak displacement (2D) represents the full range of motion of the actuator during a single voltage cycle. Below f_c, the device achieves close to maximum displacement amplitude (D). We calculate external strain ($2\epsilon_{ex}$) using Equation (1-5):

$$2\epsilon_{ex} = \frac{2Dh}{D^2+L'^2}, \tag{1-5}$$

where h is the thickness of the tri-layer swollen in electrolyte and L' is the distance from the fixed end to the point along the beam at which we measure displacement. However, external strain only accounts for the displacement and dimensions of the beam. Differential free strain (2ϵ), calculated using Equation (1-6), further accounts for the thicknesses and Young's moduli of individual layers.

Therefore, it is a more representative measure of the electrochemically induced strain in the active CP layers of the actuators. Here,

$$2\epsilon = 2\epsilon_{ex}\frac{h_p}{h}\left[\frac{nm^3+6m^2+12m+8}{6(m+1)}\right] = \frac{2Dh_p}{D^2+L'^2}\left[\frac{nm^3+6m^2+12m+8}{6(m+1)}\right], \quad (1\text{-}6)$$

where h_p is the thickness of the conducting polymer layer swollen in electrolyte, $m = h_g/h_p$ is the ratio of swelled thickness of the separator and conducting polymer layers, and $n = E_g/E_p$ is the ratio of swelled Young's moduli of the separator and conducting polymer layers, respectively.

1.5.3 Blocking Force

Blocking force (F_B) is the maximum force generated by the actuator, which we define as the minimum force required to keep the tip of the beam in its neutral position. The work in this thesis does not specifically focus on improving F_B; however, it is an important parameter for applications such as tactile displays. Equation (1-7) approximates the relationship between ϵ and F_B for $f < f_c$:

$$F_B \approx \epsilon\left[\frac{3W}{2L}E_p h_p\left(h_p + h_g\right)\right]. \quad (1\text{-}7)$$

The actuator achieves maximum possible F_B at $f < f_c$. Similar to the displacement-frequency response, F_B decreases as f increases above f_c. When we operate the devices faster than f_c, the electrodes only partially charge, and this reduces the overall force the system generates.

1.6 Literature Review on CP Tri-layer Actuators

In this section, we summarize and compare previous developments in the CP tri-layer actuator space. The most common CP's used for tri-layer actuators include PEDOT [38], PEDOT:SS [15, 39, 40], PPy [38, 41-45], and PEDOT:PPy composite [38]. Effective separator

materials include PEO:NBR [40] and PVDF [15, 38, 41, 44, 45]. Table 1-1 summarizes the typical Young's moduli reported for these materials. The tri-layer actuators characterized in this work were fabricated from PEDOT:PSS and PVDF.

Table 1-1 Young's Moduli of conducting polymers and separators commonly used to fabricate tri-layer actuators (Adapted from © 2019 Ebrahimi T. UBC [3]).

Material	Young's Modulus (MPa)	Reference
PPy	90	[26]
PEDOT	180	[23, 46]
PEDOT:PSS	2000	[47]
PEO:NBR, PEO:PTHF, PEO:PB copolymers	1	[23, 46]
PVDF	70	[26]

Figure 1-4 compares the relationships between f_c, maximum ϵ, and maximum F_B of different actuators described in the literature, for specified dimensions (Appendix A). This summary demonstrates the benefits and trade-offs between the different material selections. PEDOT has higher electrical and ionic conductivities than PPy. Fabrication methods for PEDOT achieve higher porosity, which facilitates better ion movement [38]. Therefore, PEDOT- and PEDOT:PSS-based actuators exhibit higher cut-off frequencies than PPy-based actuators [3, 23, 48]. This may make them more suited to high-speed applications that do not necessarily require high strain, such as vibrotactile displays [8, 18].

Maziz *et al.* reported the highest f_c; they showed that actuator deflection remained within 90% of its maximum amplitude up to 20 Hz for ultra-thin PEDOT/PEO:NBR/PEDOT micro-actuators with dimensions of 900 µm x 300 µm x 6 µm [23]. This ultra-thin structure facilitated shorter diffusion times than typical tri-layer actuator designs with thicknesses in the range of 50-150 µm. This study also demonstrated a fundamental resonant frequency (f_r) of 930 Hz, which is the highest reported value for CP tri-layer actuators. At f_r, the beam displaced 190 µm, 690 µm

from the fixed end. However, this thin design has a trade-off of lower F_B; the structure described by Maziz *et al.* only achieved 1.5 μN at low frequencies [23].

PPy-based actuators universally exhibit larger maximum free strain but with the trade-off of lower speeds [10, 33, 38, 45]. This is likely due to a more compact structure impeding ion movement through the electrodes [38]. Gaihre *et al.* reported the largest free strains up to 10.2% (at low f_c < 0.1 Hz) in a micro-actuator with dimensions of 850 × 250 × 126 μm, fabricated by electrodeposition of an 8 μm thick PPy layer on both sides of a 110 μm-thick commercial PVDF membrane [33].

PEDOT-PPy composite actuators achieved the highest F_B [38]. Temmer *et al.* demonstrated that the PEDOT layer allowed for higher actuation speeds and the PPy layer contributed to the higher strain and blocking force. The PEDOT/PPy/PVDF/PPy/PEDOT actuators achieved a blocking force of 4 mN/V at 0.2-1 V, which is the highest force reported in the literature. However f_c was only ~0.5 Hz, which is one to three orders of magnitude lower than values reported for PEDOT:PSS and PEDOT actuators.

In this thesis, we further developed and characterized tri-layer actuators fabricated from PEDOT:PSS/PVDF/PEDOT:PSS. Previous work by Ebrahimi T. *et al.* achieved an f_c, ϵ, and F_B values of of 2.2 Hz, 0.63 %, and 0.6 mN, respectively [3]. We used the fabrication technique spray coating to deposit controlled, quantifiable sub-millimeter thick PEDOT:PSS layers on a 100-125 μm PVDF membrane. An advantage to these actuators is that they were fabricated from commercially available materials through a reproducible and scalable fabrication method.

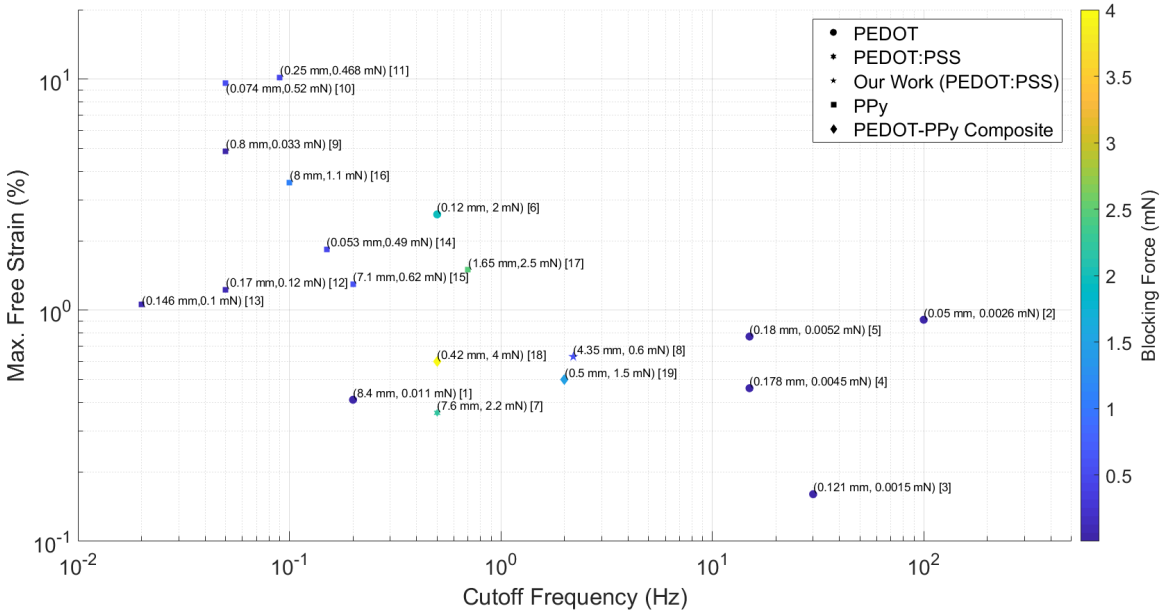

[1] PEDOT/PEO:NBR/PEDOT in EMITFSI N. T. Nguyen *et al.*, *Electrochim. Acta* 265, 670–680 (2018)

[2] PEDOT/PEO:NBR/PEDOT in EMITFSI A. Maziz *et al.*, *Electroact. Polym. Actuators Devices 2015*, 9430, 94300O (2015)

[3] PEDOT/PEO:NBR/PEDOT in EMITFSI (6 µm thick) A. Maziz *et al.*, *Adv. Func. Mater.*, 24, 4851–4859 (2014)

[4] PEDOT/PEO:NBR/PEDOT in EMITFSI (12 µm thick) A. Maziz *et al.*, *Adv. Func. Mater.*, 24, 4851–4859 (2014)

[5] PEDOT/PEO:NBR/PEDOT in EMITFSI (19 µm thick) A. Maziz *et al.*, *Adv. Func. Mater.*, 24, 4851–4859 (2014)

[6] (PEDOT/PEDOT)/PVDF/(PEDOT/PEDOT) in 1 M LiTFSI in PC R. Temmer *et al.*, *Smart Mater. Struct.*, 22, 104006 (2013)

[7] PEDOT:PSS/(IL/PU)/PEDOT:PSS in EMITFSI H. Okuzaki *et al.*, *Sensors Actuators, B Chem.*, 194, 59–63 (2014)

[8] PEDOT:PSS/PVDF/PEDOT:PSS in EMITFSI S. E. Takalloo, The University of British Columbia, 2019.

[9] PPy/PVDF/PPy in 0.1 M LiTFSI in PC (porous, 1% salicylic acid) B. Gaihre *et al.*, *J. Microelectromechanical Syst.*, 21, 574–585 (2012)

[10] PPy/PVDF/PPy in 0.1 M LiTFSI in PC (0.025 M LiTFSI-incorporated) B. Gaihre *et al.*, *J. Microelectromechanical Syst.*, 21, 574–585 (2012)

[11] PPy/PVDF/PPy in 0.1 M LiTFSI in PC (commercial membrane) B. Gaihre *et al.*, *J. Microelectromechanical Syst.*, 21, 574–585 (2012)

[12] PPy/PVDF/PPy in 0.1 M LiTFSI in PC (porous, 1% salicylic acid) B. Gaihre *et al.*, *J. Microelectromechanical Syst.*, 21, 574–585 (2012)

[13] PPy/PVDF/PPy in 0.1 M LiTFSI in PC (0.0125 M LiTFSI-incorporated) B. Gaihre *et al.*, *Sensors Actuators, B Chem.*, 155, 810–816 (2011)

[14] PPy/PVDF/PPy in 0.1 M LiTFSI in PC (commercial membrane) B. Gaihre *et al.*, *Sensors Actuators, B Chem.*, 155, 810–816 (2011)

[15] PPy/PVDF/PPy in 0.1 M LiTFSI in PC S. W. John, G. Alici, and C. D. Cook, *Electroact. Polym. Actuators Devices 2008*, 6927, 69271T (2008)

[16] PPy/PVDF/PPy in 0.05 M TBA PF6 in PC G. Alici and N. N. Huynh, *IEEE/ASME Trans. Mechatronics*, 12, 73–84 (2007)

[17] (PPy/PPy)/PVDF/(PPy/PPy) in 1 M LiTFSI in PC R. Temmer *et al.*, *Smart Mater. Struct.*, 22, 104006 (2013)

[18] (PEDOT/PPy)/PVDF/(PPy/PEDOT) in 1 M LiTFSI in PC R. Temmer *et al.*, *Smart Mater. Struct.*, 22, 104006 (2013)

[19] (PPy/PEDOT)/PVDF/(PEDOT/PPy) in 1 M LiTFSI in PC R. Temmer *et al.*, *Smart Mater. Struct.*, 22, 104006 (2013)

Figure 1-4 Plot of maximum free strain versus cut-off frequency of tri-layer CP actuators. Each data point corresponds to a single device and is labelled with its maximum peak-to-peak displacement and blocking force for the specified dimensions reported in the study.

1.7 The Development of Conducting Polymers

Conducting polymers show promise in flexible, inexpensive, large-area applications, such as flexible displays, radio frequency identification devices (RFIDs), photovoltaic arrays; sensors and actuators [49]. In 1977, Alan J. Heeger, Alan G. MacDiarmid, and Hideki Shirakawa discovered doped the polymer polyacetylene exhibited high conductivity up to 28, 500 S/cm; for this work they won the Nobel Prize in Chemistry in 2000 [50, 51]. While polyacetylene failed to achieve commercialization due to its poor stability in air, the discovery of its conductive properties launched subsequent research into conducting polymers as a new generation of materials that exhibit the intrinsic electrical and optical properties of metals and semiconductors, but maintain the mechanical and processing advantages of polymers [52].

Strategies to solve the lack of stability of polyacetylene involved the addition of electron donating heteroatoms, such as N and S, either in the main polymer chain or as carbon substituents in the heterocycles [53, 54]. In 1988, the German Bayer Company used this concept to synthesize poly(3,4-ethylenedioxythiophene) polystyrene sulfonate (PEDOT:PSS), which has become one of the most successful conducting polymers in both fundamental research and commercial applications [54-56]. PEDOT:PSS has good film-forming properties, high transparency in the visible range, thermal stability, tunable conductivity through secondary doping or solvent treatment, environmental stability, and flexibility [53, 56-59].

PEDOT is prepared through the oxidation polymerization process of EDOT [60]. To synthesize PEDOT, the monomer EDOT is immersed in a polyelectrolyte solution in the presence of an oxidizing agent. PSS is the most common anionic polymer used in this process, which results in aqueously dispersed PEDOT:PSS [56]. In this system, PSS functions as both the dopant and charge stabilizer for PEDOT [55]. PEDOT alone is hydrophobic and insoluble in water, which

restricts deposition methods. PSS is an anionic surfactant whose hydrophilicity enables aqueous dispersion [55, 61].

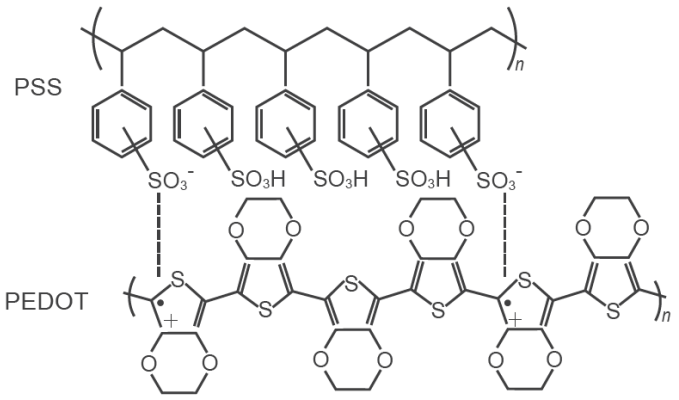

Figure 1-5 Chemical structure of PSS (top and PEDOT (bottom). A chemical shift in S 2p peak occurs as a result of the different oxidation states of S in PSS and PEDOT.

PEDOT:PSS consists of nuclear crystalline PEDOT domains surrounded by amorphous PSS matrices. Figure 1-5 shows the chemical structure of PEDOT:PSS. PEDOT has a conjugated backbone that allows delocalized bipolarons to easily transfer via π-orbitals [57]. Polymer chains stack due to π-π interactions, which give rise to weak Van der Waals forces. Unfortunately, PSS is not electronically active and therefore hinders the electronic performance of PEDOT. Charge transfer is fast along PEDOT chains, moderate between PEDOT chains, and slow between lamellar planes that are separated by insulating PSS [55]. Therefore, charge transport mechanisms depend on the structure and doping of the CPs [49, 53].

1.8 Literature Review on PEDOT:PSS Electrical Conductivity

In this section, we explore previous work to improve the electrical conductivity of PEDOT:PSS films. Table 1-2 summarizes the changes to electrical conductivity following post-treatment with acid, polar solvents, or ionic liquids reported in the literature. As we discussed in Section 1.5.1, the electrical resistance of the CP material contributes to the impedance of the tri-layer system. This results in a lower mechanical response as frequency increases, due to

insufficient time for the electrodes to become fully charged. We investigated techniques to post-treat PEDOT:PSS films to increase the speed of the devices.

Pristine PEDOT:PSS films tend to exhibit low chain alignment with the presence of excess PSS. This alignment is an important characteristic for CP's because it determines the energy required for charge to transfer between polymer chains, which contributes to the overall conductivity of the material. Th morphology of pristine films results in low electrical conductivity in the range of 1-10 S/cm [59, 62]. Secondary doping is the most common approach to effectively enhance PEDOT:PSS conductivity by optimizing the morphology and crystal structure of PEDOT, which increases carrier mobility and density. This involves either adding dopants to the aqueous solution or post-treatment of PEDOT:PSS films with a dopant solution. Secondary doping differs from primary doping (doping that takes place during polymerization) in that the property changes the polymer experiences may persist even after the secondary dopant is completely removed [63].

Addition of certain additives causes a screening effect, which weakens coulombic interactions between positively charged PEDOT and negatively charged PSS and promotes rearrangement of the PEDOT chains [55]. However, this method often also promotes gelling, which limits the deposition methods possible for fabrication. Kim *et al.* (2002) showed that dimethyl sulfoxide (DMSO) increases PEDOT:PSS electrical conductivity from 0.8 S/cm to 80 S/cm but does not cause the aqueous solution to gel [64]. Additionally, Jonsson *et al.* observed an increased ratio of PEDOT:PSS after mixing the solution with solvents, which they attributed to some segregation of PSS from the surface of the grains and removal from the surface of the film. This induced better connection between PEDOT:PSS grains, creating a more efficient pathway for charge transport [53, 56]. Now, commercial manufacturers of PEDOT:PSS recommend adding

DMSO to their products prior to deposition; the recipe we followed in this work uses a 5% (v/v) DMSO in PEDOT:PSS solution.

Post-treatments effectively remove excess insulating phase to enhance conductivity of CP films. Commonly used post-treatment solutions include: organic solvents, acids, alkali, ionic liquids (ILs), and reducing agents [55, 57, 58, 60]. Physical treatments such as annealing and UV radiation also alter PEDOT:PSS film morphology and improve the conductivity of the material [65-68]. In this work, we explore several chemical post-treatments and their influence of conductivity and actuation.

1.8.1 Acid Post-Treatment

Concentrated sulfuric acid (H_2SO_4) is the most successful reported secondary dopant post-treatment for increasing PEDOT:PSS conductivity. Kim *et al.* found significant electrical conductivity enhancement when directly dipping or immersing PEDOT:PSS films into H_2SO_4, which resulted in a maximum conductivity value of 4380 S/cm (the highest recorded at the time of the study in 2014 and nearly comparable to ITO – a material commonly used as the charge transport layer or electrical interconnect in organic electronic devices). X-ray diffraction (XRD) absorption peaks in the UV range correlated with PSS reduced with increasing acid concentration, demonstrating that H_2SO_4 selectively removed PSS from the polymer matrix. This treatment also induced structural rearrangement of PEDOT:PSS and the formation of crystallized nanofibrils via a charge-separated transition mechanism. The extent of morphological changes also increased with increasing acid concentration [62]. Recently, Shi *et al.* demonstrated a further increase the maximum recorded electrical conductivity of 6324 S/cm following concentrated H_2SO_4 post-treatment. To achieve this, films were treated with H_2SO_4 twice: once at 9.2mol/L and second at 18.4mol/L [69].

1.8.2 Polar Solvent Post-Treatment

A plethora of studies investigate the effects of polar solvent post-treatment methods on the electrical conductivity properties of PEDOT:PSS. Post-treatments that have shown to significantly increase the conductivity of PEDOT:PSS include immersing the films in: (1) DMSO [70, 71], (2) methanol (MeOH) [72], (3) ethylene glycol (EG) [73-75]. The hydrophilic nature of PSS and the hydrophobic nature of PEDOT offers a means for selectively de-doping PSS from PEDOT using these polar solvents.

DMSO dissolves the PSS shell so that PEDOT in the core releases and self-aggregates, which leads to phase separation of the PEDOT and PSS [53]. Luo *et al.* showed that DMSO post-treatment of PEDOT:PSS is much more efficient than DMSO aqueous addition for the improvement of conductivity. However, Unsworth *et al.* showed that both methods (immersion or addition) improve conductivity by a similar magnitude [76].

Alemu *et al.* post-treated PEDOT:PSS films with methanol and the conductivity increased from 0.3 to 1362 S/cm. Other alcohols like ethanol and propanol showed inferior conductivity enhancements. The conductivity enhancement was greatly affected by the hydrophilicity and dielectric constant of the alcohols used [77].

Multiple studies successfully demonstrated that EG post-treatment improves the electrical conductivity of PEDOT:PSS. Ouyang *et al.* enhanced the conductivity of PEDOT:PSS by more than two orders of magnitude with EG [75]. Ely *et al.* further enhanced the conductivity by chemically modifying PEDOT:PSS films with EG. The peak conductivity through this method was 610 S/cm [73]. Sankir *et al.* showed that EG post-treated films experienced a 250-900x increase in conductivity [74].

1.8.3 Mechanisms

Despite the substantial amount of literature showing the improvement in conductivity with chemical post-treatments, the mechanisms are still widely debated. Some suggested mechanisms include [76, 78]:

(1) A screening effect between PEDOT and PSS chains due to polar solvents that induce a phase separation between the polymers.
(2) PSS precipitation and removal.
(3) Enhanced charge mobility, due to improved interchain packing and thinner PSS barriers.
(4) More uniform distribution of PEDOT-rich regions.

The most commonly proposed mechanism in literature is that the increased conductivity is associated with phase separation between the insulating PSS and the conducting PEDOT. Polar additives weaken the electrostatic interactions between PEDOT and PSS, thus promoting separation of the two polymers. This screening also causes the redistribution of PEDOT on PSS chains, facilitating the release of free PSS [61]. A major piece of evidence that supports this hypothesis is the decrease of the PSS content, as measured using S 2p signal intensity on the film surface from X-ray photoelectron spectroscopy (XPS) [61, 76, 79]. Polymer interactions with these solvents provide free energy that favors dissolving PSS, which washes away excess PSS and improves interconnectivity of the PEDOT-rich domains [53, 61, 80].

A study by Palumbiny *et al.* used Grazing-Incidence Wide-Angle X-ray Scattering (GIWAXS) to observe the structural evolution of PEDOT:PSS in EG treated films during drying. Their results showed a decrease in the π-π stacking distance from 3.63 to 3.45 Å. The authors proposed a model in which EG promoted the interchain coupling of PEDOT segments, which enhanced conductivity [81]. Additionally, hydrogen bonding between the EG and PSS components caused a phase separation, which lead to a linear reorientation of PEDOT chains and larger PEDOT

domains in the bulk film. Collectively, these factors resulted in higher electrical conductivity compared to pristine PEDOT:PSS [82].

Ouyang *et al.* suggested that the number of polar groups in organic solvents affects the conductivity of PEDOT:PSS [75]. The interactions between the dipoles drives the conformation of PEDOT in solid film from coiled type (dominated by benzene chain structure to a linear type (dominated by quinone chain structure) resulting in delocalization of the carriers on the PEDOT chain, which improves electronic transmission [55]. As a result of this linear realignment, Shi *et al.* showed through 4-point probe measurements that out-of-plane conductivity can be up to five orders of magnitude lower than in-plane conductivity, which indicates electron transport properties of PEDOT:PSS are anisotropic [69]. We did not observe this significant of a difference between planes in our results, discussed in Section 2.5.2.

1.8.4 Ionic Liquid Post-Treatment

Ionic liquids (IL) are organic/inorganic salts with properties such as good chemical stability, low flammability, negligible vapor pressure, and a large electrochemical window ($3.5<EW<6$). The majority of investigations to improve electrical conductivity with ILs focus on ethyl-3-methylimidazolium (EMIM) ILs [83], such as ethyl-3-methylimidazolium bis(trifluoromethylsulfonyl)imide (EMIM TFSI) – the IL we use as the electrolyte in this work [84]. A study by Atoyo *et al.*, looking at improving electrical conductivity and the Seebeck coefficient in PEDOT:PSS using EMITFSI, showed a maximum conductivity of 1439 S/cm. This is highly conductive compared to solvent treatments such as DMSO (100-600 S/cm) and EG (400-1000S/cm). The proposed mechanisms for improving conductivity are similar to those discussed for polar solvents [84, 85].

In another example with different ILs, Oechsle *et al.* showed that post-treatment with 1-ethyl-3-methylimidazolium dicyanamide (EMIM DCA), 1-allyl-3-methylimidazolium dicyanamide (AMIM DCA) and 1-Ethyl-3-methylimidazolium tetracyanoborate (EMIM TCB) increase the electrical conductivity of PEDOT:PSS by 2-3 orders of magnitude. EMIM DCA and AMIM DCA both decrease the film thickness by ~150 nm, however EMIM TCB increased film thickness by about 75 nm. The most pronounced improvement occurred with EMIM DCA treatment, with a maximum conductivity of 1126 S/cm [83]. This study proposed the increased conductivity was due to the removal of non-conductive PSS polymer and conductivity enhancing morphology changes to the PEDOT:PSS films. This was supported by the measured decrease in film thickness with the post-treatment of EMIM DCA and EMIM DCA. For the case of EMIM TCB, the film thickness increased, which is likely due to the interaction between IL anions and the charged polymer backbone, $PEDOT^+$; The anions replace PSS^- and accumulate in the polymer matrix, causing swelling [83]. This ion exchange between the PSS and IL components helps PEDOT decouple from PSS and grow into large-scale conducting domains [86].

Teo *et al.* used EMIM TCA to improve the electrical properties of PEDOT:PSS for stretchable electronic applications. They added increasing concentrations of the IL to aqueous PEDOT:PSS and observed that this resulted in an increase of electrical conductivity from 1 S/cm to 1280 S/cm. However, they also observed that adding high concentrations of EMIM TCA caused PEDOT:PSS to precipitate out of solution and made the material too viscous for fabrication techniques requiring a liquid starting material [87].

Finally, Luo *et al.* came up with a method to treat PEDOT:PSS films with a mixture of organic solvent and IL. All films post-treated demonstrated much higher conductivity compared to untreated films. They showed that DMSO alone increased electrical conductivity more than the

mixed DMSO+IL [88]. In our work, we soak all our CP tri-layer actuators in the IL electrolyte EMITFSI, which provided the ions that migrate and facilitate actuation. Therefore, we further explored how the combination of ILs and polar solvents affect the material and electrical properties of PEDOT:PSS.

Table 1-2 Summary of electrical conductivity following chemical post-treatments.

Additive	Additive type	Pristine Conductivity (S/cm)	Treated Conductivity (S/cm)	Supplier	Substrate	Film Fabrication Method	Reference
oxalic acid	Acid	0.2	182	Clevios PH1000	Glass	Spin coating	[89]
sulfuric acid	Acid	1	4380	Clevios PH1000	Glass	Spin coating	[62]
sulfuric acid	Acid	4.2	6323.9	Clevios PH 1000	Glass	Spin coating	[69]
AMIM DCA	Ionic liquid	1	881	Ossila PH1000	Glass	Spin coating	[83]
EMIM DCA	Ionic liquid	1	1126	Ossila PH1000	Glass	Spin coating	[83]
EMIM TCB	Ionic liquid	1	440	Ossila PH1000	Glass	Spin coating	[83]
EMIM BF_4	Ionic liquid	1	125	Clevios PH1000	Glass	Spin coating	[88]
DMSO	Polar solvent	1	930.21	Clevios PH1000	Glass	Spin coating	[88]
EG	Polar solvent	0.4	200	Baytron P V4071	Glass	Spin coating	[75]
EG	Polar solvent	0.2	1200	Ossila PH1000	Silicon	slot-die coated	[81]
MeOH	Polar solvent	0.3	1362	Clevios PH1000	Glass	Spin coating	[77]
DMSO +EMIM BF_4	Polar solvent + ionic liquid	1	700	Clevios PH1000	Glass	Spin coating	[88]

1.9 Conclusion

In this thesis, we explore the effect of the post-treatments on electrochemical and actuation properties of PEDOT:PSS/PVDF/PEDOT:PSS tri-layer actuators. Most studies looking to improve electrical conductivity of PEDOT:PSS focus purely on improving the electrical properties of the material for applications such as flexible organic electronic devices. However, these studies do not consider the electrochemical properties of the material [90]. They do not consider the effects to ionic conductivity of the material, and, in most cases, porosity is not desired in the polymer structure. For CP tri-layer actuators, we also needed to investigate how these post-treatments affected ionic conductivity because ionic resistance is a large source of impedance that increases the time constant in our actuators.

In the following Chapters we investigate how MeOH, EG, DMSO, and EMITFSI alter the charge storage and charge transfer mechanics of our CP tri-layer actuators. The goal of this work was to increase actuation speed, such that our devices achieve high displacements and blocking forces at high frequencies. We hypothesized that we could achieve this by improving electrical conductivity of PEDOT:PSS.

Chapter 2: Electrochemical Characterization

In this chapter, we discuss the materials selection, fabrication, and electrochemical characterization of PEDOT:PSS/PVDF/PEDOT:PSS tri-layer actuators. We first describe the spray coating method we used to deposit the commercially available conducting polymer poly(3,4-ethylenedioxythiophene) polystyrene sulfonate (PEDOT:PSS) on the separator membrane polyvinylidene fluoride (PVDF). Based on the literature review discussed in Chapter 1, we selected the polar solvents methanol (MeOH), ethylene glycol (EG) and dimethyl sulfoxide (DMSO) to treat the PEDOT:PSS films.

Initial characterization included optical profilometry to measure the thicknesses of the deposited PEDOT:PSS films, analysis of PEDOT:PSS water solubility pre- and post-treatment, and measurements of mass change at each stage of the tri-layer fabrication process. Next, we present electrical and ionic conductivity results of the untreated and treated devices. We then further characterized the electrochemical behavior of the CP tri-layer actuators through cyclic voltammetry. This allowed us to determine the volumetric capacitance and time constants for each treatment. Finally, we presented results from X-ray photoelectron spectroscopy (XPS), which we used to analyze the near surface chemistry of our tri-layer actuator samples pre- and post-treatment. XPS analysis showed that PSS was removed from the surface of the sample following chemical treatments, which helped us explain the increases to electrical conductivity we observed.

2.1 Materials Selection and Tri-layer Fabrication

2.1.1 Materials

This section summarizes the key materials we used to fabricate and characterize the CP tri-layer actuators.

2.1.1.1 Conducting Polymer

We used the conducting polymer poly(3,4-ethylenedioxythiophene) polystyrene sulfonate (PEDOT:PSS, Heraeus Clevios™ PH 1000, Ossila) as the electrically active material in our tri-layer actuators. This material is designed for high conductivity and optical transparency applications. As discussed in Section 1.7, PEDOT:PSS is a commercially available, which removes the need for complex synthesis processes. In addition, its stability in air and water solubility allows for simple fabrication techniques (such as spray coating, molding or printing) and storage. We chose PEDOT:PSS over other conducting polymers due to these advantageous properties. Table 2-1 summarizes relevant technical specifications provided by the company.

Table 2-1 Summary of technical specifications for PEDOT:PSS (Heraeus Clevios™ PH 1000, Ossila) provided by the company.

Specification	Value
Resistivity	< 0.0012 Ω.cm (with use of 5% (v/v) as morphology enhancer
Solid content	1.0 – 3.0 wt% dispersed in water
PEDOT:PSS ratio	1:2.5
Particle size distribution	D_{50} = 30 nm
Work Function	4.8 – 5.0 eV

2.1.1.2 Separator

We used commercially available polyvinylidene fluoride (PVDF, Durapore®, MilliporeSigma) as the ionically conductive porous separator layer. This material is commercially available, highly porous and ionically conductive. Previous work, discusses in Section 1.6, has successfully described PVDF as the separating membrane in tri-layer actuators [3, 10]. This

separator layer serves as an ion reservoir through which ions migrate under an applied potential between CP layers [45]. According to the company specifications, these hydrophilic membranes have a thickness of 125 μm and pore size of 0.45 μm. One disadvantage of commercial PVDF is that we cannot control th thickness of the membrane.

2.1.1.3 Electrolytes and Solvents

EMITFSI

We used the ionic liquid (IL) 1-Ethyl-3-methylimidazolium Bis(trifluoromethanesulfonyl) imide (EMITFSI, ≥ 99%, Solvionic). EMITFSI is a non-aqueous solvent/electrolyte that has advantages over its traditional water-based counterparts due to its low vapor pressure, high thermal stability, good conductivity, and wide electrochemical window. Its non-volatile and stable properties eliminate the need for encapsulation of the tri-layer actuators. This allows the devices to have a long shelf-life, such that mechanical performance does not decrease overtime due to evaporation or degradation of the electrolyte [39].

Polar Solvents

Base on our analysis of previous work describe in Section 1.8, we used the following solvents to post-treat the PEDOT:PSS films in our tri-layer actuators:

- Methanol, MeOH (CH_3OH, ≥ 99.8%, Sigma-Aldrich)
- Ethylene glycol, EG ($HOCH_2CH_2OH$, 99.8%, Sigma-Aldrich)
- Dimethyl sulfoxide, DMSO ($(CH_3)_2SO$, ≥ 99.7%, Sigma-Aldrich)

2.1.1.4 Contact Electrodes

Contact resistance between metal electrodes and the CP material contributes to limiting the speed of the device. Additionally, certain metals react with the electrolyte stored in the device, which further increases contact resistance and can damage the sample. We selected gold ((99.99%, 0.127-mm thick, Sigma Aldrich) as the electrode material because it is inherently inert and is the best choice to achieve an ohmic contact with PEDOT:PSS. Gold has a work function of 5.1-eV [91], which nearly matches the HOMO level of PEDOT:PSS of 4.8 – 5.0 eV.

2.1.2 Fabrication

This section describes the spray coating fabrication process we used to deposit PEDOT:PSS on both sides of PVDF membranes. It also discusses the chemical post-treatments we used to enhance the electrical properties of the CP electrodes.

2.1.2.1 Spray Coating

This tri-layer fabrication method was developed and refined by Ebrahimi T. *et al.* over the course of her PhD at the University of British Columbia [3]. Spray coating is a well-characterized film deposition technique that allows for tuning the thickness of each coat down to 200 nm. This process is also scalable, low cost, reliable, and reproducible. We prepared a solution of aqueously dispersed PEDOT:PSS (Heraeus Clevios^{TM} PH 1000, Ossila) with 5% (v/v) DMSO (as recommended by the manufacturer) and stirred vigorously for at least 15 minutes. The solution was then loaded into a 25 mL spray-coating syringe (Hamilton 1025 TLL). We used a Sono-Tek ExactaCoat robotic spray coater equipped with a 120 kHz ultrasonic atomizing nozzle to deposit PEDOT:PSS on the PVDF membranes. This deposition technique converts high frequency sound waves into mechanical energy, which is then transferred into the liquid deposition material creating

a standing wave. A fine mist of uniform droplets form (mean diameter = 18 μm) that break away from the atomizing surface of the nozzle and are directed towards the substrate via the shaping air. We used Vortex ultrasonic spray shaping to produce a conical spray pattern, which followed a raster path with a spacing of d = 2-mm.

We fixed 6.7-cm x 6.7-cm sheets of PVDF on the spray-coating substrate using a machined Al frame with a mask dimension of 5-cm x 5-cm. We also heated the substrate temperature to 130°C to facilitate rapid water evaporation and prevent diffusion of the deposited material into the bulk PVDF and short circuiting between the two CP layers. Ebrahimi T. *et al.* demonstrated that this fabrication procedure reliably produced functional tri-layer actuators [3]. We did not explore how adjusting these parameters affected material properties or performance in this work. Table 2-2 lists the fixed parameters of this deposition procedure, which we controlled using the software, ExactaCoat, provided by the manufacturer. Each sample was allowed to heat up to the temperature of the substrate and coated with 20 layers of PEDOT:PSS per side. We weighed the PVDF membranes, using an analytical balance (Mettler Toledo, accuracy of 0.1 mg), before and after deposition to determine the mass of PEDOT:PSS (detailed SOP available in Appendix B.1).

Table 2-2 list of parameters used for spray coating.

Parameter	Value
Substrate Temperature (T)	130°C
Nozzle Height (H)	9 cm
Path Spacing (d)	2 mm
Nozzle Speed (V_n)	20 mm/s
Shaping Air Pressure (P_{air})	4 PSIG
Sample Flow Rate (Q)	0.13 mL/min

2.1.2.2 Solvent Treatment

Following deposition, we used a fresh razor blade to cut tri-layer samples into either 1.5-cm x 1.5-cm samples, 1-cm x 3-cm samples, or T-shaped samples with a beam dimension of 1.2-cm x 2-mm and a contact area of 4-mm x 3-mm. These shapes are shown in Figure 2-1.

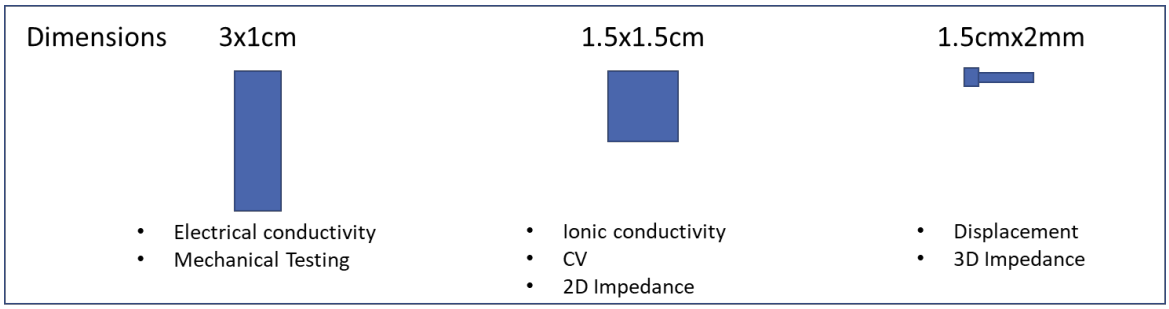

Figure 2-1 dimensions of cut samples and experiment for which each sample type was used for.

We post-treated the PEDOT:PSS films with DMSO, EG, MeOH, DMSO+EMITFSI, EG+EMITFSI (50%v/v) or MeOH+EMITFSI (50%v/v). Table 2-3 summarizes these treatment methods.

Table 2-3 Summary of post-treatment methods.

Treatment	Time for Solvent Immersion (min)	Time for post-treatment MeOH Solvent Immersion (min)
Pristine	-	-
MeOH	45	-
MeOH+EMITFSI	45	-
DMSO	10	15
DMSO+EMITFSI	10	-
EG	10	15
EG+EMITFSI	10	-

DMSO and EG Treatments

We soaked 3 of each sample dimensions type in the organic solvent for 10 minutes, while gently stirring. Oversoaking the samples resulted in damage to the PEDOT:PSS films (Appendix C.1). We then soaked these samples in MeOH for 15 minutes to remove the solvent from the

sample. MeOH was chosen because it is highly volatile (~12kPa at room temperature) and therefore evaporated quickly during the drying process. The samples were then dried on a hot plate at 50°C until all solvent was completely evaporated.

DMSO+EMITFSI and EG+EMITFSI Treatment

We prepared the solvent solution by mixing an equal volume of DMSO or EG and EMITFSI and stirring vigorously for 15 minutes. Three of each sample dimension type was soaked in these prepared solvents for 10 minutes, while gently stirring. Following immersion, samples were dried on a hot plate at 50°C, until they appeared dry. However, since EMITFSI is non-volatile, we could not remove all the solvent from the films.

MeOH and MeOH+EMITFSI Treatment

We soaked 3 of each sample dimension type in the organic solvent for 45 minutes, while gently stirring, until the samples were completely saturated. MeOH is a much gentler solvent than EG or DMSO, and oversoaking did not damage the PEDOT:PSS films. The samples were then dried on a hot plate at 50°C until all solvent was completely evaporated. A similar treatment procedure was also followed for samples soaked in a MeOH+EMITFSI (50%v/v) solution, which was prepared by mixing equal volume MeOH and EMITFSI and stirring vigorously for 15 minutes.

Ionic Liquid Electrolyte Saturation

We soaked all samples (including untreated samples) in EMITFSI electrolyte for at least three hours, which was the amount of time needed for complete saturation of this thicknesses of our samples described by Ebrahimi T. *et al.* [3].

2.2 Profilometry

Optical profilometry is a non-destructive, non-contact surface analysis technique we used to measure the thickness of the PEDOT:PSS layers following spray coating fabrication. The instrument splits a light beam into two paths; one path reflects off the surface of the sample of interest and the other reflects off a reference mirror. When the reflected light from these two surfaces recombines, the interference patterns provide information about the surface topography of the sample. In the following section, we discuss the application of this technique to characterize the dimensions of our samples.

2.2.1 Methods

In Previous work, Ebrahimi T, *et al.* measured the equivalent thickness of the spray coated PEDOT:PSS layers using a Bruker Dektak XT profilometer (stylus diameter: 2 μm, force: 0.1 mN) [3]. The results demonstrated a linear relationship between PEDOT:PSS film thickness and the number of spray coats. We reproduced these measurements using a 3D optical surface profilometer (Filmetrics Profilm3D). We determined step height for 6, 10, 12, 15, 21, and 30 coats of PEDOT:PSS deposited on a glass microscope slide.

We also performed optical profilometry measurements on PEDOT:PSS/glass samples following post-treatment with each of the methods outlined in Section 2.1.2.2. As discussed in Section 1.8.3 on mechanisms, polar solvents cause morphological changes and the removal of PSS in the PEDOT:PSS films. The goal of these measurements was to identify and quantify the change in thickness to the PEDOT:PSS films.

2.2.2 Results

Figure 2-2 shows the linear relationship between film thickness (h_p) and number of PEDOT:PSS coats (n). One coat deposited a film of PEDOT:PSS 230 nm thick. Previous work by Ebrahimi T, *et al.* reported a single coat thickness of ~400 nm, which they claimed to date was the minimum thickness reported for the CP layer of a tri-layer conducting polymer actuator [3]. We have achieved a layer thickness slightly more than half of their reported value.

Ebrahimi T, *et al.* also showed that sheet resistance of the PEDOT:PSS films decreased with increasing number of coats due to penetration of the CP into the porous structure of the PVDF membrane. Therefore, the initial coats of PEDOT:PSS have a higher actual surface area. As the number of coats increases and the pores fill in, the apparent and actual surface area values converge, and sheet resistance decreases. Additionally, as the pores are filled in, contact area increases, which reduces the contact resistance between the CP and gold electrodes [3]. Based on these findings, we chose to design tri-layer actuators spray coated with 20 layers of PEDOT:PSS. This corresponded to an equivalent glass slide thickness of 4.74-µm, which is sufficiently thick to reduce both sheet and contact resistance.

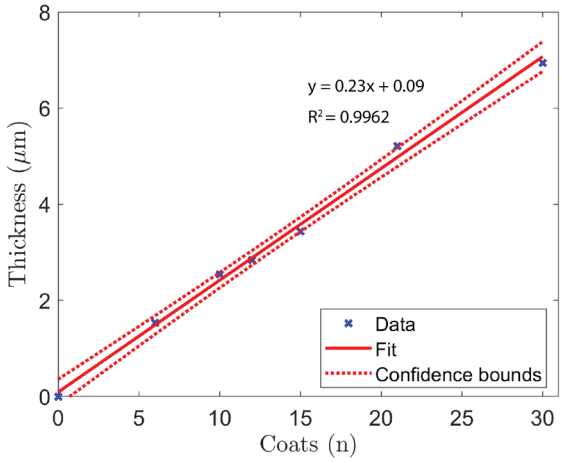

Figure 2-2 Thickness of PEDOT:PSS deposited on a glass slide versus the corresponding number of coats.

We did not observe changes in thickness between untreated and treated PEDOT:PSS/glass samples. These results contradict previous reports on organic solvent treatments – including MeOH, DMSO, and EG – reducing the total film thickness of deposited PEDOT:PSS [92]. The lack of changes to film thickness are likely due to immersion of all samples, including pristine, in the EMITFSI. Previous work showed that samples soaked in EMITFSI swelled proportionately to the IL uptake [93, 94]. Since all samples are treated with EMITFSI, this may explain why the film thickness does not change between samples.

Based on these results, we assumed that the film thickness of all 20-layer, treated or untreated, samples was (4.74 ± 0.1) μm. This assumption has several limitations, which Section 2.2.3 outlines.

2.2.3 Limitations

There are several limitations to this method of using profilometry to measure equivalent PEDOT:PSS film thickness on glass slides. However, the rough and opaque nature of PEDOT:PSS and PVDF make it impossible to use profilometry to directly measure CP film thickness deposited on the membrane. Additionally, the initial coats of PEDOT:PSS penetrate into the bulk of the PVDF membrane through the pores. In this analysis of the tri-layer actuators, we assumed there is a distinct junction between the two materials; in reality, a PEDOT:PSS gradient exists. Therefore, the actual thickness of the PEDOT:PSS electrodes is slightly larger than the film deposited on glass slides. Work by Ebrahimi T, *et al.* used scanning electron microscopy (SEM) in conjunction with Energy-dispersive X-ray (EDX) element analysis to image a cross section of a 10 layer PEDOT:PSS/PVDF/PEDOT:PSS tri-layer actuators. These results showed that some PEDOT:PSS can penetrate up to 15 μm into the PVDF membrane on each side, which leaves ~95 μm of PVDF with no PEDOT:PSS [3]. Simaite *et al.* showed that a certain depth of this entanglement between

the PEDOT:PSS polymer chains and PVDF membrane promotes better adhesion between the layers, which reduces the likelihood of delamination under mechanical stress [39].

Finally, we also assumed that deposition of PEDOT:PSS is symmetrical on either side of the PVDF membrane. However, due to manual processes involved in fabricating the tri-layers, such as flipping the PVDF membranes over to switch sides being spray coated, it is unlikely the devices are ideally symmetrical. Simaite *et al.* used AFM to show that commercial PVDF membranes have slightly asymmetric surface roughness's, which may also contribute to differences in how PEDOT:PSS wets and bonds to the each side of the membrane during spray coating [39]. Nguyen *et al.* also reported asymmetry in their PEDOT/PEO:NBR/PEDOT tri-layer actuators by measuring differences in electrical properties of the different electrodes [95].

2.3 PEDOT:PSS Water Solubility

PEDOT:PSS is water soluble due to the hydrophilicity PSS component. While this property is a valuable asset that allows for easy fabrication of thin films from commercially available PEDOT:PSS, it limits the selection of electrolyte materials to those that are non-aqueous, such as IL's. In this section we show how removing PSS via organic solvent treatment improves the stability of our tri-layer actuators in water.

2.3.1 Methods

We soaked 1cm x 1cm 20-layer PEDOT:PSS/PVDF samples in deionized (DI) water for 1 minute while stirring. We then rubbed the samples on a piece of white A4 paper until they were dry. We then used tweezers to scrape at the surface of the samples and observed if we could remove PEDOT:PSS. From this crude experiment we were able to draw conclusions on the stability of each sample following immersion in DI water. We performed this process with a pristine sample and samples treated with MeOH, MeOH+EMITFSI, EG, EG+EMITFSI, or DMSO.

2.3.2 Results

Figure 2-3 shows the images of each sample following immersion in DI water. The pristine sample (Figure 2-3a) was severely damaged; PEDOT:PSS rubbed off onto the A4 paper and we were easily able to scrape the CP off the membrane. This shows that untreated PEDOT:PSS samples are not stable in aqueous solution. Conversely, all treated samples (Figure 2-3b-e) exhibited high stability in water. We observed that very little PEDOT:PSS rubbed off in this process.

PSS both balances the charge of the polymer backbone and stabilizes aqueously dispersed PEDOT:PSS. However post-deposition, PSS contributes to lower conductivity and hydrophilicty. Additionally, PSS has hygroscopic properties; this means that the material has the tendency to absorb water over time, which reduces the lifetime of PEDOT:PSS films exposed to air and moisture [96]. Döbbelin *et al.* showed that adding ILs to aqueously dispersed PEDOT:PSS resulted in hydrophobic cation exchange. They observed that PEDOT:PSS precipitated in water. Modified PEDOT:PSS films showed robust water resistance under a current of flowing water, whereas commercial PEDOT:PSS films were easily washed away [96]. In comparison, our results suggest that soaking PEDOT:PSS in the IL EMITFSI does not sufficiently remove PSS to improve water stability of our tri-layer actuators. However, the hydrophobic nature of the PEDOT:PSS films following treatment with organic solvents or a combination of organic solvents and EMITFSI, suggests that we removed PSS from the polymer films.

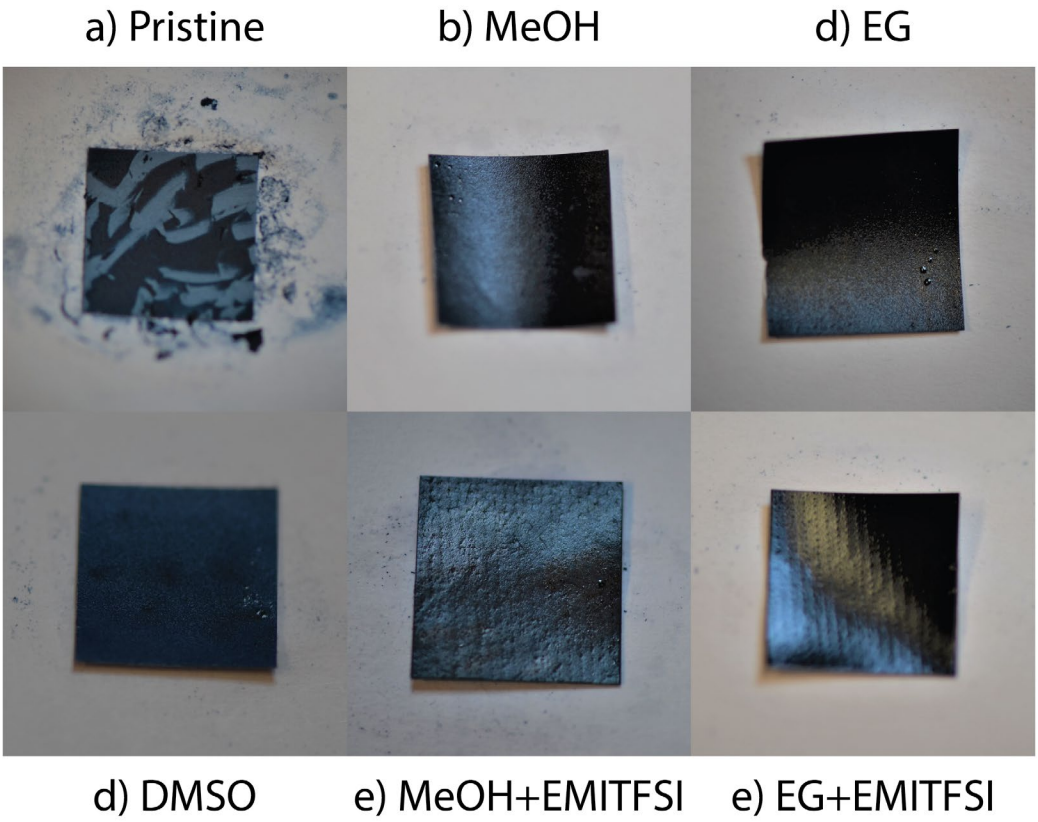

Figure 2-3 Water solubility of PEDOT:PSS/PVDF/PEDOT:PSS tri-layer actuators a) pristine and post-treatment with b) MeOH, c) EG, d) DMSO, e) MeOH+EMITFSI, or f) EG+EMITFSI. 1x1cm samples were soaked in deionized water for 1 minute then dried on paper. Images were captured using a Nikon D5100 DSLR Camera.

The improved stability of PEDOT:PSS/PVDF/PEDOT:PSS tri-layer actuators in water opens the opportunity to explore aqueous electrolytes, as an alternative to IL's. Oyedotum *et al.* reported that the aqueous electrolytes KOH and Na_2SO_4 showed a higher current response and ion mobility, compared to a protic1-ethylimidazolium bis(trifluoromethanesulfonyl)imide IL electrolyte. K^+ and Na^+ ions have higher diffusion coefficients, lower viscosities, and are smaller than the IL. These properties contributed to overall lower solution resistance, evident from lower real part impedance (Z') shown in the Nyquist plot [97]. This suggests that using aqueous salts instead of EMITFSI could improve the actuation speed of our devices. However, this study also

found that the IL had a larger electrochemical stability window of ~1.5 V compared to both $KOH_{(aq)}$ and $Na_2SO_{4,(aq)}$, which exhibited potential windows of ~0.4 V, due to electrochemical breakdown of water [97]. A study by Temmer *et al.* compared mechanical performance of various tri-layer actuators doped with either LiTFSI (an aqueous electrolyte) or EMITFSI (an IL). They found that LiTFSI yielded higher strain, actuation speed, and force generation – regardless of CP material. This was likely, in part, due to the lower viscosity of the aqueous electrolyte [38]. Unfortunately, aqueous electrolytes are also volatile, which necessitates an encapsulation step of our tri-layer actuators [38, 98]. In future work, we intend to investigate if replacing EMITFSI with an aqueous electrolyte improves the actuation response of our devices.

2.4 Mass and Density

This section reports how the mass of our PEDOT:PSS/PVDF/PEDOT:PSS tri-layer actuators changes following treatment and soaking in EMITFSI electrolyte. Here, we also report the average mass density of our samples following each treatment.

2.4.1 Methods

We used an analytical balance (Mettler Toledo, accuracy of 0.1 mg) to weigh each sample (3 per treatment). We then treated each sample following the process outlined in Section 2.1.2.2. After the sample appeared visibly dry, we weighed it again to determine the % mass change. Next, we saturated the sample in EMITFSI electrolyte and measured the % increase in mass. We used the equivalent glass slide PEDOT:PSS film thickness measured in Section 2.2 to determine the average density of each sample.

2.4.2 Results

Table 2-4 summarizes the results from this experiment. Treatment with pure organic solvents (MeOH, EG, or DMSO) decreased the mass of the tri-layer actuators. This suggests that

these treatments remove PSS from the polymer structure. Samples treated with an organic solvent plus IL (MeOH+EMITFSI or EG+EMITFSI) increased in mass. As expected, all samples increased in mass following post-treatment immersion in EMITFSI. However, this increase was smaller for the MEOH+EMITSI and EG+EMITFSI samples. These results suggest that residual EMITFSI remains in the tri-layers from the pre-treatment, which explains the smaller observed mass increase post-treatment.

Table 2-4 Summary of % mass change of PEDOT:PSS/PVDF/PEDOT:PSS tri-layer actuators untreated (pristine) or treated with MeOH, MeOH+EMITFSI, EG, EG+EMITFSI, or DMSO. Then % mass change following each sample soaking to saturation in EMITFSI. The average mass density ($\rho_{average}$) was calculated based on these measurements. S.E. refers to standard error.

Treatment	% Δ mass - treatment	S.E. (%)	% Δ mass - soaked	S.E. (%)	$\rho_{average}$ (g/cm^3)
Pristine	-	-	+113.4	-	10.2
MeOH	-3.5	0.7	+120.4	7.7	10.8
MeOH+EMITFSI	+107.8	17.4	+31.2	3.0	13.6
EG	-2.5	0.3	+119.5	1.4	10.7
EG+EMITFSI	+10.1	2.4	+97.5	3.6	9.2
DMSO	-4.7	0.4	+126.8	2.9	10.3

2.5 Electrical Conductivity

This section explores how PEDOT:PSS treatment with organic solvents or organic solvents combined with the IL EMITFSI affects electrical conductivity.

2.5.1 Methods

We fabricated a four-line probe set-up by sputtering 5nm/100nm thick Cr/Au on a glass microscope slide. This set-up consisted of four electrodes with a length equivalent to the width of the glass (~2.54 cm) and a width of (2.7 ± 0.25) mm. There was a (3 ± 0.25) mm space separating the inner and outer electrodes (L) and a (9.7 ± 0.25) mm gap between the inner electrodes. We pressed 1-cm x 3-cm tri-layer samples firmly over the four electrodes by tightly clamping a second glass microscope slide over the sample.

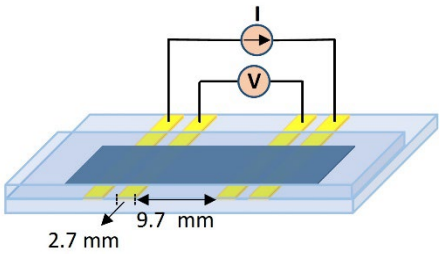

Figure 2-4 Schematic of experimental set up for electrical conductivity measurements (Information obtained from © 2019 Ebrahimi T. UBC [3]).

We applied a Galvano-dynamic measurement by applying a ramp current from -0.5 mA to +0.5 mA at a rate of 0.1-mA/s between the two outer electrodes. The change in voltage between the two inner electrodes was measured using a Solartron 1287A Potentiostat/Galvanostat (Hampshire, UK). We took three measurements per side of each sample. Linear regression on the Ohmic I-R curve allowed us to determine the electrical resistance (R_e) along the length of the sample, from the slope. We calculated sheet resistance ($R_{\square}$) using Equation (2-1):

$$R_{\square} = R_e \frac{W}{L}, \tag{2-1}$$

where the width (W) was (10 ± 0.25) mm for all measured samples. We then calculated the electrical conductivity of the PEDOT:PSS films (σ_e) using Equation (2-2):

$$\sigma_e = \frac{1}{R_{\square} h_p}. \tag{2-2}$$

For this analysis we used the equivalent thickness of PEDOT:PSS on glass slides (h_p).

We used samples coated with 20 layers of PEDOT:PSS for all the measurements. For each solvent treatment, we measure three separate 1-cm x 3-cm samples; both CP electrodes (each side of the tri-layer) were measured separately three times. Table 2-5 summarizes the parameters used in these measurements.

Table 2-5 Summary of parameters used for electrical conductivity measurements.

Parameter	Value
Width (W)	10 ± 0.25 mm
Length (L)	9.7 ± 0.25 mm
Number of Coats (n)	20
Polymer Thickness (h_p)	4.74 µm

2.5.2 Results

Figure 2-5a shows characteristically linear IR curves for each sample. Based on Ohm's law (V = IR), the slope equals electronic resistance, R_e. The pristine samples have the steepest slope, which corresponds to much higher resistance compared to samples that have undergone treatment. From these results, we calculated the conductivity, σ_e by assuming thickness, h_p, of each sample was equal to the equivalent film thickness of PEDOT:PSS sprayed on a glass slide – described in Section 2.2.2. Figure 2-5b illustrates the relative change in σ_e compared to the untreated samples following each treatment. The large error may be a result of differences in geometry, such as variable thickness or width, since we manually cut these samples.

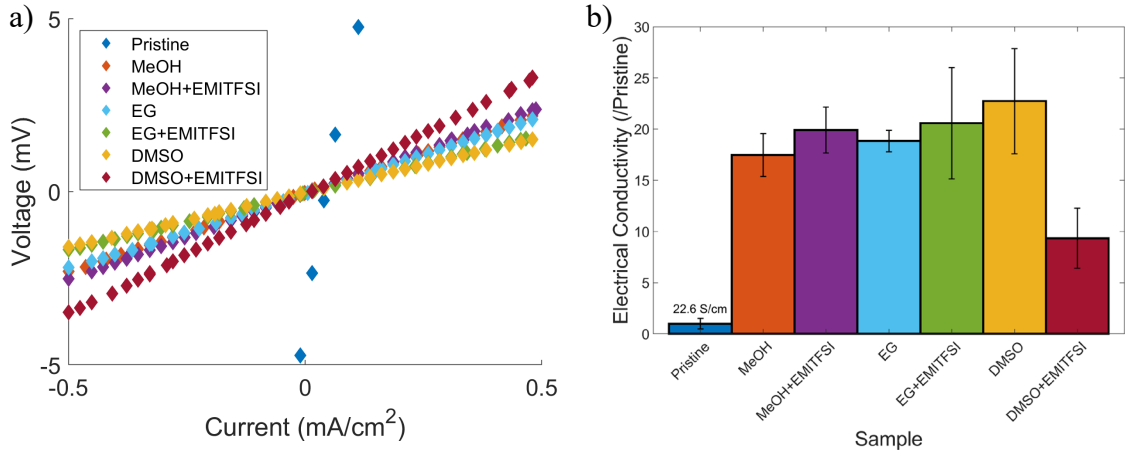

Figure 2-5 a) Representative I-V curves for each solvent treatment of PEDOT:PSS tri-layer actuators. b) Measured electrical conductivity of PEDOT:PSS films untreated relative to with solvent post-treatments (ratio of conductivities). The error bars represent standard error.

Pristine samples had a mean σ_e of (23.0 ± 11.1) S/cm. All post-treatments increased σ_e by one order of magnitude. DMSO and EG+EMITFSI reported the largest absolute conductivity measurements with values of (582.8 ± 130.8) S/cm and (522.8 ± 133.1) S/cm. However, these measurements also had high relative errors, which suggested these treatments were less reproduceable than MeOH- or pure EG-solvents. We also found that DMSO and EG sometimes delaminated the PEDOT:PSS from the PVDF membrane if the films were exposed to the solvents for 30 and 45 minutes. DMSO+EMITFSI was the least effective treatment, with a mean σ_e of (219.6 ± 68.4) S/cm, which was approximately half that of MeOH. This treatment also exhibited a high relative error, suggesting it had the potential to damage samples during post-treatment. Table 2-6 summarizes the R_e and σ_e results for each treatment.

Table 2-6 Tabulated values for electrical resistance (R_e) and conductivity (σ_e) with their respective errors for each solvent treatment of PEDOT:PSS tri-layer actuators.

Treatment	R_e (Ω)	R error (Ω)	σ_e (S/cm)	σ_e error (S/cm)
Pristine	90.6	43.6	23.0	11.1
MeOH	4.9	0.6	427.0	51.8
MeOH+EMITFSI	4.2	0.4	498.4	54.1
EG	4.4	0.2	471.4	26.0
EG+EMITFSI	4.0	1.0	522.5	133.1
DMSO	3.6	0.8	582.8	130.8
DMSO+EMITFSI	9.5	2.9	219.6	68.4

Our results are similar to previously reported values in literature on improving the electrical conductivity of PEDOT based tri-layer actuators. To our knowledge, the electrical conductivity we measured is the highest reported for PEDOT- and PEDOT:PSS- based actuators. Temmer *et al.* showed an effective conductivity of 176.7 S/cm for pure PEDOT electrodes [38]. In another study, Maziz *et al.* measured electrical conductivity of their untreated PEDOT electrodes for a 3.0 μm sample to be 36 ± 7 S/cm [23]. Despite the low conductivity they achieved, the actuators described in the latter study demonstrated high cut-off frequencies and a resonance peak at 930

Hz. This suggests that other mechanisms in addition to high electrical conductivity are also important to fast actuation. In their case, they used a separator layer that was ten times thinner than the PVDF layer used here, and all dimensions were small.

Some studies on tri-layer actuators investigated additives to improve electrical conductivity. Maziz *et al.* used the polar monomer polyethylene glycol methacrylate derivative (mPEG) as an additive for polymerization of PEDOT electrodes. These samples were also directly rinsed with MeOH [99]. Tri-layers fabricated using this method achieved maximum electrical conductivity values around 400 S/cm, which is within the lower range of conductivities measured for our samples. Samples that this research group synthesized without mPEG demonstrated conductivity values of 22 S/cm, which is also similar to the conductivity of our untreated samples. Nguyen *et al.* also investigated the glycol-based additive mPEG for improving PEDOT electrical conductivity. They observed an increase from 18 S/cm (in the untreated sample) to 164 S/cm (in the treated sample) [95].

In another study, Ikushima *et al.* investigated how various additives improve the electrical conductivity and overall performance of PEDOT:PSS-based tri-layer actuators. Similar to our findings, they observed that DMSO resulted in the largest increase in conductivity. However, they observed the caveat that DMSO immersion led to a high incidence of short-circuiting between the two electrodes and delamination – a trend that was also apparent in our experiments. In addition, this group reported an improvement to the conductivity of PEDOT:PSS by adding PEO to the aqueously dispersed solution, prior to deposition. Their results revealed that the higher the PEO concentration the higher the PEDOT:PSS conductivity but the lower the elastic modulus. To reduce the power loss due to the IR voltage drop along the length of the PEDOT:PSS films, the electrical conductivity must be high; however, to achieve large forces, the elastic modulus should

also be high [15]. Their untreated films demonstrated an electrical conductivity of 6.2 x 10^{-2} S/cm and at 1wt% PEO, they showed a 3 to 4 order of magnitude increase in conductivity [15]. This is a lower absolute magnitude but larger relative increase compared to the samples we fabricated.

Finally, Rohtlaid *et al.* studied the effect on electrical properties of PEDOT:PSS electrodes as a function of polyethylene oxide, PEO, content (0-60wt%). This additive increased the electrical conductivity of PEDOT:PSS from 1 S/cm to 163 S/cm at a concentration of 40 wt% PEO [90]. This showed that PEO enhances the conductivity of PEDOT:PSS; however, the treatments reported in our work achieved a higher absolute magnitude for conductivity by ~4 times.

Overall in this work, the peak conductivity values are consistent with those reported in the literature for treated PEDOT:PSS. The electrical conductivities are similar to but higher than those employed in other treated PEDOT:PSS tri-layer actuators. Next we show how these treatments increase ionic conductivity. We then explore how these results improve actuation.

2.6 Ionic Conductivity

Most studies looking to improve electrical conductivity of PEDOT:PSS focus purely on improving the electrical properties of the material for applications such as solar cells [58]. These studies do not also consider the ionic conductivity of the material and in most cases, faster ion transport is not desired in the polymer structure. Even within the CP tri-layer actuator literature, researchers rarely report ionic conductivity. Nguyen *et al.* determined the ionic conductivity of their PEO/NBR separator layer by measuring impedance at high frequencies. However, their model neglects to account for ionic conductivity of their CP electrodes [95]. We investigated how our post-treatments affected ionic conductivity because ionic resistance is a large source of impedance that increases the time constants of our actuators [33].

2.6.1 Methods

We conducted ionic conductivity (σ_i) measurements using an ionic four-channel diffusion set-up shown in Figure 2-6. This was a procedure previously described by Dobashi *et al.*, which allows for the separation of ion transport analysis in mixed electronically and ionically conducting membranes [100]. We immersed two platinum (Pt) electrodes (1-cm x 2-cm) in the EMITFSI solution at each of the two ends of the set-up, which served as the working and counter electrodes, through which we applied a ramp current from -0.5-mA to 0.5-mA. We used Ag/AgCl reference electrodes (BASi, MF-2021) placed into the two middle cannulas to measure the potential across the membranes. The ends of these reference electrodes were separated by a (9 ± 0.5) mm gap. The cross-sectional area through which ions and solution were able to transfer from one side of the membrane to the other (A) was equal to 0.65-cm^2.

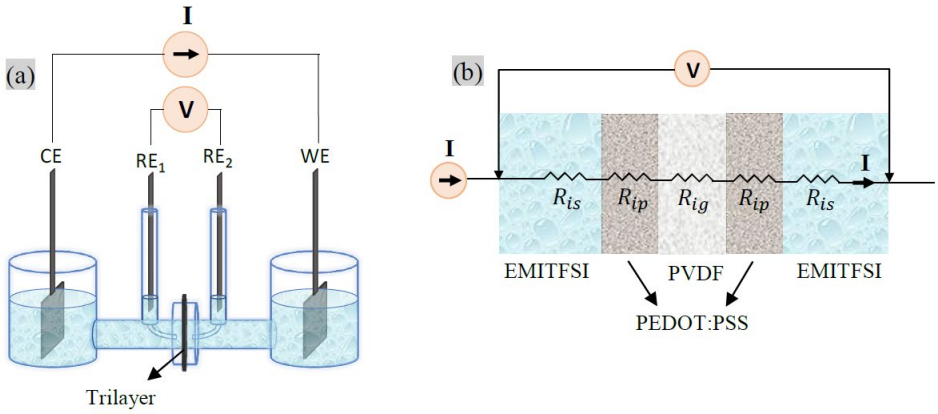

Figure 2-6 (a) Schematic of the set-up used for the four-probe ionic conductivity measurements. (b) The equivalent electric circuit model of ionic conductivity measurement setup (Information obtained from © 2019 Ebrahimi T. UBC [3]).

Prior to any measurements on the tri-layer samples, we applied a Galvano-dynamic analysis on the pure EMITFSI electrolyte without a membrane separating the electrodes. We applied a ramp current from -0.5-mA to +0.5-mA at a rate of 0.1-mA/s between the working and counter electrodes and measured the voltage change between the reference electrodes. These

measurements were performed to determine solution resistance (R_{si}) from the slope of the I-V plot. We then fixed a PVDF membrane (without deposited PEDOT:PSS) between the two parts of the experimental apparatus. We applied the same Galvano-dynamic parameters to measure the PVDF separator resistance (R_{ig}), which we also determined from the slope of the I-V plot. We conducted these initial measurements on each day we performed σ_i experiments, to account for fluctuations in room conditions, the age of the electrolyte, and any sources of error outside of our control. In particular, EMITFSI is hygroscopic, which means that it absorbs humidity over time and becomes more ionically conductive [3].

For samples with high σ_i, we conducted Galvano-dynamic measurements by applying a ramp current from -0.5-mA to +0.5-mA at a rate of 0.1-mA/s between the working and counter electrodes and measuring the potential difference between the two inner reference electrodes, using a Solartron 1287A Potentiostat/Galvanostat (Hamshire, UK). These samples exhibited a characteristically linear Ohmic I-V curve. We performed linear regression on the data to determine the total ionic resistance (R_i) from the slope. We ran three sequential measurements on each sample without disassembling the set-up.

We determined that some samples, for example the untreated samples, did not exhibit the characteristically linear Ohmic curve seen in pure resistors. This is likely because the current ramp rate was too fast to allow for charging within the CP layers. For these samples, we performed Galvano-static measurements by applying a constant current for a sufficient amount of time to allow full charging of the tri-layer, which was indicated by a plateau in the voltage vs. time curve. Constant currents from -0.5-mA to +0.5-mA in 0.1mA intervals were applied for 5-10 minutes. We then plotted the plateau voltage vs. current and performed a linear regression to determine R_i from the slope (Appendix C.1).

The dimensions of the samples we used in these measurements was 1.5 x 1.5 cm. Figure 2-6b shows the equivalent circuit model for the PEDOT:PSS/PVDF/PEDOT:PSS membrane immersed in EMITFSI electrolyte. The total ionic resistance of the membrane between the cannula ends (R_i) is equal to the sum the ionic resistance of EMITFSI (R_{is}), the PEDOT:PSS layers (R_{ip}), and the PVDF membrane (R_{ig}) according to Equation (2-3):

$$R_i = 2R_{is} + 2R_{ip} + R_{ig} \ . \tag{2-3}$$

The ionic conductivities of the EMITFSI electrolyte (σ_{is}), PVDF membrane (σ_{ig}), and PEDOT:PSS layers (σ_{ip}) were determined through Equation (2-4):

$$\sigma_{ij} = \frac{\Delta_j}{R_{ijA}}, (j = s, g, p) \ , \tag{2-4}$$

where Δ_s is the gap between the two inner cannulas equal to (9 ± 0.5) mm, Δ_g (= $h_g \approx$ 125-µm) is the thickness of the PVDF membrane, and Δ_p (= $2h_p$) is the equivalent thickness of PEDOT:PSS deposited on a glass slide and is based on the profilometry measurements in Section 2.2.2.

2.6.2 Results

Table 2-7 summarizes the measured ionic resistances and calculated ionic conductivities of pure EMITFSI electrolyte, PVDF soaked in EMITFSI, and PEDOT:PSS/PVDF/PEDOT:PSS tri-layer samples (1.5x1.5cm), using an ionic four-channel set-up, which measures the resistance of the system to diffusion of ions. The mean ionic conductivity of EMITFSI was (0.8 ± 0.06) S/m, which was in the range of values previously reported in literature [101, 102]. For example, Tokuda *et al.* measured the σ_i of EMITFSI at room temperature to equal 0.58 S/m [103]. We measured a mean ionic conductivity of the PVDF membrane of (0.56 ± 0.47) S/m, which was also similar to previously reported values using the same experimental set-up [100]. However, these results

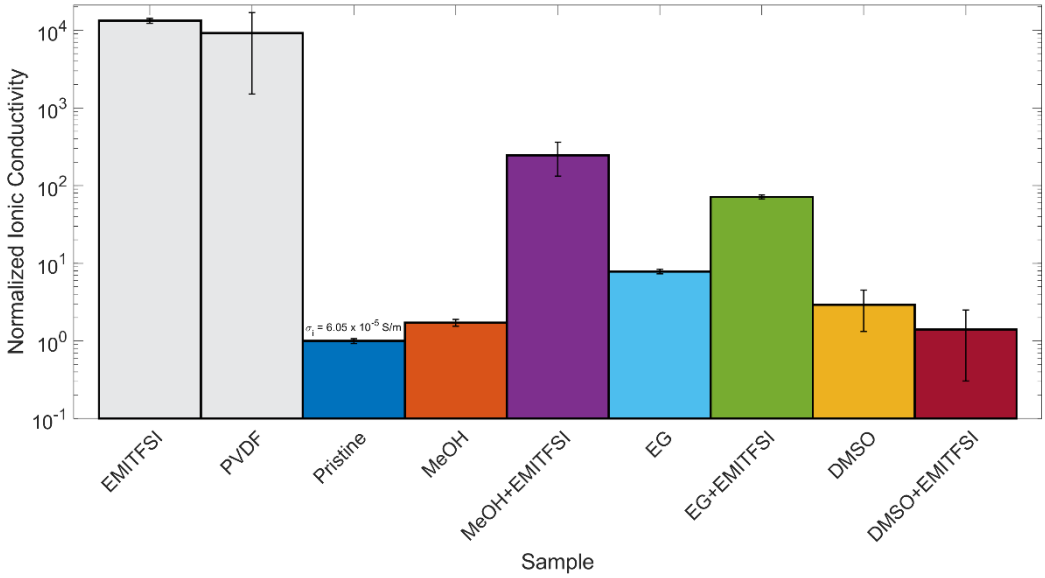

Figure 2-7 Measured ionic conductivity of PEDOT:PSS films with solvent post-treatments, relative to untreated PEDOT:PSS.

showed a large experimental variation, due to fluctuations in ambient conditions, such as air temperature, humidity, and apparatus set-up between days. We stored EMITFSI in a sealed container, to prevent water uptake due to air exposure as much as possible.

Table 2-7 Tabulated values for ionic resistance (R_i) and conductivity (σ_i) with their respective errors for each solvent treatment of PEDOT:PSS tri-layer actuators. Pure EMITFSI refers to measurements on this ionic liquid alone, without a separator membrane in the cannulas.

Treatment	R_i (Ω)	R_i error (Ω)	σ_i (S/m)	σ_i error (S/m)
Pure EMITFSI	172	9	0.80	0.06
PVDF	3.4	3	0.56	0.5
Pristine	1204	50	6.1E-05	4E-06
MeOH	703	60	1.0E-04	1E-05
MeOH+EMITFSI	4.9	2	1.5E-02	7E-03
EG	154	6	4.8E-04	3E-05
EG+EMITFSI	16.9	unknown	4.3E-03	2E-04
DMSO	410	220	1.8E-04	1E-04
DMSO+EMITFSI	860	670	8.5E-05	7E-05

Figure 2-7 compares the relative changes in σ_i for PEDOT:PSS tri-layer actuators with and without chemical post-treatments. For all samples, the PEDOT:PSS layers were the largest contributors to overall R_i and are therefore more rate limiting compared to the separator or pure

EMITFSI. For untreated samples, we reported an σ_i value of (6.05 ± 0.42) x10^{-5} S/m using galvanostatic measurements from -0.5 mA to 0.5 mA. We found that the solvent treatments we used to improve electrical conductivity of PEDOT:PSS also increased the σ_i. We observed that treatments with EMITFSI mixed with a polar solvent showed the most significant increase of σ_i. Treatment with MeOH+EMITFSI resulted in the largest change, increasing the σ_i by three orders of magnitude to (1.49 ± 0.69) x10^{-2} S/m. EG+EMITFSI increased σ_i by two orders of magnitude to (4.32 ± 0.24) x10^{-3} S/m. The polar solvents MeOH, EG, and DMSO increased σ_i by one order of magnitude, with values of (1.04 ± 0.10) x10^{-4} S/m, (4.75 ± 0.32) x10^{-4} S/m, and (1.77 ± 0.96) x10^{-4} S/m, respectively. The treatment DMSO+EMITFSI did not significantly improve σ_i and measurements were not reproduceable, resulting in a large experimental error. Pure DMSO treatments also reported highly variable results and a large error. This is consistent with our observations that over-exposure to DMSO damages the PEDOT:PSS films and reduces the electro-chemo-mechanical properties of the material.

Little work has been reported on enhancing σ_i of PEDOT:PSS. To the best of our knowledge, this is the first study that reports the effects of treatments of polar solvent +ionic liquid mixtures to improve the ionic conductivity of conducting polymers. Abdullayeva *et al.* used an aqueous solution of 5% Nafion^{TM} mixed with PEDOT:PSS to enhance proton transfer through electrochemically-overoxidized PEDOT:PSS. They observed that this treatment enhanced σ_i from 0.0035 to 0.13 S/cm [104]. This approach is different, as it adds a second, ionically conductive phase to the film. In another study, Liu *et al.* added diethylene glycol (dEG) to aqueously dispersed PEDOT:PSS prior to deposition. They used SEM to show these films pre-treated with dEG had more macroscale pores compared to pristine samples. These large pores were likely voids previously occupied by dEG, prior to drying. This study showed that the increased porosity of their

treated films resulted in better electrochemical performance in terms of specific capacitance, due to the increase in accessible surface area or better ion access to dope the PEDOT. They also showed that PEDOT:PSS-dEG films retained a highly rectangular cyclic voltammetry (CV) curve, even at high scan rates, which is indicative of high charge mobility [105]. These results corroborate our findings. Ours is the first direct measurement of the effect of polar solvents on ionic conductivity in PEDOT:PSS.

2.7 Cyclic Voltammetry

In this section, we present CV results for untreated and treated PEDOT:PSS/PVDF/PEDOT:PSS tri-layer actuators. We determined the volumetric capacitance (C_V) and electrochemical time constants (τ). These results show how chemical treatment with polar solvents or IL affect the charge storage capabilities and charge transfer rates of our devices.

2.7.1 Methods

The experimental apparatus for the CV measurements involved tightly clamping the 1.5-cm x 1.5-cm PEDOT:PSS/PVDF/PEDOT:PSS tri-layer samples between two gold foils (99.99%, 0.127-mm thick, SUREPURE CHEMETALS, L.L.C.) of approximately the same size. We used a two electrode set-up to apply a cycling voltage between -1V and +1V ($\Delta V = 2V$) at scan rates (υ) of (0.2, 0.4, 0.6, 0.8, 1, 2, 3, 4, and 5) V/s. We ran each test for 5 cycles and measured the current using a Metrohm Autolab® Potentiostat/Galvanostat. Additionally, for samples that appeared to charge slowly and thus did not exhibit a capacitive CV even at 0.2-V/s, we ran further CV measurements at 0.05 and 0.1 V/s.

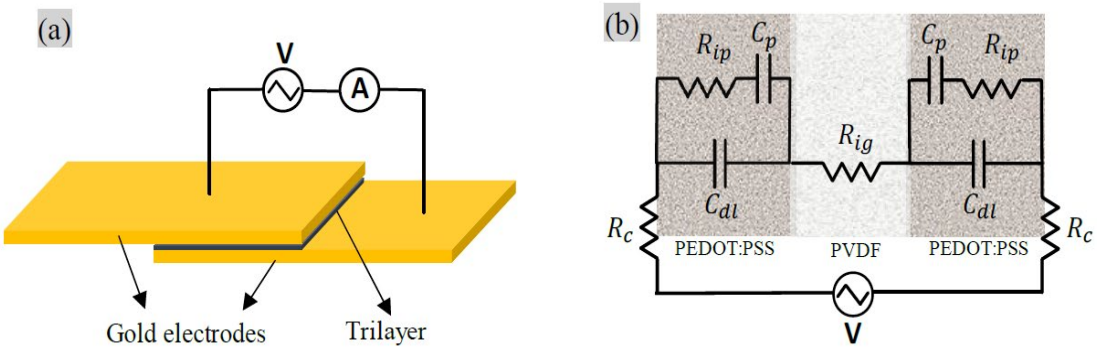

Figure 2-8 (a) Schematic of the experimental set-up for performing CV measurements, composed of the tri-layer actuators sandwiched between two gold foils. (b) The corresponding simplified 1D equivalent circuit model for the CV measurement set-up (Information obtained from © 2019 Ebrahimi T. UBC [3]).

Figure 2-8b shows the simplified 1D equivalent circuit model for the CV measurements. R_c is the sum of the contact resistance and any external resistance between the sample and power supply. R_{ip} and R_{ig} are the ionic resistances of the PEDOT:PSS and PVDF layers. C_P and C_{dl} represent the capacitance of the PEDOT:PSS layers and double layer capacitance respectively. Since C_{dl} (~ 20μF) << C_P, and assuming the two CP layers were symmetric, we calculated C_p through Equation (2-5) after the CP layers were charged (the voltage across the capacitors is equal to the applied voltage):

$$i = C\frac{dV}{dt}. \qquad (2\text{-}5)$$

In this specific context, we approximated the current ($\bar{I}$) to equal the difference between current values at 0-V for oxidation and reduction divided by 2 and υ = dV/dt. Therefore, we calculated C_V using Equation (2-6):

$$C_V = 2\frac{\bar{I}}{\vartheta(LWh_p)}\,. \tag{2-6}$$

Volumetric capacitance is the capacitance per unit volume of the polymer material.

We also determined time constants (τ) by fitting an exponential function to the rise time of each CV curve, according to Equation (2-7):

$$i = I_{Max}\left(1 - e^{-\frac{t}{\tau}}\right) + \varepsilon\,, \tag{2-7}$$

where *i* is the current, I_{Max} is the maximum current, and ε is the offset. the charging time (RC) of the system corresponds to 36.8% of the peak current. The current flow during actuation results from the addition or removal of charge on the primary chain of the polymer to maintain charge neutrality [22].

2.7.2 Results

2.7.2.1 Volumetric Capacitance

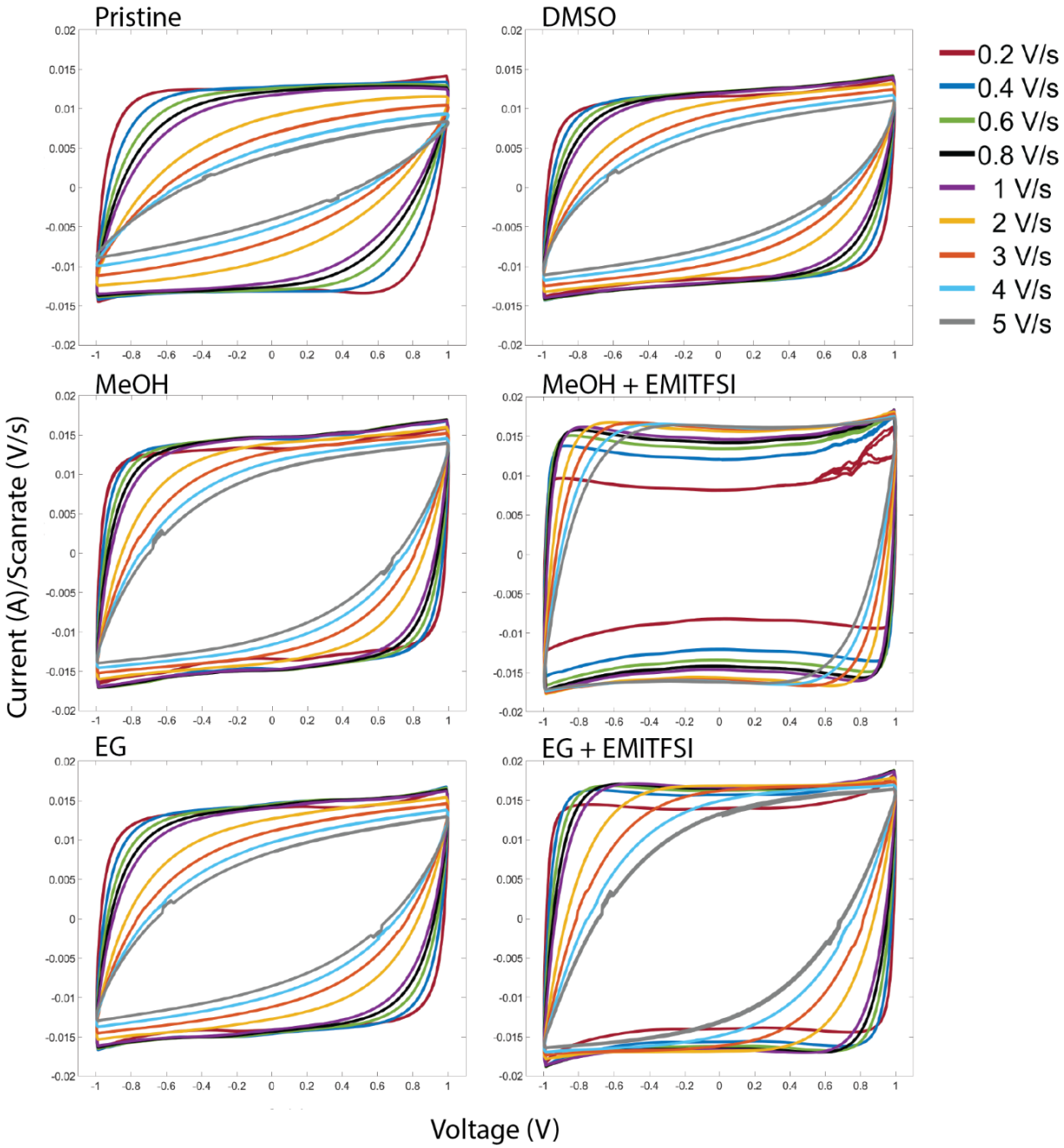

Figure 2-9 Cyclic voltammetry plots of current/scan rate versus voltage for pristine and treated samples with DMSO, MeOH, MeOH+EMITFSI, EG, or EG+EMITFSI. CV's were run at scan rates of 0.2, 0.4, 0.6, 0.8, 1, 2, 3, 4, and 5 V/s.

Figure 2-9 shows the CV curves for pristine and treated samples. At sufficiently low scan rates and from -0.8V to 0.8V for all samples, the CV curves were symmetric and rectangular, which indicated no redox reaction occurred during the charge and discharge of the PEDOT:PSS layers. The slight slopes of the graphs after the CP layers were charged between -0.8 to -1V and 0.8V to 1V, indicated a resistive region. This was likely indicative of leakage current passing through the PVDF membrane. We also suspected some degradation of the sample outside the electrochemical voltage window of -0.8 to 0.8 V occurred, which contributed to these resistive elements.

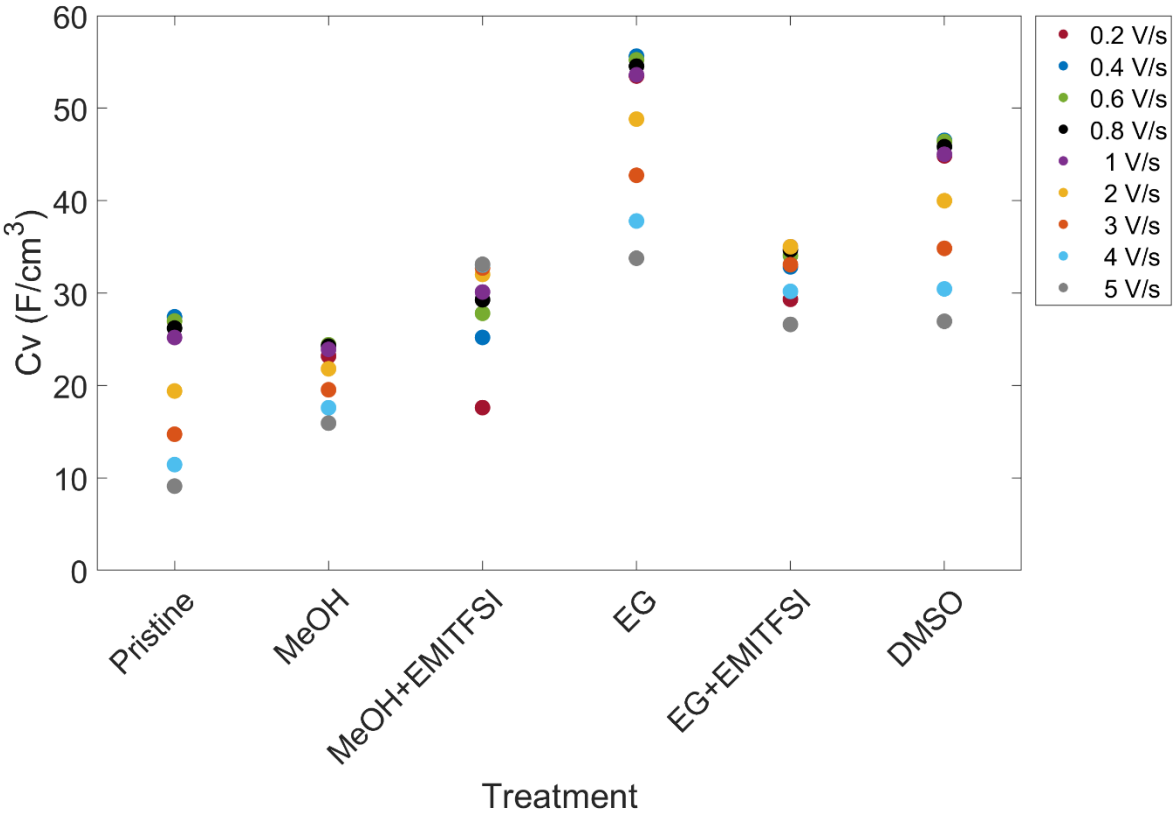

Figure 2-10 Volumetric capacitance (C_v) measured for each sample at scan rates from 0.05 to 5 V/s. C_v should be constant for all scan rates that allow sufficient time for charging, therefore the value at which C_v measured for each scan rate converges is the volumetric capacitance of the material.

We assumed the actuators behaved as pure capacitors and the two CP layers were symmetric. In Figure 2-10, we show the C_v calculated at each ν, based on Equation (2-6). Here, we observed a general trend in which C_V values increased then converged as ν decreased and the actuators charged fully. Theoretically, the C_v is independent of scan rate; however when the sample is not given sufficient time to charge (i.e. at scan rates faster than the time constant of the material), the measured C_v appears lower. Therefore, we took CV measurements across a range of scan rates and calculated at what maximum capacitance the values converged for each sample. We recorded the C_v's and convergence scan rates in Table 2-8.

Table 2-8 Summary of volumetric capacitance for untreated and post-treated PEDOT:PSS tri-layer actuators as well as the scan rates at which maximum charge storage was achieved for each sample.

Treatment	C_v (F/cm^3)	S.E. (F/cm^3)	υ (V/s)
Pristine	27.4	0.5	0.4
MeOH	24.4	1.3	0.6
MeOH_EMITFSI	33.1	0.9	5
EG	55.6	4.3	0.4
EG+EMITFSI	35.0	2.4	1
DMSO	46.5	3.0	0.4

We measured the C_v of untreated PEDOT:PSS/PVDF/PEDOT:PSS tri-layer actuators to have a value of (27.4 ± 0.5) F/cm^3 at 0.4 V/s. This value fell within the range previously reported in literature. For example, Ebrahimi T, *et al.* reported a C_v = (24.2 ± 0.4) F/cm^3 in her PhD thesis [3]. Additionally, Rivnay *et al.* studied the application of PEDOT:PSS in organic electrochemical transistors (OECTs) and measured a C_V value of (39.3 ± 1.3) F/cm^3 [106]. In our work, post-treatment with EG resulted in the highest C_v = (55.6 ± 2.4) F/cm^3 at 0.4 V/s. DMSO post-treatment also nearly doubled the C_v to a value of (46.5 ± 3.0) F/cm^3, also at 0.4 V/s. MeOH treatment had little effect on the C_v of the material, with a reported value of (24.4 ± 1.3) F/cm^3 at 0.6 V/s. The IL + polar solvent treatments EG+EMITFSI and MeOH+EMITFSI increased the C_v of PEDOT:PSS to a (35.0 ± 2.4) F/cm^3 and (33.1 ± 0.9) F/cm^3, respectively. Additionally, we

measured the peak C_v's of these samples at higher scan rates than untreated or pure polar solvent treated samples, which indicated that IL + polar solvent treated samples charged much faster. This was likely due to the higher ionic conductivities of these materials, which reduced the impedance to ion movement through the CP electrodes and allowed the ions to diffuse through the sample at a higher rate under an applied potential difference.

Measurements on DMSO+EMITFSI samples produced a characteristically resistive ohmic response, even at very low scan rates, which indicated that this treatment rendered the tri-layer actuators non-capacitive. Therefore, we could not determine the C_v for this post-treatment. As we have discussed previously, this was likely because over exposure to DMSO damaged the CP electrodes, which caused delamination or shorting through the thickness of the PVDF membrane. Based on these results, we chose not to perform further characterization measurements on PEDOT:PSS/PVDF/PEDOT:PSS tri-layer samples treated with DMSO+EMITFSI.

2.7.2.2 Electrochemical Time Constants

Figure 2-11 shows the initial rise times for current to reach a peak value and plateau. The vertical dashed lines indicate when time equals τ according to Equation (2-7). The rise times of all treated samples were shorter than that of the pristine samples. PEDOT:PSS treated with a mixture of polar solvent MeOH or EG and IL were significantly faster than those treated with pure polar solvent. MeOH+EMITFSI treated samples demonstrated the fastest rise time of $\tau = (0.04 \pm 0.0004)$ s. The trend in these results inversely matched that of the ionic conductivity results. As σ_i increased, τ decreased, which suggested that ionic conductivity played a large role in determining speed of actuation and cut-off frequencies. Table 2-9 summarizes the time constants and cut-off frequencies of each sample based on the rise time of the CV curves.

Table 2-9 Summary of time constants (τ) and cut-off frequencies (f_c) for untreated and treated PEDOT:PSS/PVDF/PEDOT:PSS tri-layer actuators based on rise time of the CV curves.

Treatment	τ (s)	S.D. (s)	f_c (Hz)	S.D. (Hz)
Pristine	0.29	0.02	0.55	0.05
MeOH	0.16	0.02	1.02	0.11
MeOH+EMITFSI	0.04	0.0004	4.08	0.04
EG	0.20	0.03	0.80	0.10
EG+EMITFSI	0.10	0.002	1.53	0.04
DMSO	0.21	0.02	0.77	0.09

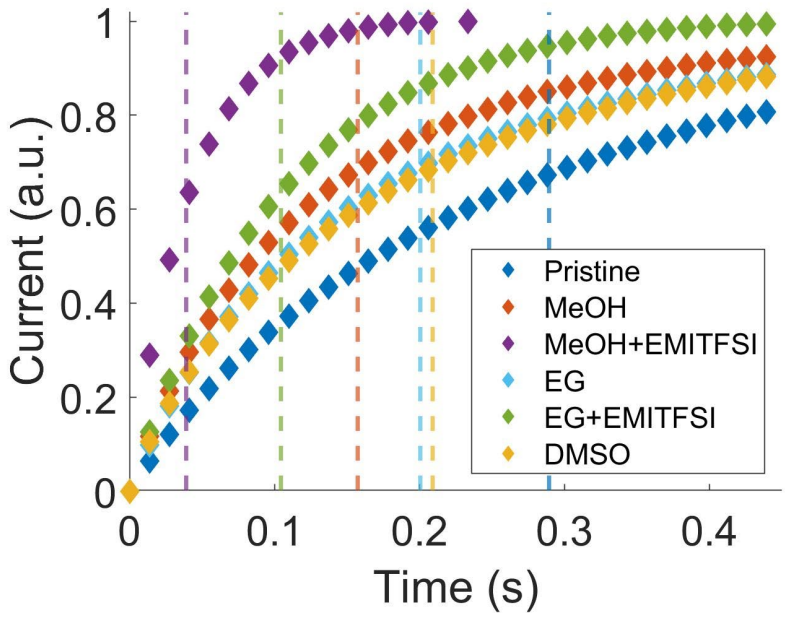

Figure 2-11 Normalized current vs. time under an applied ramp voltage of 1V for a CV taken with a scan rate of 0.6 V/s for pristine and treated samples with MeOH, MeOH+EMITFSI, EG, EG+EMITFSI, and DMSO. This shows the rise time of each treatment. The electrochemical RC time constant occurs at when $I_{Max}(1\text{-}e) \approx 0.37I_{Max}$. The colour-coded dashed lines correspond to the time constants for each treatment.

2.8 X-ray Photoelectron Spectroscopy

In this section, we used the surface characterization technique X-ray photoelectron spectroscopy (XPS) to analyze how each chemical treatment affected the near surface chemistry of our samples.

2.8.1 Background

We used X-ray photoelectron spectroscopy (XPS) to analyze the near surface chemistry of the PEDOT:PSS/PVDF/PEDOT:PSS tri-layers for untreated and post-treated samples. XPS is a non-destructive characterization technique, based on the phenomenon of external photo-effect, used for assessing surface chemistry, bonding structure, and relative composition. Monochromatic x-ray radiation bombards the sample surface with photons, which excites core electrons at discrete energy levels. Emission of these core electrons in the sample only takes place if the energy acquired from the photons (hυ) exceeds the minimum energy necessary to overcome the binding energy of the electron (E_B). This is the work required for the electron to escape from the surface [107]. The XPS analyzer detects the kinetic energies (E_{kin}) of the emitted photoelectrons, Einstein's relation for conservation of energy allows us to directly calculate E_B using Equation (2-8) :

$$E_B = h\nu - E_{kin} \, . \tag{2-8}$$

Each element has a unique set of associated core-level peaks that allow for unambiguous identification. XPS spectra provide information on elemental composition and relative atomic concentration. Peaks in the spectra correspond to the fraction of ejected core-level electrons that preserved their original energy on their way to the detector (did not collide). Binding energies of core-level electrons also depends on the chemical environment of their corresponding atoms, which results in chemical shift. This chemical shift indicates the oxidation state of the elements, which allows for the determination of bonding structure, and any changes in this structure as a result of surface treatment or sample processing [107]. Information about chemical bonds

identified in XPS spectra results is usually extracted by comparing the measured E_B values to literature or data base libraries [108].

XPS notation for core-level signals follows the convention "X nl_j", where X denotes the element, n is the principal quantum number (n = 1, 2, 3, …), l is the angular quantum number (s, p, d, f), and j is the total angular momentum quantum number equal to the sum of angular and spin orbital projection (s = ±1/2) quantum numbers ($j = l + s$). All core-level signals with $l \geq 1$ have a form of spin-split doublets with corresponding theoretical area ratios that are fixed. For example, S 2p splits into S $2p_{3/2}$ and S$2p_{1/2}$ with a respective area ratio of 2:1 [107].

2.8.2 Methods

2.8.2.1 Data Collection

We performed XPS measurements using a monochromated X-ray Al Kα source (Omicron XM 1000, hυ = 1486.6 eV). Photoelectrons were detected with an Omicron Sphera electron analyzer in an ultra-high vacuum system (P ~ 10^{-9} mbar). We initially recorded a wide range survey spectrum of each sample for energies ranging from 36.7 to 1286.7 eV, to obtain signatures for all elements in the sample. For all samples we detected carbon, oxygen, and fluorine, in addition to sulfur [108]. We expected to see contributions from these elements and none of their corresponding peaks interfered in the spectrum range of sulfur. Subsequently, we performed narrow-region high-energy resolution scan from 126.7 to 186.7 eV, which is the energy range we expected to observe sulfur peaks [61, 76, 108].

2.8.2.2 Background Subtraction

A large source of error associated with determining the chemical composition of a surface using XPS is related to the reliable measurement of peak areas and intensities. This breaks into two aspects: (1) spectra acquisition procedure, and (2) background subtraction [107]. Inelastically

scattered photoelectrons, that have lost energy through inelastic collisions, contribute to the step-like background shape. Previous work extensively studies how to separate the XPS signal into the elastic peak (< 5% of total electrons intensity) and inelastic background (> 95% of total electron intensity) [107, 109]. The background subtraction function has a direct effect on peak areas. Well established methods include: linear [110], Shirley [111], and Tougaard [109, 112] backgrounds These techniques do not require preliminary knowledge of aspect such as peak shape and spectrum structure. Linear-subtraction, is the simplest method; however it lacks theoretical grounds and makes the peak area dependent on arbitrarily selected start and end points. The widely applied Shirley method assumes that the number of inelastically scattered electrons contributing to the background increase is directly proportional to the total photoelectron flux. The more complicated and controversial Tougaard method relies on the quantitative description of inelastic scattering. It provides an estimate of area mostly independent of upper and lower end point selections [107, 113].

Unsworth *et al.* applied a Shirley background to their XPS spectra analyzing PEDOT:PSS the impact of DMSO treatment on surface composition [76]. This method is based on an iterative solution of equations with a selected kinetic energy above ($E_{K,right}$, I_{right}) and another below ($E_{K,left}$,I_{left}) of the peaks described by Equation (2-9) [114, 115]:

$$\begin{aligned} B_{SS,1}(E_K) &= k_{SS,1} \int_{E_K}^{E_{K,right}} dE'_K \left[I(E'_K) - \left(I_{right} \right) \right], \\ B_{SS,2}(E_K) &= k_{SS,2} \int_{E_K}^{E_{K,right}} dE'_K \left[I(E'_K) - \left(I_{right} \right) - B_{ss,1}(E'_K) \right], \\ B_{SS,n}(E_K) &= k_{SS,n} \int_{E_K}^{E_{K,right}} dE'_K \left[I(E'_K) - \left(I_{right} \right) - B_{ss,n-1}(E'_K) \right], \\ &\text{For } E_{K,left} \leq E_K \leq E_{K,right}, \end{aligned} \tag{2-9}$$

where $B_{ss,n}$ is the n^{th} iteration of the Shirley background, E_K is the kinetic energy, $I(E_K)$ is the intensity signal at E_K and $k_{SS,n}$ [units: eV^{-1}] is the n^{th} iteration value of the scattering factor, which measures the strength of the background as is independent of the vertical scale, as described by Equation (2-10):

$$k_{SS,n} = \frac{I_{left} - I_{right}}{\int_{E_{K,left}}^{E_{K,right}} dE'_K [I(E'_K) - (I_{right}) - B_{ss,n-1}(E'_K)]} . \quad (2\text{-}10)$$

The total background is the sum of a baseline (equal to I_{right}) and $B_{SS,n}$. The iterative process ends when the difference between $B_{ss,n}$ and $B_{ss,n-1}$ is negligible.

2.8.2.3 Modelling

Sophisticated GUI software, such as CasaXPS, exist for fitting XPS. However, these programs are complicated and offer a "black-box" approach to analysis. This often results in the development of fit models that are difficult to interpret and lack physical meaning [107, 116]. We developed our own model using MatLab to deconvolve our XPS spectra for the S 2p peaks correlated to oxidation states in of the thiophene S in PEDOT and the sulfonate S in PSS. In this analysis we took the following steps:

1) Shirley background subtraction.
2) Normalization of BE intensity to values from [0 1] with arbitrary units.
3) Optimization of data to a Gaussian model fit.
4) Calculation of peak areas correlated to relative concentrations of PSS to PEDOT.

We observed chemical shifts and BE splitting between spin-split components due the two different oxidation states of S in PEDOT:PSS. We applied constraints to our model that account for the underlying physics, such as the fixed relationships from the spin-orbit contributions of S $2p_{3/2}$ and S $2p_{1/2}$ described in Equations (2-11)-(2-14):

$$A_T = A_{S\,2p_{1/2}} + A_{S\,2p_{3/2}} , \quad (2\text{-}11)$$

$$A_i = I_i\sqrt{\pi w_i}, \quad i = T, S\ 2p_{1/2}, S\ 2p_{3/2}\ , \tag{2-12}$$

$$I_{S\ 2p_{3/2}} = 2I_{S\ 2p_{1/2}}\ , \tag{2-13}$$

$$w_{S\ 2p_{3/2}} = w_{S\ 2p_{1/2}}\ , \tag{2-14}$$

where A_T, $A_{S\ 2p_{1/2}}$, and $A_{S\ 2p_{3/2}}$ refer to the total peak and split-spin orbital peak areas. I_i and w_i refer to the peak intensities and full width half maximums (FWHM), respectively. These relationships allow for analytical consistency between multiple data sets. We used the *fmincon* function in the MATLAB R2020b optimization toolbox to fit four split-spin orbital peaks (S $2p_{3/2}$ and S $2p_{1/2}$ for PEDOT and PSS) to a Gaussian line-shape described by Equation (2-15):

$$I(E) = I_i e^{-\left[\frac{E-E_{Bi}}{w_i}\right]^2}, \quad i = T, S\ 2p_{1/2}, S\ 2p_{3/2}\ , \tag{2-15}$$

where I(E) is the intensity at a given BE (E) along the XPS spectrum, I_i is the peak intensity, and E_{Bi} is the peak BE. We identified the values of E_B, $E_{B\ 2p_{1/2}}$, and $E_{B\ 2p_{3/2}}$ from previously reported literature on PEDOT:PSS surface characterization [61, 76], which are outline in Table 2-10. We specified the intensity of each S 2p peak as the maximum measured intensity from the normalized

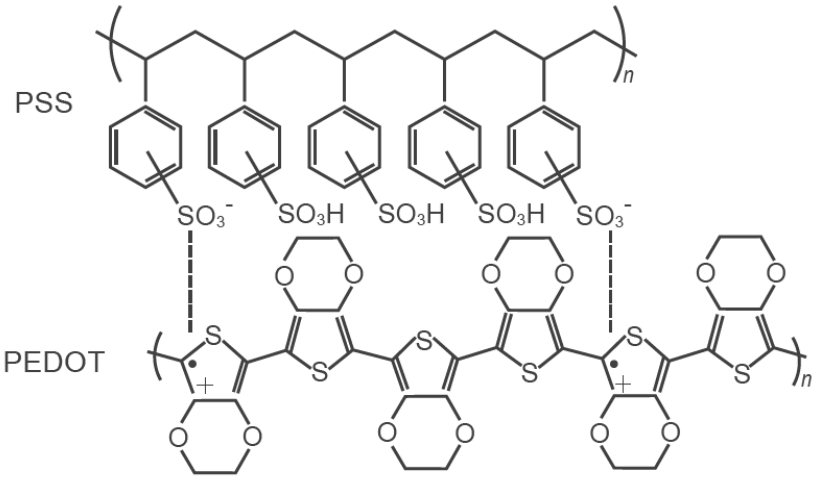

Figure 2-12 Chemical structure of PSS (top and PEDOT (bottom). A chemical shift in S 2p peak occurs as a result of the different oxidation states of S in PSS and PEDOT.

data. The unknown variables in this model include: A_T, $A_{S\,2p_{1/2}}$, $A_{S\,2p_{3/2}}$, $I_{S\,2p_{1/2}}$, $I_{S\,2p_{3/2}}$, FWHM$_T$, $FWHM_{S\,2p_{1/2}}$, and $FWHM_{S\,2p_{3/2}}$.

Table 2-10 Binding Energies for S 2p peaks corresponding to PSS and PEDOT.

Peak	Binding Energy (eV)	
	PSS	PEDOT
S 2p	168.7	164.8
S 2p$_{1/2}$	168.5	164.0
S 2p$_{3/2}$	168.7	164.7

The cost function in our model, which we wanted to minimize, was the mean squared error between the measured data and the curve fit of the sum of split-spin orbital Gaussian peaks described by Equation (2-16):

$$MSE = \frac{1}{n}\sum_{i=1}^{n}(I(E)_{measured} - I(E)_{model})^2 . \quad (2\text{-}16)$$

We calculated relative surface composition of each sample by first calculating the areas of the PEDOT and PSS peaks using Equation (2-12), then dividing these values to identify to ratio of PSS to PEDOT.

2.8.3 Results

Figure 2-13a-c illustrates the results from XPS analysis. Table 2-11 summarizes the relative composition results based on the integrated the S 2p peak areas for PEDOT and PSS and the respective ratios ($R_{S/T}$, where S refers to sulfonate and T refers to thiophene). The untreated PEDOT:PSS.PVDF/PEDOT:PSS sample had a $R_{S/T}$ of 21.8. The sample treated with 50% (v/v) EG and EMITFSI reported the lowest $R_{S/T}$ value of 7.57, which corresponds to a 7.3% decrease in PSS concentration. Treatment with MeOH+EMITFSI also reported a relatively large change with an $R_{S/T}$ value of 10.54, which corresponds to a 4.3% decrease in PSS concentration. Treatments with DMSO and DMSO+EMITFSI did not show significant changes in composition (% composition increases = 0.63% and 0.37%, respectively).

Previous work characterizing the changes to surface composition of PEDOT:PSS treated with DMSO showed large decreases in $R_{S/T}$. For example, Unsworth *et al.* observed up to a 40% decreases in the PSS component following the immersion of PEDOT films in DMSO [76]. Overall, our $R_{S/T}$ values were approximately 10x higher than those previously reported in literature [61, 76]. These discrepancies are likely because we saturated all samples (including the pristine samples) in EMITFSI electrolyte, which replaced PSS^- as the charge balancing ion in the polymer structure. Therefore, the EMITFSI also resulted in some removal of PSS from the untreated sample. Additionally, EMIFSI contains a sulfonate bond; however, since all samples were saturated in the IL, we assumed any discrepancies in the sulphonate S 2p peak between samples was a result of PSS removal. The results from this analysis further support our observations from sections 2.3 (water solubility) and 2.4 (mass change) that PEDOT:PSS treatment with organic solvents and ionic liquids remove hydrophilic and insulating PSS^- from the polymer structure. This removal enhances both the electrical and ionic properties of tri-layer actuators for high-speed applications (Full XPS results available in Appendix C.4).

Table 2-11 Summary of peak areas corresponding to PSS and PEDOT, the ratios of PSS to PEDOT, and mean squared error of the Gaussian model to the measured XPS spectrum data.

Sample	Area PSS	Area PEDOT	$R_{S/T}$ (PSS to PEDOT)	MSE
Pristine	2.25	0.10	21.84	0.00057
MeOH	2.29	0.15	15.67	0.00037
MeOH+EMITFSI	2.29	0.22	10.54	0.00082
EG	2.27	0.17	13.37	0.00038
EG+EMITFSI	2.31	0.31	7.57	0.00058
DMSO	2.24	0.087	25.73	0.00075
DMSO+EMITFSI	2.27	0.095	23.96	0.00039

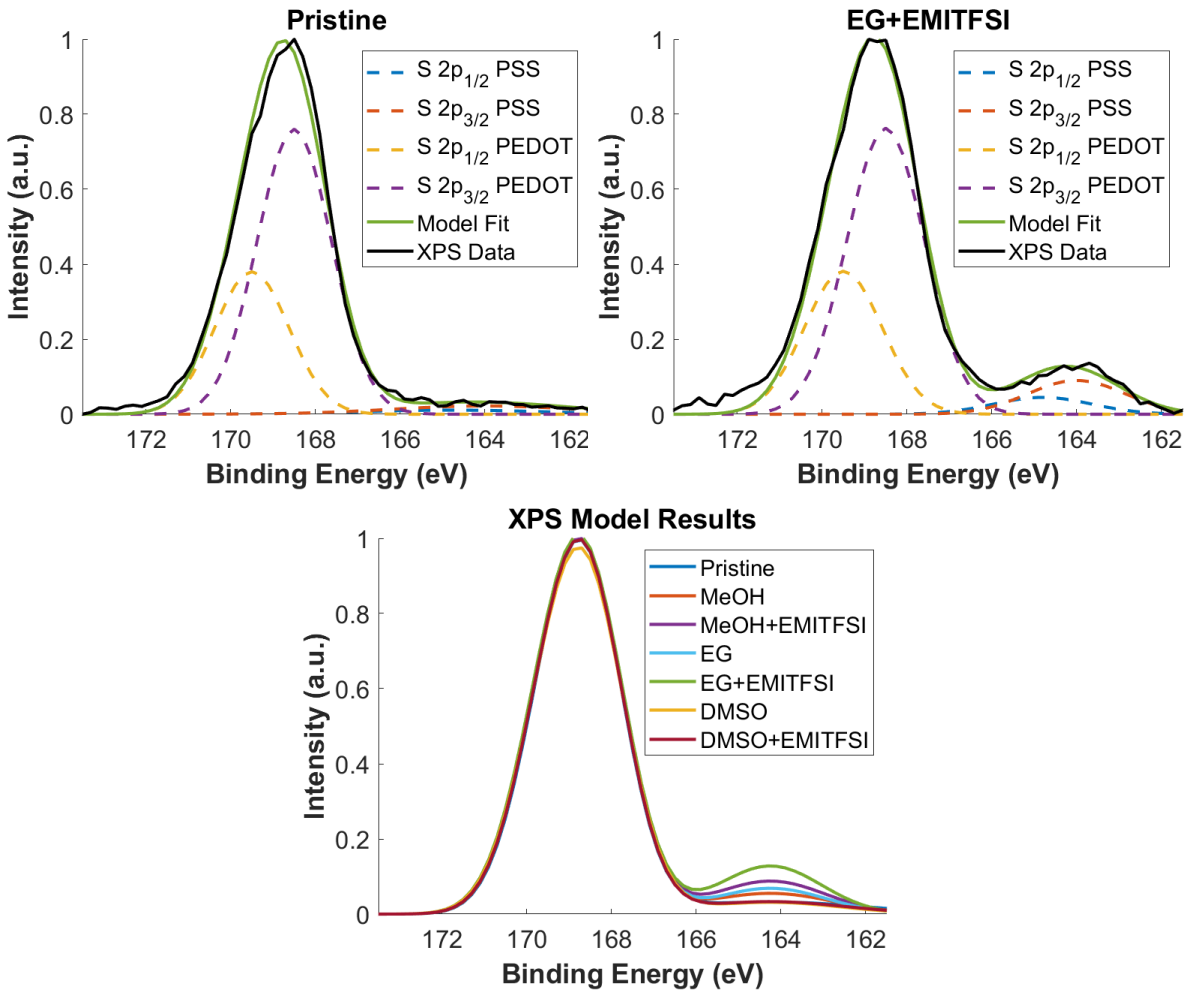

Figure 2-13 Normalized XPS results for analysis of untreated and post-treated PEDOT:PSS/PVDF/PEDOT:PSS tri-layer actuators soaked in EMITFSI. a) Normalized XPS spectra and Gaussian model for a pristine sample. b) XPS spectra and Gaussian model for sample treated with a 50% (v/v) mixture of EG and EMITFSI. c) Normalized Gaussian curve fit to experimental data for the spectra of untreated and post-treated samples.

2.9 Conclusion

In this section we analyzed the electrochemical performance of PEDOT:PSS/PVDF/PEDOT:PSS tri-layer actuators. We first listed the materials and fabrication processes we used to design these devices. We treated the PEDOT:PSS with MeOH, MeOH+EMITFSI, EG, EG+EMITFSI, or DMSO. Next, we performed initial profilometry measurements, which showed that PEDOT:PSS film thickness increases linearly with the number of coats spray coated and that polar solvent chemical treatment did not change the deposited film thickness. Our results showed that the chemical treatments described in this chapter significantly improved both electrical and ionic conductivities of the conducting polymer. We determined time constants and volumetric capacitance of each sample through cyclic voltammetry measurements. These results showed that MeOH+EMITFSI and EG+EMTIFSI treatments resulted in the fastest current rise times. Polar solvents without EMITFSI had the largest effect on increasing volumetric capacitance. Finally, XPS analysis showed that the treatments reduced the ratio of PSS to PEDOT on the surface of the samples. This suggests that the improvement to electrical conductivity we observed is due to the removal of insulating PSS from the material. In Chapter 3, we show how these improvements to the electrochemical properties of PEDOT:PSS improved the actuation mechanics and speed of our CP tri-layer actuators.

Chapter 3: Mechanical Characterization

In this chapter, we discuss the mechanical characterization of PEDOT:PSS/PVDF/PEDOT:PSS tri-layer actuators. We first determine how the polar solvent and IL treatments described in Chapter 2 effect the Young's modulus of PEDOT:PSS. Next, we show the actuation-frequency response for these tri-layers. We analyze how parameters such as voltage amplitude, beam length, and chemical treatment impact mechanical performance. Additionally, we use electrochemical impedance spectroscopy (EIS) to analyze the contributions from resistive and capacitive equivalent circuit elements. These data allow us to identify characteristic time constants that contribute to a drop in mechanical performance as frequency increases. Finally, we predict the maximum force generation of these devices, based on the analytical electro-chemo-mechanical model Actuatool, which was previously developed by Ebrahimi T. *et al.* [3].

3.1 Young's Modulus

In this section, we present results from uniaxial tensile test measurements, which we used to determine the Young's Moduli of untreated and treated samples.

3.1.1 Methods

We measured the Young's moduli of the tri-layer samples soaked in EMITFSI pre- and post-treatment, though uniaxial stress-strain measurements using a Bose ElectroForce®-3100 system in tension mode (a strain of 0.5% at 0.1 Hz for 5 cycles). The width (W) of all the samples was (10 ± 0.25) mm and the length (L_i) under tension was (20 ± 0.25) mm. We unmounted and remounted each sample between measurements to account for experimental error. We also performed stress-strain analysis on a pure PVDF sample soaked in EMITFSI of the same dimensions.

We used linear regression to calculates the material stiffness (K) from the slope of the force vs. displacement curve for each sample (Appndix C.3). The Young's Modulus of the PVDF membrane (E_g) was calculated using Equation (3-1):

$$E_g = \frac{K_g L}{h_g W}, \tag{3-1}$$

where K_g and h_g are the stiffness and the thickness of the PVDF membrane, respectively.

To find the Young's modulus of the PEDOT:PSS layers, we used the equivalent thickness deposited on the glass slides for 20 coats. The stiffness of the tri-layer actuator (K_T) is express using Equation (3-2):

$$K_T = K_g + 2K_P, \tag{3-2}$$

where K_P is the stiffness of each CP layer. To determine the Young's modulus of PEDOT:PSS we used equation (3-3):

$$E_P = \left(\frac{K_P}{h_P}\right)\left(\frac{W}{L}\right). \tag{3-3}$$

3.1.2 Results

Table 3-1 and Figure 3-1 summarize the Young's moduli for the PVDF membrane, PEDOT:PSS untreated, and with solvent post-treatments. The modulus of pure PVDF soaked in EMITFSI was (77 ± 7.33) MPa, which agrees with previously reported values [3, 26]. For Pristine PEDOT:PSS, we measured a Young's modulus value of (1.68 ± 0.185) GPa, which is also within the range of previously reported values of 0.9 to 2.8 GPa [3, 47].

Table 3-1 Summary of Young's Moduli for untreated and post-treated PEDOT:PSS tri-layer actuators.

Treatment	E_P (MPa)	S.D. (MPa)
PVDF	77.8	7.3
Pristine	1680.8	185.8
MeOH	2459.9	437.3
MeOH+EMITFSI	849.1	244.7
EG	2527.3	594.6
EG+EMITFSI	887.9	55.5
DMSO	2161.2	579.3
DMSO+EMITFSI	2331.1	542.2

We found that treatments with the pure polar solvents (MeOH, EG, and DMSO) increased the Young's Modulus of the material. Samples that received EG and MeOH post-treatments showed the highest value of (2.53 ± 0.595) GPa and (2.46 ± 0.437) GPa, respectively. Conversely, samples that received post-treatment with a mixture of polar solvent and ionic liquid (with the exception of DMSO+EMITFSI) showed a decrease in Young's moduli to approximately half that of untreated films.

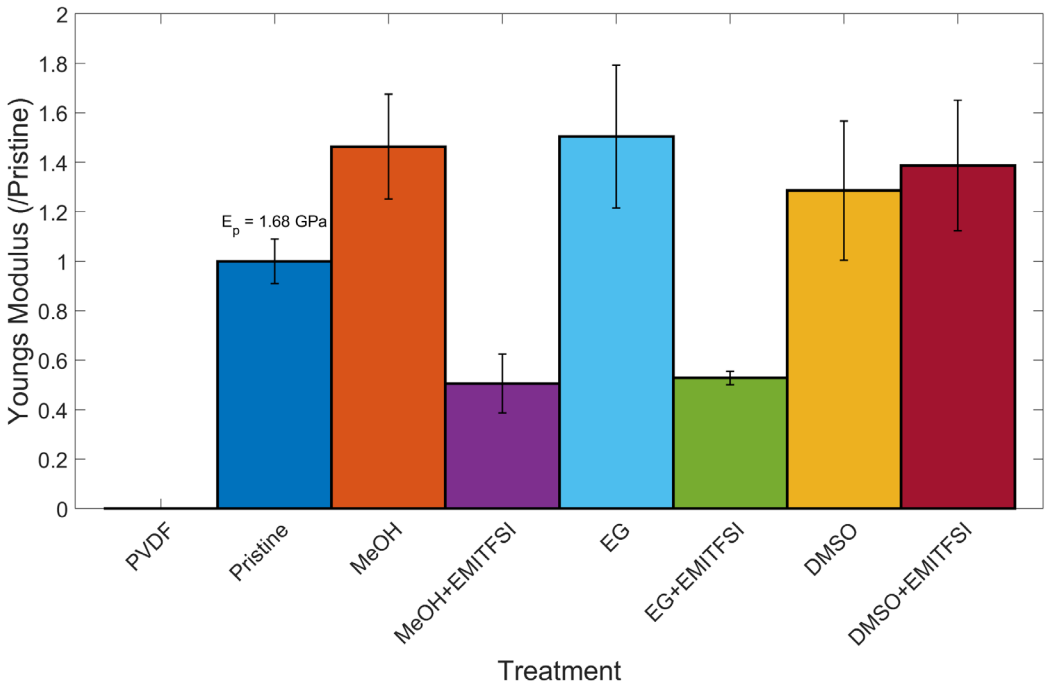

Figure 3-1 Young's moduli of PVDF, untreated and post-treated PEDOT:PSS tri-layer actuator samples.

To our knowledge, no previous studies look at the effects on PEDOT:PSS Young's modulus following post-treatments with polar solvent - ionic liquid mixtures. Teo *et al.* showed that the IL 1-ethyl-3-methylimidazolium tetracyanoborate (EMIM TCB) added to aqueous PEDOT:PSS was a plasticizer for the CP. In addition to improving the electrical conductivity, IL incorporation improved the stretchability up to 50% strain on a PDMS substrate [87]. Another study by Döbbelin *et al.* also showed that adding IL's to PEDOT:PSS decreased the stiffness of deposited films [96]. This supports our results that show IL treatment decreased the Young's modulus of PEDOT:PSS. There are trade-offs to increasing versus decreasing the stiffness of the actuators. Higher stiffness correlates to higher generated forces, but lower strain [15]. We will explore these trade-offs later in this Chapter.

3.2 Actuation Frequency Response

In this section, we show how electrical conductivity treatments with polar solvents and IL's effect the mechanical frequency response of the CP tri-layer actuators.

3.2.1 Methods

We applied a sine wave voltage to the two conductive sides of the tri-layer actuators clamped tightly between gold electrodes using a Solartron 1287A Potentiostat/Galvanostat (Hampshire, UK), with a Solartron 1260A Frequency Response Analyzer. The area in contact with the gold was 6-mm^2. We measured displacement of the 2-mm x 12-mm beam using a laser displacement sensor (Keyence LK-G32), with a minimum resolution of 50-nm. We painted a silver reflective point 1 cm from the fixed end of the actuator, which was illuminated with the laser. We measured peak-to-peak actuator displacement at frequencies between 0.01-Hz to the maximum frequency at which displacement was detected by the laser sensor (full SOP available in Appendix

B.2). We used MATLAB R2020b to detrend the measured data to account for drift and noise. We then fit a sine wave function to the data to determine the peak-peak displacement at each frequency.

3.2.2 Analysis

Strain

As discussed in Section 1.5.2, the peak-to-peak displacement represents the full range of motion of the actuators during one voltage cycle. The differential external strain, $2\epsilon_{ex}$, is calculated from Equation (3-4):

$$2\epsilon_{ex} = \frac{2Dh}{D^2+L'^2}, \tag{3-4}$$

where D is half of the peak-to-peak displacement, h is the thickness of the tri-layer swollen in electrolyte, and L' is the length at which the laser is illuminating from the base of the actuator.

The differential free strain, 2ϵ, is calculated from the external strain using Equation (3-5):

$$2\epsilon = 2\epsilon_{ex}\frac{h_p}{h}\left[\frac{nm^3+6m^2+12m+8}{6(m+1)}\right] = \frac{2Dh_p}{D^2+L'^2}\left[\frac{nm^3+6m^2+12m+8}{6(m+1)}\right], \tag{3-5}$$

where h_p is the thickness of the conducting polymer layer swollen in electrolyte, $m = h_g/h_p$ is the ratio of swelled thickness of the separator and conducting polymer layers, and $n = E_g/E_p$ is the ratio of swelled Young's moduli of the separator and conducting polymer layers.

While the external strain only accounts for the displacement and dimensions of the beam, the free strain accounts for the thickness and Young's moduli of individual layers within the tri-layer actuator. Therefore, free strain is a more representative measure of the electrochemically induced strain in the conducting polymer layer of the actuator. Additionally, we calculated the strain-to-charge ratios (α) using Equation (3-6):

$$\alpha = \frac{\epsilon}{C_V V}. \tag{3-6}$$

The strain-to-charge ratio is related to the volume change produced per charge inserted; the strain is proportional to the charge passed [117].

Resonance Frequency

Mechanical resonance is the tendency of a mechanical system to respond at a greater amplitude when the frequency of oscillation equals the natural/resonance frequency (f_r) of the system. Mathematically, a system is at resonance when the exciting force and system's response are in phase with each other. The f_r of CP tri-layer actuators depends on the mechanical properties and dimension of the device [118]. Equation (3-7) estimates f_r of CP tri-layer actuators:

$$f_r = \frac{1}{2\pi\sqrt{12}} \alpha_n^2 \frac{h_T}{L^2} \sqrt{\frac{EI}{I_T \rho}(1-\zeta^2)}, \tag{3-7}$$

where α_n is a coefficient defined by the n^{th} normal mode of natural frequency and equals 1.87 at the fundamental frequency (first normal mode), 4.694 at the second mode, and 7.855 at the third mode for a free bending cantilever beam [118]. We obtain EI from Equation (3-8) [119]:

$$EI = \frac{W}{12}\left(E_g h_g^3 + E_p\left(h_T^3 - h_g^3\right)\right), \tag{3-8}$$

and the total moment of inertia (I_T) from Equation (3-9):

$$I_T = \frac{W h_T^3}{12}. \tag{3-9}$$

The damping ratio (ζ) for PEDOT:PSS/PVDF/PEDOT:PSS tri-layer actuators was previously decribed by Ebrahimi T. *et al.* [3]. This parameter is primarily influenced by the viscosity of the electrolyte and thickness of the device. We estimated composite density (ρ) in Section 2.4.

According to these equations, f_r is directly proportional to thickness (h) and increases inversely to the square of length (L). Therefore, we predict that short thin beams result in high fundamental resonant frequencies. Maziz *et al.* previously observed these correlations; They observed a resonant peak at 930 Hz designing a CP tri-layer beam with L = 690 μm and h = 12 μm [23]. This is the highest recorded f_r reported in the literature for CP tri-layer actuators.

3.2.3 Results

3.2.3.1 Actuation

Figure 3-2a-f shows the top view optical image of the extent of actuation of a MeOH+EMITFSI treated PEDOT:PSS/PVDF/PEDOT:PSS tri-layer actuator under the influence of a sine wave voltage with an amplitude of 500mV and frequencies of a) 0.1 Hz, b) 1 Hz, c) f_c = 4 Hz, d) 10 Hz, e) f_r = 69 Hz, and f) 100 Hz. Figure 3-2g-l shows the fitted sine wave to the normalized actuation response at each of these frequencies. Deflection follows the shape of the applied voltage.

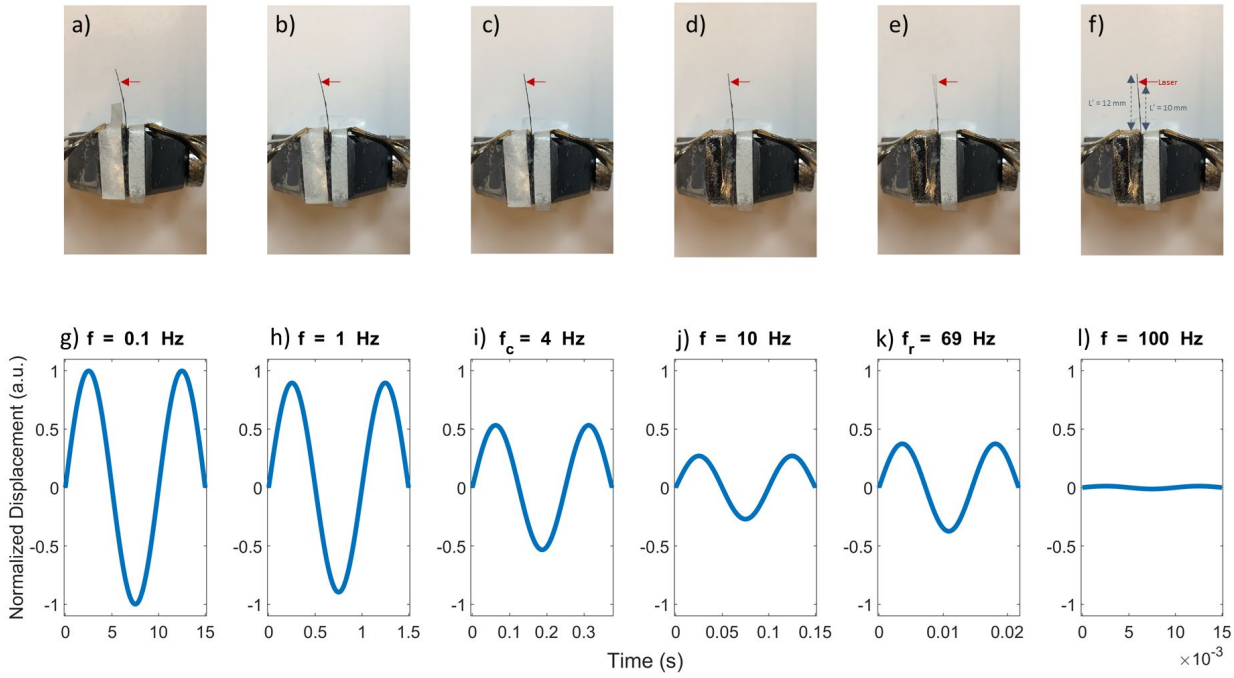

Figure 3-2 a-f) Top view of PEDOT:PSS/PVDF/PEDOT:PSS tri-layer actuators treated with MeOH+EMITFSI. These actuators operate through the application of a sine wave voltage with an amplitude of 500 mV and frequencies of a) 0.1 Hz, b) 1 Hz, c) cut-off frequency = 4 Hz, d) 10 Hz, e) resonance frequency = 69 Hz, and f) 100 Hz. The length and width of the device are (12 ± 0.25) mm and (2 ± 0.25) mm, respectively. The displacement of the device was measured at L' = (10 ± 0.25) mm from the fixed end. g-l) Fitted sine curve to the normalized peak-peak displacement versus time of the actuation response. Peak-peak displacement of the actuator operated at 0.1 Hz and measured at L' was 1999 µm.

The displacement of the actuator decreased as frequency increased. This decrease indicated displacement was driven by time-dependent internal processes; as there was less time for these processes to occur, a smaller proportion of the CP electrodes charged and the devices produced less strain [120]. We observed cut-off frequency (f_c), which occurs when the tri-layer bends to $(1 - 1/e) \approx 0.63$ (Equation (2-7)) of the maximum deflection (D – measured at 0.01 Hz), at 4Hz for these actuators (Figure 3-2i). At ~69 Hz, we observed the first mode of mechanical resonance, which corresponded to an increase in displacement (Figure 3-2k). Above resonance frequency (f_r), displacement decreased at a faster rate, which resulted in small but still measurable deflection at

100 Hz (Figure 3-2l). In subsequent sections, we further discuss experimental parameters, such as applied voltage and beam dimensions, that influence the displacement versus frequency response of these tri-layer actuators. We also explore the impact of polar solvent and IL treatments.

3.2.3.2 Influence of Voltage

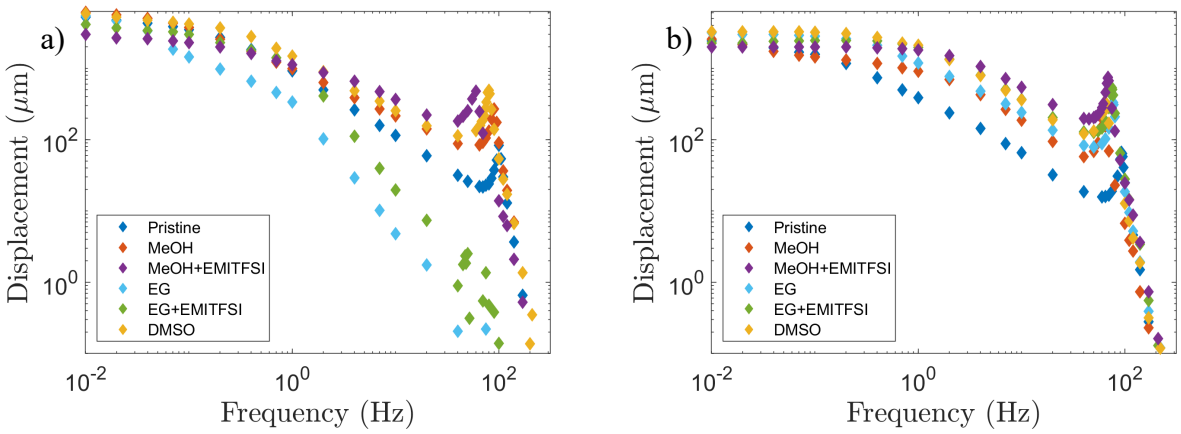

Figure 3-3 Displacement vs. plots for 1cm long beam. a) ± 1V b) ± 0.5V

We initially performed all frequency response experiments by applying a sinusoidal voltage with an amplitude of 1 V, based on previously reported results from Ebrahimi T. *et al.* that PEDOT:PSS/PVDF/PEDOT:PSS tri-layer actuators were stable within this operational window [3]. However, as shown in Figure 3-3a, we observed overoxidation resulting in electrochemical degradation [121]. This was evident from the negative slope exhibited by all samples at $f < f_c$. Additionally, we could not reach the same displacement magnitude in repeat measurements, which indicated a decrease in mechanical performance.

We repeated measurements on new samples for each treatment at a voltage amplitude of 0.5 V, which are shown in Figure 3-3b. For all samples, we observed that maximum peak-to-peak displacement at 0.01 Hz decreased with voltage, as shown in Table 3-2. We expected this result since strain is proportional to voltage, according to Equation (3-6). John *et al.* demonstrated that tri-layer actuators exhibit a linear relationship between maximum displacement and voltage [120].

However, we observed a horizontal slope below f_c, a slower rate of displacement drop-off as f increased above f_c, and larger displacement magnitudes at f_r. These results showed that an amplitude of ± 0.5 V stays within the electrochemical window of the tri-layer actuators and does not degrade the material.

Table 3-2 Maximum peak-peak displacements recorded at 0.01 Hz for each treatment under an applied sinusoidal voltage with amplitudes of 1 V or 0.5 V.

	Voltage	Pristine	MeOH	MeOH+EMITFSI	EG	EG+EMITFSI	DMSO
Maximum peak-peak displacement at 0.01 Hz (um)	**1 V**	5201	6102	2973	5450	4139	5839
	0.5 V	2407	2559	1999	3176	2271	3234

3.2.3.3 Influence of Treatment

Cut-off frequency (f_c) occurs when the tri-layer bends to $(1 - 1/e) \approx 0.63$ of the maximum deflection (D – measured at 0.01 Hz). Pristine samples demonstrated an f_c = 0.1 Hz. We predicted that improving the electrical conductivity of PEDOT:PSS through polar solvent treatments would increase the speed of our tri-layer actuators. As discussed in Section 2.6, we also found that these treatments significantly increased ionic conductivity of the tri-layer actuators. Based on the frequency response results presented in Figure 3-3b, we concluded that ionic conductivity more strongly influenced cut-off frequency of the actuators compared to electrical conductivity. MeOH+EMITFSI and EG+EMITFSI treated samples showed the largest increase in ionic conductivity, which corresponded to the highest f_c values of 4 Hz and 2 Hz, respectively. DMSO post-treatment increased f_c by an order of magnitude to 1 Hz. MeOH and EG treatments did not significantly change f_c, compared to the untreated sample.

Electrical and ionic conductivities appeared to also have an effect on the frequency response at $f > f_c$. Resonance peak-to-peak displacement of the pristine sample was 66.4 μm at 93 Hz. All treated samples demonstrated a less rapid drop-off in displacement as f increased,

compared to the pristine sample. The MeOH+EMITFSI treated samples showed the largest magnitude of peak-to-peak displacement at resonance, with a value of 749.1 μm at 69 Hz. These results demonstrated that we successfully improved the speed of our CP tri-layer actuators, which opens the possibility of high-speed applications, such as vibrotactile feedback displays.

When the actuators had sufficient time to charge, at $f < f_c$, the conductivities of the material did not appear to influence displacement characteristics. We observed that samples treated with pure organic solvent achieved the largest maximum displacement at low f. DMSO treated samples exhibited the largest displacement with a value of 3.24 mm. MeOH and EG achieved displacements of 2.56 mm and 3.18 mm, respectively. Conversely, maximum displacements of MeOH+EMITFSI and EG+EMIFSI decreased compared to the pristine sample with values of 2.00 mm and 2.27 mm, respectively. The untreated sample achieved a maximum displacement of 2.41 mm. These results appear to correlate to the stiffness of the material.

Table 3-3 Summary of measured parameters for PEDOT:PSS/PVDF/PEDOT:PSS tri-layer actuators pristine or treated with MeOH, MeOH+EMITFSI, EG, EG+EMITFSI, or DMSO. Parameters include: volumetric capacitance (C_V), Young's Modulus (E_P), peak-to-peak displacement (D), mechanical cut-of frequency (f_c), resonance frequency (f_r), free strain/Voltage (ϵ/V) and strain-to-charge ratio (α).

Treatment	C_v (F/cm^3)	E_p (MPa)	D (μm) - measured at 500mV & f = 0.01 Hz	Mechanical f_c (Hz)	Mechanical f_r (Hz)	ϵ/V (%/V)	α (mm^3/C)
Pristine	27.4	1680.8	2407	0.1	93	0.35	0.13
MeOH	24.4	2459.9	2559	0.07	63	0.36	0.15
MeOH+EMITFSI	33.1	849.1	1999	4	69	0.34	0.10
EG	55.6	2527.3	3176	0.4	77	0.44	0.08
EG+EMITFSI	35.0	887.9	2271	2	75	0.38	0.11
DMSO	46.5	2161.2	3234	1	64	0.45	0.10

Table 3-3 summarizes the experimental parameters of PEDOT:PSS required to determine ϵ at 0.01 Hz and α – based on Equations (3-5) and (3-6), respectively. Values for f_c and f_r are also tabulated. Based on these results, we concluded that none of PEDOT:PSS post-treatments had a

large impact on α, compared to the untreated sample. We measured an α value of 0.13 mm^3/C for the pristine samples, which agreed with previously reported values by Ebrahimi T. *et al.* [3].

3.2.3.4 Influence of Geometry

In addition to electrochemical and material properties of PEDOT:PSS, dimensions of the cantilever beam also impact the displacement-frequency response. In this section we measured the frequency response of a (5 ± 0.25) mm sample treated with MeOH+EMITFSI. John *et al.* showed that the fundamental resonant frequency is an inverse function of length [118]. According to Equation (3-7), we expected the shorter sample to exhibit a higher f_r. Figure 3-4 shows the displacement versus frequency response of a (5 ± 0.25) mm PEDOT:PSS/PVDF/PEDOT:PSS tri-layer actuator treated with MeOH+EMITFSI compared to the same sample (10 ± 0.25) mm long. Decreasing the length of the beam increased f_r from 69 Hz (at 10 mm) to 292 Hz (at 5 mm).

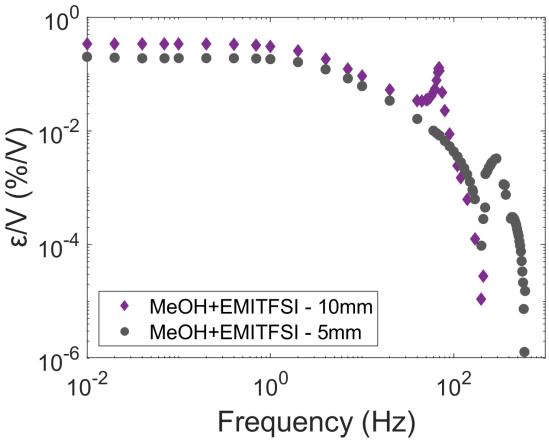

Figure 3-4 strain vs. frequency response for MeOH+EMITFSI treated sample at ± 0.5V for beam length of 10 mm vs. 5mm.

Intuitively, the time required to charge the length of a beam (τ_e) decreases with beam length. Therefore, we expected f_c to increase accordingly. However, for both the 10 mm and 5 mm length beams, f_c = 4 Hz. This suggested that ionic resistance through the thickness of the tri-layer actuator contributes more to overall impedance than electrical resistance along the length of the

beam at low frequencies. However, as f increased, τ_e appeared to play a larger role in limiting the speed and performance of the device. As shown in Figure 3-4, the 5 mm length beam exhibited a lower rate of drop-off in ϵ compared to the 10 mm sample. At 100 Hz (above the 10 mm sample f_r and below the 5 mm sample f_r), the ϵ of each beam were equal. As f continued to increase, the 5 mm sample exhibited higher ϵ.

Table 3-4 Summary of measured parameters for MeOH+EMITFSI treated PEDOT:PSS/PVDF/PEDOT:PSS tri-layer actuators (10 ± 0.25) mm or (5 ± 0.25) mm in length. Free strain/voltage (ϵ/V) and strain-to-charge ratios (α) are also tabulated.

Length	D (μm) - measured at 500mV & f = 0.01 Hz	Mechanical f_c (Hz)	Mechanical f_r (Hz)	ϵ/V (%/V)	α (mm^3/C)
10 mm	1998.9	4	69	0.34	0.10
5 mm	291.1	4	292	0.20	0.06

3.3 Electrochemical Impedance Spectroscopy

Electrochemical Impedance Spectroscopy (EIS) is a technique based on mathematical transforms that result in real values of impedance in temporal space. Impedance is the general oppositional force to electron current that accounts for frequency dependence. It can encompass resistance, capacitance, and inductance. In Bode plots, impedance and phase angle are plotted versus frequency [122]. This analysis gives information on time constants and nature of the impedance across a wide frequency range.

3.3.1 Methods

We performed 2D EIS measurements using the same set-up as described in Section 3.2.1 for actuation-frequency response. We clamped a T-shaped sample with beam dimensions of L = (12 ± 0.25) mm, W = (2 ± 0.25) mm, and contact area = 6 mm^2 tightly between gold electrodes. We applied a sinusoidal voltage with an amplitude of 10 mV and frequency sweep from 10^6 Hz to to 10^{-3} Hz using a Solartron 1287A Potentiostat/Galvanostat (Hampshire, UK), with a Solartron 1260A Frequency Response Analyzer.

3.3.2 Results

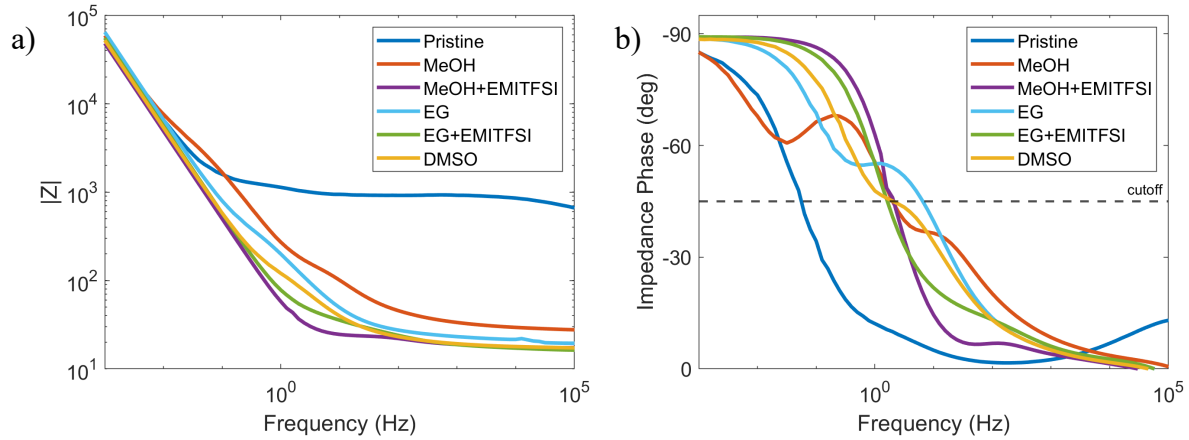

Figure 3-5 Bode a) magnitude and b) phase plots of the impedance for 1cm and ±10mV

For all devices, at high frequencies the phase of impedance was close to zero, as shown in Figure 3-5b. This was indicative of nearly pure resistive behavior. Here, the magnitude of impedance is equal to the sum of ionic resistances, electrical resistance and contact resistance. As predicted from both electrical and ionic conductivity measurements, pristine samples exhibited the largest impedance compared to treated samples at high frequencies. Figure 3-5b shows that impedance phase decreases as frequency of the applied voltage decreases, which indicates charging/discharging of the PEDOT:PSS electrodes, as they become more capacitive.

A phase angle of -90° is the maximum possible phase shift between voltage and current, and indicates the device is ideally capacitive. However, none of the samples in this study fully reach -90°, which suggested that there is electron flow through the separator layer. This was likely a result of leakage between the CP electrodes, due to an electrical short-circuit. Pristine and MeOH treated samples showed the lowest absolute phase angle at low frequencies. Conversely, the MeOH+EMITFSI and EG+EMITFSI treated samples exhibited the most capacitive behavior with phase angles of -88.9° and -89.2°, respectively at 0.001 Hz.

The impedance of a resistor is independent of frequency and only contains the real component of impedance (Z'). Conversely, impedance of a capacitor is inversely proportional to frequency and only has the imaginary (Z'') component. Bode plots with slopes near -1 are characteristic for capacitive materials and slopes near 0 are indicative of resistive behavior [123]. The slopes of the untreated sample and samples treated with pure polar solvents demonstrated |slopes| < |-1|, which indicated that they did not behave as ideal capacitors at low frequencies. However, the MeOH+EMITFSI and EG+EMITFSI treated samples had slopes equal to -0.99 and -0.98, respectively, which showed quantitatively that they are near ideal capacitors. Table 3-5 summarizes these results.

The tri-layer exhibits half capacitive and half resistive behavior when the impedance phase equals -45° [100]. This occurs at the cut-off frequency of the device, which correlates to the minimum time required for fully charging or discharging the capacitor. This time constant represents the transition from resistive to capacitive behavior for an electrochemical capacitor [123]. Table 3-5 summarizes these cut-off frequencies determined from the Bode phase plots for the untreated and treated samples.

Table 3-5 Summary of cut-off frequencies (at phase = -45°) and slope of Bode magnitude plot for pristine and treated PEDOT:PSS/PVDF/PEDOT:PSS samples.

	Pristine	MeOH	MeOH+EMITFSI	EG	EG+EMITFSI	DMSO
f_c	0.05	2.0	2.0	6.3	1.6	2.0
Bode Slope	-0.72	-0.69	-0.99	-0.86	-0.98	-0.94

The phase Bode plots for pristine and polar solvent treated samples appeared to consist of multiple time constants corresponding to several rise and plateau sections through the frequency sweep. Dobashi *et al.* proposed that this behavior may be explained by a gradient in the distribution of PEDOT into the PVDF membrane, which results in non-uniform electronic and ionic resistances per unit length and capacitance per unit length across the thickness of the device [100].

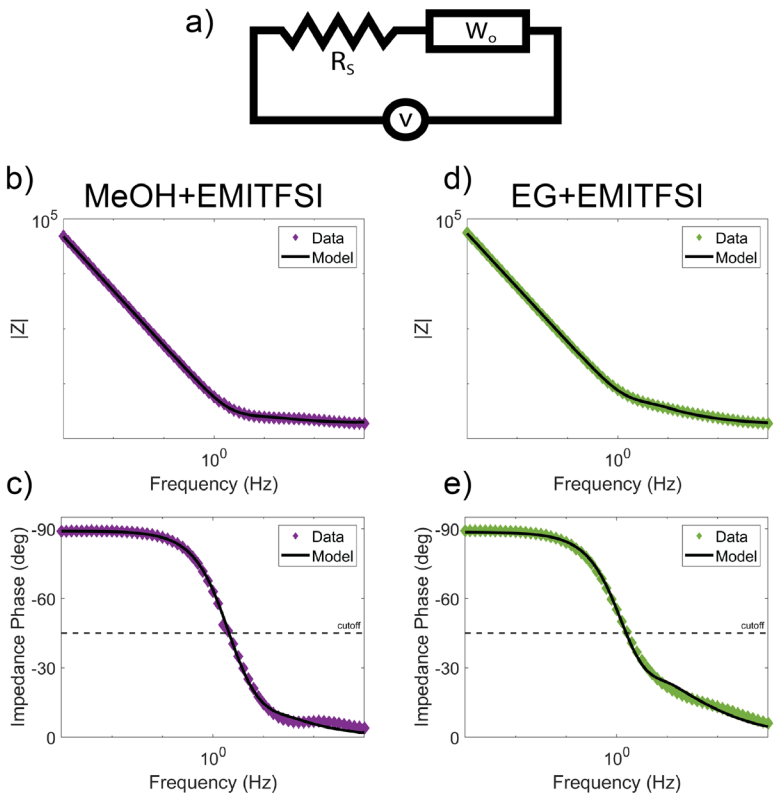

Figure 3-6 a) equivalent circuit of Warburg open (W_o) element in series with a resistive element (R_s). Model results for b) Bode plot of |Z| versus frequency of MeOH+EMITFSI treated samples, c) phase Bode plot of MeOH+EMITFSI treated samples, d) Bode plot of |Z| versus frequency of EG+EMITFSI treated samples, c) phase Bode plot of EG+EMITFSI treated samples.

For samples that exhibited close to ideal capacitive behavior (MeOH+EMITFSI and EG+EMITFSI), we used the program ZView to model an equivalent circuit that consisted of a resistor (R_s) in series with a Warburg open circuit element (W_o) – shown in Figure 3-6a. Warburg impedance represents 1D diffusion behavior. In electrochemical systems such as supercapacitors or batteries, the process of ion diffusion within a porous electrode in the system also gives rise to a characteristic Warburg element. In an open system, the response tends towards capacitive-like behavior as *f* decreases. Equation (3-10) describes the W_o element:

$$W_o = Z_0(j\omega\tau)^{-\alpha}\coth(j\omega\tau)^{\alpha}\,, \tag{3-10}$$

where Z_0 is the real component of W_o, τ is the time constant of the system and is related to the effective diffusion thickness (L) and effective diffusion coefficient (D) of the ions by Equation (3-11):

$$\tau = \frac{L^2}{D}. \tag{3-11}$$

The coefficient α equals ½ in an ideal Warburg system. Table 3-6 summarizes the modelled values of R_s, Z_0, τ, and α for both MeOH+EMITFSI and EG+EMITFSI treated samples.

In both models, $\propto \approx 0.5$; the MeOH+EMITFSI model had a value of 0.47 and the EG+EMITFSI model value was 0.49. This showed that the systems exhibited nearly ideal Warburg characteristics and were diffusion controlled. The τ values for MeOH+EMITFSI and EG+EMITFSI treated samples were 0.050s and 0.19s, respectively. These values correspond to f_c values of 3 Hz and 0.8 Hz, which fall within the range of f_c values we calculated from the actuation-frequency response data for both treatments.

We used this model to calculated capacitance (C) from the Warburg RC time constant (τ) and resistance (Z_0). These values were 3.2 mF and 3.0 mF for MeOH+EMITFSI and EG+EMITFSI treated samples, respectively. We also compared the R_s and Z_0 values obtained in this model to the R_i values we measured in Section 2.6.2 (Ionic Conductivity). R_i for the MeOH+EMITFSI sample had a value of 17.6 **Ω**, which fell between the values for R_s and Z_0, shown in Table 3-6. This suggested that, due to the low ionic resistance of MeOH+EMITFSI treated PEDOT:PSS, the time required for diffusion of ions through both the separator and conducting polymer layers contributed significantly to the RC time constant. Conversely, we measured a value of R_i equal to 61.2 **Ω** for the EG+EMITFSI treated samples. R_s and Z_0 values for this sample were 17.9 **Ω** and 72.2 **Ω**,

respectively. These values suggested that ionic resistance through the conducting polymer layers dominated the RC time constant in these samples.

Figure 3-6b-c show the Bode plots for the MeOH+EMITFSI model and Figure 3-6d-e show the Bode plots for the EG+EMITFSI model; all these figures also include the experimental results for comparison. The impedance response for pristine and pure polar solvent treated samples show more complex behavior. More analysis is needed to understand these systems and develop well-fitting equivalent circuit models.

Table 3-6 Summary of EIS equivalent circuit modelling results of MeOH+EMITFSI and EG+EMITFSI samples for the following elements: solution resistance (R_s), Warburg open impedance (Z_0), Warburg open time constant (τ) and Warburg open phase (α). From these results, capacitance (C) and volumetric capacitance (C_v) were calculated based on the specific cantilever beam geometry. Ionic resistance (R_i), based on the measured ionic conductivity and specific cantilever beam geometry is also presented here.

MeOH+EMITFSI			EG+EMITFSI		
Element	**Value**	**error**	**Element**	**Value**	**error**
Rs (Ω)	18.0	0.2	**Rs (Ω)**	17.9	0.1
Z_0 (Ω)	16.9	2.6	**Z_0 (Ω)**	72.2	1.8
τ (s)	0.050	0.010	**τ (s)**	0.19	0.01
α	0.47	0.02	**α**	0.49	0.001
C (mF)	3.2	0.01	**C (mF)**	3.0	0.03
C_v (F/cm^3)	18.8	-	**C_v (F/cm^3)**	17.6	-
R_i (Ω)	17.6	-	**R_i (Ω)**	61.2	-

Warburg impedance models have some limitations; we assumed 1) the CP electrodes were a single lumped element with a real and imaginary component, and 2) charge was evenly distributed through the structure, which means we could not derive conclusions about the actual location of the charge within the porous structure. A transmission line model is a more complex alternative that is capable of assigning local circuit elements and configurations to more accurately describe the electrochemical behavior of the system. Several researchers have developed transmission line models to describe CP tri-layer actuators [3, 26, 30, 100, 124, 125].

3.4 Application of Actuatool Model

Ebrahimi T, *et al.* developed the graphical user interface (GUI) ActuaTool – an analytical model to dynamically predict the electro-chemo-mechanically behavior of the actuators based on input geometry and material properties of the separator and CP layers [3]. Deformation, speed and blocking force are all metrics we need to optimize to our intended application. Models such as Actuatool are helpful tools for iteratively optimizing device parameters. Blocking force, in particular, is a challenging metric to quantify experimentally. In this section, we discuss the application of Actuatool to estimate how the chemical post-treatments effect blocking force (supplemental results available in Appendix D).

3.4.1 Blocking Force

Blocking force is defined as the minimum force needed to return the actuator to its neutral axis and is an indication of the maximum force possible. Equation (3-12) approximates the relationship between ϵ and F_B as a function of frequency (f):

$$\frac{F_B(f)}{V(f)} \approx \epsilon(f)\left[\frac{3W}{2L}E_p h_p\left(h_p + h_g\right)\right]. \tag{3-12}$$

In this relationship for dynamic actuation, we assume charge transfer occurs evenly though the entire volume of the CP layers. We also assume that the entire beam returns to its neutral axis when we apply F_B to the tip. However, since the bending moments vary along the length of the beam, some buckling occurs. These assumptions result in a slightly larger F_B predicted by the model compared to what the actuators can generate.

3.4.1.1 Methods

We collected F_B measurements experimentally using a micro-force sensor (Femtotoolss; FT-S270 and FT-S540). We clamped a 20 layer pristine tri-layer actuator beam with the same dimensions as described in Section 3.2.3.1 on actuation (L = 10 mm, W = 2 mm, h_p = 4.74 μm, and h_g = 125 μm). The tip of the force sensor was brought into contact with the tip of the actuator, such that no force was applied. We applied a sinusoidal voltage with an amplitude of 1 V at f = 0.01 to 100 Hz sequentially and recorded the maximum force. We then compared these experimental results to the modelled F_B – frequency response (Note: this experimental data was collected by Dr. Saeedeh Ebrahimi Takalloo during her PhD).

Next, we predicted how treatment with polar solvents and polar solvents mixed with EMITFSI impacted F_B frequency response of our CP tri-layer actuators. We applied the Actuatool model based on our measured electro-chemo-mechanical parameters.

3.4.1.2 Results

Figure 3-7 shows the F_B frequency response determined experimentally and using the Actuatool model. At $f < f_c$, the model accurately estimated the F_B generated by the tri-layer actuators. As we predicted, the modelled results report slightly larger F_B at $f > f_c$. These results show that we can reliably use Equation (3-12) to estimate F_B. Measuring F_B experimentally presents multiple challenges that makes obtaining accurate results difficult and time consuming. Therefore, we chose not to continue with experimental analysis for treated samples, after showing that our model reliably estimates blocking force, especially at low f.

We observed that the samples with the largest E_p generate the largest F_b. Since F_B is proportional to E_p, according to Equation (3-12), we expected to see this trend. At low f, samples treated with pure polar solvents exhibited the largest F_B values. MeOH+EMITSI and

EG+EMITFSI treated samples generated approximately half the force of untreated samples, due to reduced E_P values. However, these samples maintained maximum force output up to ~1 Hz, which was the highest f_c of all the samples modelled. These results suggest that pure polar solvent treated samples are better suited to relatively high force and low speed applications, whereas those treated with a combination of polar solvent and IL may work for low force and higher speed applications.

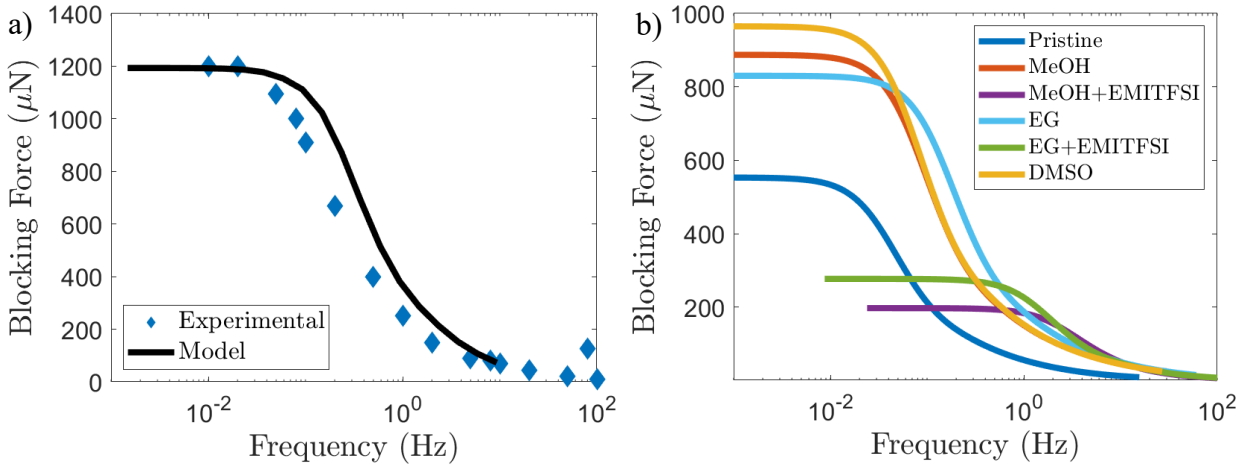

Figure 3-7 a) Comparison of blocking force (F_B) measured experimentally and predicted by the Actuatool model. b) Modelled F_B frequency response for PEDOT:PSS/PVDF/PEDOT:PSS tri-layer actuators pristine or following treatment with MeOH, MeOH+EMITFSI, EG, EG+EMITFSI, or DMSO.

These results support previous work that shows altering properties of the CP tri-layer actuators to enhance performance in one parameter often comes at the cost of performance in another aspect [38, 44]. Our DMSO treated samples exhibited a maximum F_B of 1.9 μN/V at low frequency. Previous work by Temmer *et al.* designed PEDOT/PPy composite tri-layer actuators that achieved a maximum F_B of ~3mN/V. They showed that adding a PPy layer to PEDOT-based actuators increased the maximum strain and force but decreased the speed. Their pure PEDOT tri-layer actuators exhibited a much lower F_B of ~ 0.45 mN at low *f*; however, they generated larger forces and displacements than the composite tri-layers above ~1 Hz [38]. The trade-offs this

research showed between designing for high strain and force compared to speed by incorporating PPy are similar to the trends we see between the pure polar solvent and polar solvent + IL treatments we investigated in this work.

3.5 Comparison of Cut-off Frequencies

Table 3-7 summarizes all the f_c values we have discussed so far in this thesis. We calculated the electrical (f_{ce}), ionic – polymer (f_{cip}) , and ionic separator (f_{cig}) values based on the time constant Equations (1-1)-(1-3). These calculations show that impedance of ion diffusion through the separator has the least impact on limiting actuation speed. The f_{cip} arising from ion diffusion through the CP layers has the smallest value and appears to initially cause the drop in mechanical performance at low *f*. Therefore, CP ionic resistance likely contributes most to the overall impedance of the system. However, results for the MeOH+EMITFSI treated samples show an exception to this general trend. In this case, $f_{ce} < f_{cip}$, which suggests that the rate of electrical charging plays a larger role in impeding mechanical performance, due to the higher ionic conductivity of these samples.

Table 3-7 Summary of all calculated, measured, and predicted cut-off frequencies

	Cut-Off Frequency						
Treatment	**Electrical**	**Ionic - Polymer**	**Ionic - Separator**	**CV Rise Time**	**Mechanical Frequency Response**	**EIS**	**Actuatool**
Pristine	0.13	0.02	11.19	0.55	0.10	0.05	0.05
MeOH	2.68	0.03	12.56	1.02	0.07	2.0	0.11
MeOH+EMITFSI	2.30	3.31	9.26	4.08	4.00	2.0	3.63
EG	1.30	0.06	5.51	0.80	0.40	6.3	0.21
EG+EMITFSI	2.28	0.91	8.76	1.53	2.00	1.6	2.00
DMSO	1.92	0.03	6.59	0.77	1.00	2.0	0.10

The f_c values we measured based on the CV rise time and mechanical frequency response appear to most closely align with f_{cip}. Our results suggest σ_e is not the main contributing factor to the overall f_c, at least in the geometry and for the materials we used. Additionally, this further

supports our observation that ionic resistance due to diffusion through the CP electrodes is the largest contributor to overall f_c and drop in mechanical performance. If the tri-layers were significantly longer (about 2.5 times longer in the pristine case, and 7 times longer for the treated material), or less conductive, we expect σ_e would dominate the frequency response.

Finally, we applied our definition of mechanical f_c to our modelled Actuatool results. These results mostly agree with the measured values, with the exception of the DMSO treated samples that have a modelled f_c value 10 times smaller than the corresponding measured value. Figure 3-8 illustrates the range of f_c values calculated, measured, or modelled for each treatment.

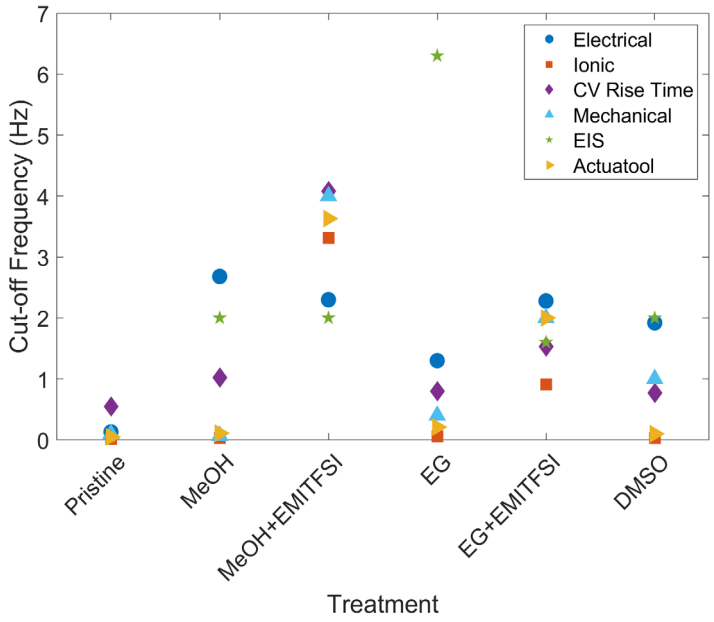

Figure 3-8 Comparison of calculated, measured, and modelled f_c values.

3.6 Conclusion

In this section we analyzed the mechanical performance of PEDOT:PSS/PVDF/PEDOT:PSS tri-layer actuators. We first described how polar solvent affect Young's Modulus. Next, we showed the actuation frequency response of samples treated with MeOH, MeOH+EMITFSI, EG, EG+EMITFSI, or DMSO compared to untreated samples. We also applied a transmission line model to predict force generation versus frequency of our samples. Our results showed that despite improving the conductivity of PEDOT:PSS, we did not significantly increase the cut-off frequency of the device. However, treated samples demonstrated larger strain at frequencies > 1 Hz and higher displacement values at resonant frequency. Therefore, the contribution of this work may be relevant for applications that require high frequencies, but not necessarily large displacements. For example, tactile feedback interfaces that reproduce sensations have applications in myoelectric prosthetics, robotic surgical tools, and braille cells for the visually impaired. Vibrotactile haptic displays operate best at high frequencies between 100-300 Hz, but only need small displacements < 100 nm to overcome threshold of human perception [126, 127]. In Chapter 4, we investigate the feasibility of these CP tri-layer actuators in vibrotactile displays.

Chapter 4: Feasibility of Vibrotactile Feedback Displays

Tactile displays that create vibration are the most widespread and best understood form of haptic feedback [127]. The basic mechanism for vibration feedback of surface haptic devices involves a vibration wave propagating into a screen to reach the finger or hand. This approach is sufficient for simple vibrotactile effects, such as alerting a user to incoming notifications [128]. More sophisticated actuators can also create a range of sensations that vary in amplitude, frequency, and waveform. Important engineering considerations generally include size, shape, cost, robustness, material properties, speed of response, input requirements, power consumption, noise and heat generation, potential interference with other system components [127].

In this Chapter we provide a brief background on the physiology of touch in humans. We also explore advantages and limitations of current and developing vibrotactile haptic technologies. This background provides a framework for how we can design our conducting polymer tri-layer actuators into viable tactors that advance this space. We developed initial conducting polymer tactor prototypes and characterized their displacement and electrochemical impedance. In addition, we modelled blocking force and used these values to predict the skin deflections our actuators could generate. Based on these results, we discuss the efficacy of our actuators as vibrotactile displays and the future work needed to design viable tactors that we can incorporate into commercial haptic technologies.

4.1 Background

4.1.1 Physiology of Perception

Human sense of touch is highly developed and essential for nearly all facets of daily life. The somatosensory system allows users to experience and interpret tactile stimuli (mechanical, thermal, electrical and chemical stimulation) – and kinaesthetic stimuli (physical force/torque, body orientation, lib alignment, and joint position) in the physical world [129, 130]. In electronics design, haptic feedback is the use of touch to communicate information to the device user. This tactile sense enables humans to perceive object properties through skin contact. For example, smartphones deliver short vibrations as notification alerts or to confirm a virtual key has been pressed. More sophisticated tactile rendering can display natural, intuitive and rich information, with relatively low complexity and cost [127].

Cutaneous sensory end organs, called mechanoreceptors, are responsible for detecting and distinguishing mechanical stimuli, which allows us to sense pressure, texture, and vibration [131]. Mechanoreceptors reside in the dermis layer of the skin (typically 50-100 μm beneath the surface) and consist of one or more sensory cells, the corresponding afferent nerve fibers, and the connection to the central nervous system (CNS) [126]. The typical thresholds for perception are stimuli on the order of 10-100 mN and 10-100 μm [130]. Perception of vibrotactile stimuli depends on actuation frequency, amplitude, waveform, shape and material of the indenter, body site, duration, contact area, gender, and age [128, 129].

4.1.1.1 The Four Channel Model

Glabrous skin (smooth hairless skin found on the hands and feet) contains four types of mechanoreceptors, shown in Figure 4-1, which differ in adaptation (slow or fast) and size of the receptive field (small/I or large/II), to respond to different stimuli. Adaptation refers to the nature of response to a stimulus. Slow adapting receptors respond to steady skin indentation with a sustained afferent neuron discharge. Fast adapting receptors stop firing as soon as the indentation is static [7]. The receptive field refers to the area on the skin on which an external mechanical stimulus will evoke a nervous impulse on a single nerve fiber [7]. The size of the receptive field depends on the number of sensory cells connected to this nerve fiber. Each afferent unit responds to a mechanical stimulus, only if it is applied over a certain sized area of the skin. A smaller receptive field results in higher spatial sensitivity [126]. Table 4-1 summarizes properties of the four cutaneous mechanoreceptor types. These physiological characteristics of skin provide important parameters for designing haptic technologies.

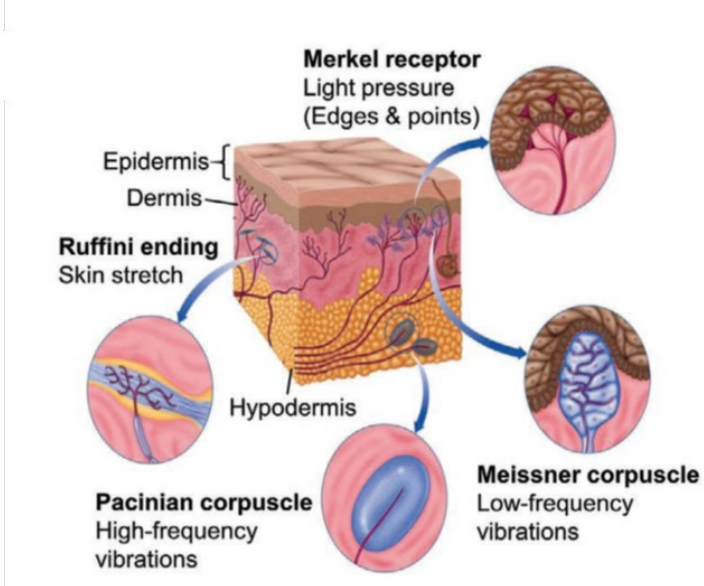

Figure 4-1 Schematic of the four mechanoreceptors found in glabrous skin (Information obtained from © 2013, Cengage Learning)

Table 4-1 Summary of cutaneous mechanoreceptor systems. [a]SA channels tend to maintain their response level for a sustained stimulus and are therefore responsible for spatial properties. [b]FA channels stop responding shortly after the stimulus is applied [7, 127]).

Receptor	Merkel Cell	Meissner Corpuscle	Ruffini Ending	Pacinian Corpuscle
Receptive Field	Type I (small)		Type II (large)	
Adaptation	slow adapting (SA)[a]	fast adapting (RA)[b]	slow adapting (SA)	fast adapting (RA)
Location	tip of epidermal sweat ridges	dermal papillae (close to skin surface)	dermis	dermis (deep tissue)
Axon diameter (μm)	7-11	6-12	6-12	6-12
Best stimulus	edge or point	lateral motion	skin stretch	vibration
Frequency Range	0-100	1-300	-	5-1000
Ideal Frequency	5	50	-	200
Threshold for rapid indentation or vibration (μm)	8	2	40	0.01

The two types of fast-adapting mechano-receptors that detect vibration are Pacinian Corpuscles (PC) and Meissner Corpuscles (MC). These organs are designed to interpret information about the dynamic qualities of mechanical stimuli, such as texture and vibration.

Pacinian corpuscles (FA-II)

PC receptors are large encapsulated endings located in the subcutaneous tissue. They exhibit the largest receptive fields and sensitivity bandwidth. PC's respond to mechanical stimuli in a wide frequency range (10-1000 Hz) but are most responsive to stimulus between 150-300 Hz. The spatial field of PC's is relatively large, which results in low spatial acuity. These channels are also capable of temporal and spatial summation. This means that a stimulus is perceived as stronger over time or for larger contact area [128, 131, 132]. This spatial summation means that the size of skin contact area is one of the most important variables we need to optimize to exceed perception thresholds for frequencies around 200-Hz [133].

Meissner Corpuscles (FA-I)

These mechanoreceptors are sensitive to stimuli acting tangential to the skin surface, which makes them important for sensory control of grip and detection of slip. They are also relevant for detecting vibrations. In contrast to PCs, MC's are activated at relatively low frequencies (3-100 Hz). These receptors have smaller receptive fields than PC's and better spatial resolution. Detection thresholds are independent of vibration frequency and MC's do not experience spatial or temporal summation. These types of mechanoreceptors are most dense on the glabrous skin of the fingertips, where touch is easier to localize [133, 134].

4.1.1.2 Kinaesthetic Receptors

Kinesthesia is the inherent sense of movement of a limb and plays a critical role in coordinating dexterous upper limb (UL) motion. There are also two primary types of receptors for kinaesthetic perception. Neuromuscular spindles consist of muscle fibers wound around nerve fibers parallel to skeletal muscle to measure strain. These afferent sensory receptors are responsible for detecting muscle stretch and providing proprioception. Golgi tendon organs are embedded in tendons and are mechanically in series to skeletal muscle; they are used to control the force muscles exert, detect maximum muscle tension, and provide feedback on joint angles [133].

Schofield, *et al.* demonstrated that when vibrations at frequencies between 70-110 Hz and amplitudes between 0.1-0.5 mm are applied over musculotendinous regions of a limb, it induces a kinesthetic illusion [135]. These vibrations activate muscle spindles, which gives subjects the illusion that their limb is moving in space, even though it physically remains stationary. Vibrotactile displays that stimulate the kinesthetic illusion have shown promise in applications such as providing a proprioceptive sensory feedback loop in myoelectric prosthetic limbs [136, 137].

4.1.1.3 Absolute Threshold

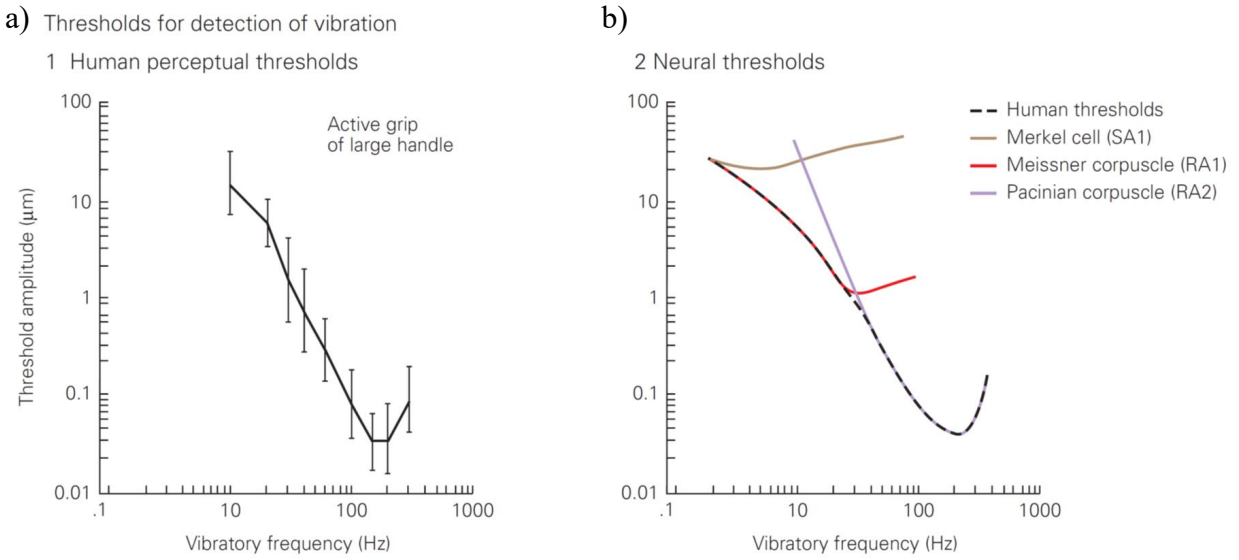

Figure 4-2 a) Psychophysical thresholds for detection of vibration as a function of stimulation frequency. Humans can detect vibrations as small as 10 nm at ~200 Hz (Information obtained from, © 1999, The American Physiological Society [1]). b) The neural threshold for detection of vibration is defined as the lowest stimulus intensity that evokes a single action potential per cycle of sinusoidal stimulus. Each mechanoreceptor is most sensitive within a specific range of frequencies. Human thresholds for vibration align with the most sensitive receptor at each frequency range (Information obtained from, © 2021 McGraw Hill [2, 7]).

Psychophysics researchers most commonly represent sensitivity to physical stimuli by the parameter 'absolute (detection) threshold'. This metric describes the minimum stimulus intensity required for a person to feel [2]. For vibrotactile feedback, the frequency of vibration largely determines the absolute thresholds for a specific force and displacement. This is due to the frequency-dependent nature of the fast acting mechanoreceptor channels. The channel with the lowest threshold at a given frequency determines the absolute threshold, as shown in Figure 4-2b. However, strong enough stimuli excite multiple mechanoreceptor types and, in this case, all activated channels contribute to perception [127, 133]. For example, MC channels typically dominate at frequencies from 1 Hz to 100 Hz. Their detection threshold decreases from approximately 30 μm to 1 μm in this range. As frequency increased above 100 Hz, PC channels dominate, according to the U-shaped threshold curve of skin displacement amplitude versus

frequency, shown in Figure 4-2a [1]. From this graph, the minimum absolute displacement threshold is between 150 to 300 Hz and as small as 0.1 μm. Figure 4-2b illustrates how human perception thresholds to vibration correspond to the most sensitive mechanoreceptor at a given frequency [7, 138].

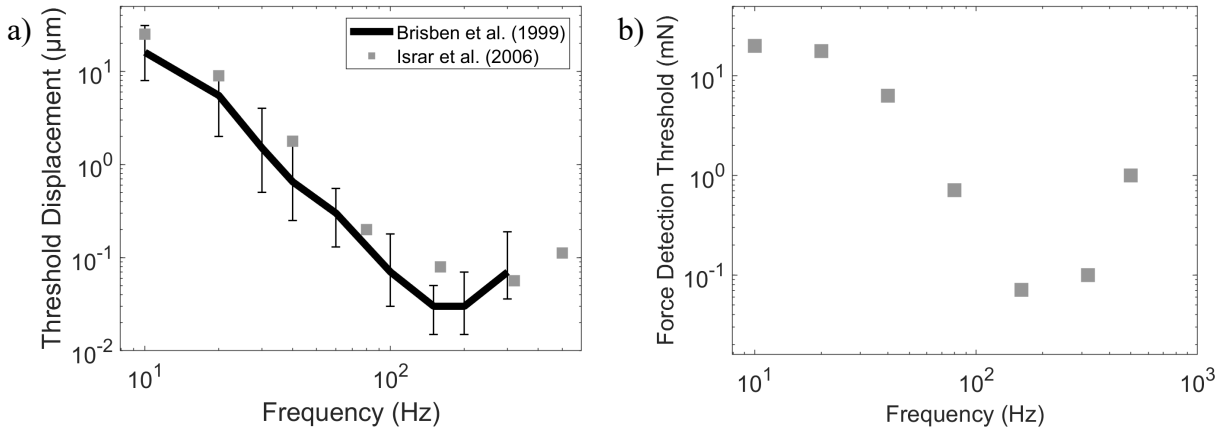

Figure 4-3 a) comparison of frequency dependent displacement thresholds reported by Brisben *et al.* and Israr *et al.* (Adapted from [1, 2]). b) Measured force detection threshold (Adapted from [2]).

Israr *et al.* reported displacement and force detection thresholds for sinusoidal waveforms with frequencies between 10-500 Hz on the fingertip [2]. To our knowledge, this was the first study that measured the perception threshold of applied force. Figure 4-3a compares the displacement threshold results reported by Israr *et al.* to those reported by Brisben *et al.* seven years earlier. The shapes of these threshold curves follow a similar U-shaped trend, with minimum detection thresholds occurring between 150 Hz and 300 Hz. Brisben *et al.* found slightly lower detection thresholds for vibrations transmitted through a hand-held tool. These discrepancies suggest that confounding variables in the experimental set-up, such as contact area, contact force, rigidity of surroundings, skin temperature and water content, affect detection threshold levels.

The shape of the force detection threshold, shown in Figure 4-3b, also follows a U-shaped curve, with a minimum occurring at approximately 160Hz and 70 μN. The force curve exhibits a

lower slope at low frequencies and higher slope at high frequencies, compared to the position threshold curves. This relationship likely results from the mechanical impedance of the skin. This study shows that skin exhibits mass, damper, and spring components [2]. The low slope at frequencies < 40 Hz indicates a dominant viscous element. As the slope increases from 40 to 80 Hz, the stiffness component plays a larger role in the mechanical behavior. The inertial component dominates at frequencies > 320 Hz, as shown by the rising slope of the curve. These trends are characteristic of a viscoelastic material, which suggests that skin experiences frequency dependent stiffness [139]. In Section 4.3.4, we use a viscoelastic model to predict the extent of skin displacement our actuators achieve, based on the frequency dependent blocking force.

Absolute threshold gives margins for sensor and actuator noise and defines the lower limit for communication applications. The subjective perception of vibrotactile stimulation results from a combination of the sum of all tactile and kinaesthetic mechanoreceptors, which has an important role in haptics design. More specifically, 3 Hz is perceived as slow kinesthetic motion, 10-70 Hz feels like rough motion or fluttering, and 100-300 Hz feels like smooth vibration [127]. The subjective quality of vibration can be further modulated by stimulus amplitude and spatial configuration. For example, the fingertip has a spatial resolution between 1-2 mm^2; however, due to size limitations of existing commercially available technologies, current haptic designs do not take advantage of this fine human perception [128]. Artificial muscle technologies in development have the potential to overcome these challenges.

4.1.2 Existing Vibrotactile Actuator Analysis

In this section we outline existing high-speed vibrotactile actuators and describe the advantages and disadvantages of these technologies.

4.1.2.1 Linear Electromagnetic Actuators

Electromagnetism is the physical phenomenon most commonly used to create vibrotactile stimuli. There are a number of motor configurations. In these, an electrically conductive wire (i.e. copper) is covered with an electrically insulating material and wrapped into a continuous coil. When an electrical current is passed through the wire, it generates a steady magnetic field that is strongest inside the wire. A force is generated between the wires in the coil and permanent magnets, other wires that carry currents, or soft magnetic materials. By alternating the applied currents, a vibration is generated. The main challenge with electromagnetic devices is that achieving sufficient forces and displacements typically demands complex designs, bulky rigid components, and poor power efficiencies [126].

Solenoid motor:

A solenoid motor consists of a movable ferromagnetic material (i.e. steel) attached to a spring and enclosed inside a conductive coil. These types of linear motors come in a wide range of sizes and are commonly used in industry applications. The smallest commercial versions have dimensions on the order of 10-mm. The electromagnetic force that actuates a solenoid is strongly dependent on the position the movable element within the magnetic field. Therefore, altering device orientation or mechanical properties of the surface the tactor is contacting often leads to inconsistent vibrotactile sensations. Solenoids also generate heat, which makes them hazardous to use in contact with skin for long periods of time [127].

Voice coil:

A coil that encloses a movable permanent magnet is typically referred to as a voice coil. These devices are similar to speakers used in audio systems, which create broad-frequency air pressure variations that we perceive as sound [128]. When the coil is energized, it attracts or repels the magnet, depending on the physical orientation and direction of current. Applying an alternating current to the coil creates a magnetic field that similarly varies over time, which produces tactile vibrations. These devices are typically sized on the order of tens of millimeters, are usually suitable for low-to-mid range actuation frequencies with respect to human tactile perception, have relatively low voltage requirements (~5 V), and produce a wide range of waveforms with fast response times (1-3000 Hz) [127, 140]. To ensure purely linear actuation, many devices have built in bushing. However, this generates static friction, which can make small vibrations difficult to feel and somewhat distort larger vibrations. Linear ball bearings tend to have lower static friction but generate parasitic lateral vibrations that are perceptible by the user. Vibrotactile sensations generated by voice coils are generally more consistent than those produced by solenoid motors.

Linear resonant actuator (LRA):

A linear resonant actuator is a special type of very small voice coil. These devices are commercially available in thicknesses between 1-3 mm and come in a wide range of geometries. Rather than directly transferring the force produced by the voice coil to the skin, the device optimizes power consumption by pushing against a spring at the spring's resonant frequency. This enables the device to generate higher displacements and forces more efficiently. However, operating LRA's outside of resonant frequencies (typically ±2-Hz) generally does not generate forces perceptible by human skin. This category of vibrotactile actuator is found commercially in

very small mobile devices. Video game controllers also make use of LRAs to provide trackpads with haptic feedback [127, 128].

4.1.2.2 Rotary Electromagnetic Actuators

Eccentric rotating mass (ERM) motors:

Rotary electromagnetic actuators are the most common mode of vibration for haptic surface technologies and are ubiquitous in older mobile electronic devices and gaming controllers [126, 128]. These direct current (DC) motors are designed to rotate continuously when a constant current is applied. An off-centre mass is fixed to the output shaft so that its rotation exerts large uneven centripetal forces on the body of the motor. This eccentric rotating mass (ERM) produces side-to-side osculation of entire device, similar to how spinning clothes in a laundry machine produce vibrations. This is the reason why older mobile phone models tend to spin on a hard surface as they vibrate. ERM actuators can generate relatively large vibrations and be made in a diverse range of sizes and shapes (order of 10 mm). However, this design inherently couples frequency and amplitude of the resulting vibrations to the motor's rotational speed. This restricts the diversity of possible vibration waveforms. Additionally, internal static friction prevents such motors from rotating under very small applied voltages, and they have a time delay for spin up [127, 128, 141].

Piezoelectric actuator:

Piezoelectric actuators are devices, typically fabricated from ceramics, that produce a small displacement with high force capabilities, in response to a high voltage. As shown in Figure 4-4, the dipoles of the piezoelectric material align under the influence of an electric field, which causes the structure to expand. This technology offers an attractive alternative to electromagnetic actuators in haptic interfaces because it is compact, has a high force-to-volume ratio, and can

operate without gears. Additionally, the ability to build ceramic medical devices with non-magnetic motors allows for compatibility with magnetic resonance imaging (MRI) environments. However, piezoelectric actuators typically require high input voltages (50-200 V) and are brittle and weak to external shock [128, 142].

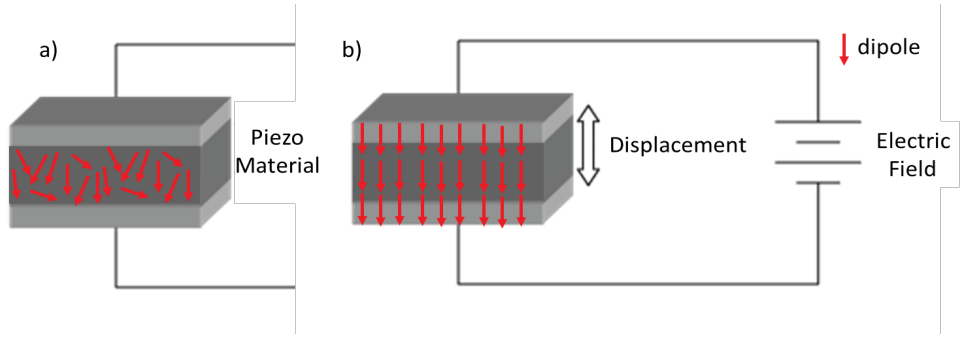

Figure 4-4 Piezoelectric material a) at rest b) under an applied electric field.

4.1.2.3 Other Emerging Vibrotactile Technology

Emerging vibrotactile technologies seek to transform electrical energy directly into mechanical vibrations without additional moving parts, to avoid the bulk and complexities of electromagnetic actuators. Electroactive polymers (EAPs) are materials that undergo dimensional changes in response to an applied electric field. "Artificial Muscle" fabricated from EAPs has the ability to mimic the behavior of mammalian muscles.

Pneumatic Actuators

Soft pneumatic actuators operate by transferring air from a source to a deformable bladder. A thin elastomer membrane encloses circular reservoir that inflates/deflates in response to pressure changes, like a balloon. Figure 4-5 shows an example of a pneumonic vibrotacile actuator developed by Huraoto *et al.* [5]. The active area of the tactor is ~1.5 cm in diameter and inflates to a thickness of ~2 mm under 50 kPa. Pneumatic actuation is appropriate for applications where there are geometric restrictions or for sensitive regions of the body where rigid bulky components

cause irritation and discomfort. The need for a high-pressure air source and regulatory system limits the vibratory action at high frequencies and portability of this technology [5].

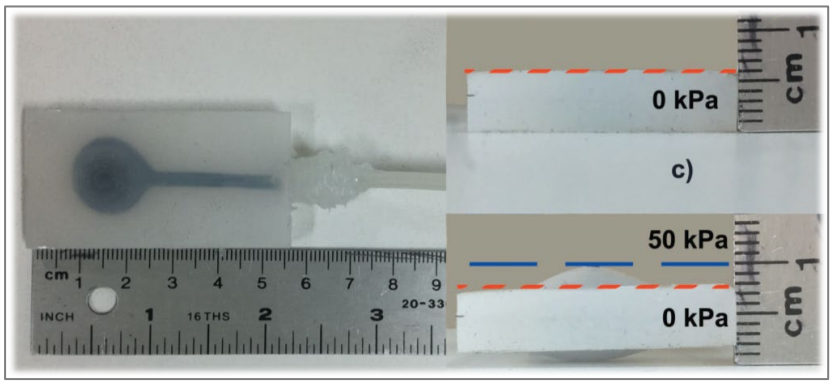

Figure 4-5 a) dimensions of a soft pneumonic actuator. b) the soft pneumonic actuator deflated. c) the soft pneumonic actuator inflated to 50 kPa (Information obtained from © 2019 IEEE [5]).

Dielectric Elastomers

These devices are fundamentally a parallel plate capacitor, where the dielectric is made of a low modulus polymer and the electrodes are typically deformable/stretchable conductors. A potential difference across the electrodes leads to electrostatic forces that compresses the polymer, which reduces the overall thickness of the structure and increases the lateral dimensions due to the Poisson effect. Figure 3-6a schematically depicts this actuation mechanism of a dielectric elastomer under the influence of a potential difference. The polymer materials are elastomers, such as silicones and polyurethanes. The relatively low dielectric constants of these materials lead to high driving voltages (>1-kV) and corresponding electric fields (>100-MV/m), with operating limits set by electrical breakdown. Single film dielectric elastomer actuators (DEAs) are typically 10-200 μm in thickness and have maximum out of plane strains between 25-35%, which corresponds to vertical a displacement of 3.5-70 μm and lateral displacement of 10-20 mm, depending on device dimensions. Multiple layers of thin DEA's are stacked on top of each other to sufficiently increase strain and blocking force. These actuators operate stably in air, are

fabricated from simple low-cost materials, experience relatively fast actuation, and exhibit high strain [6, 128].

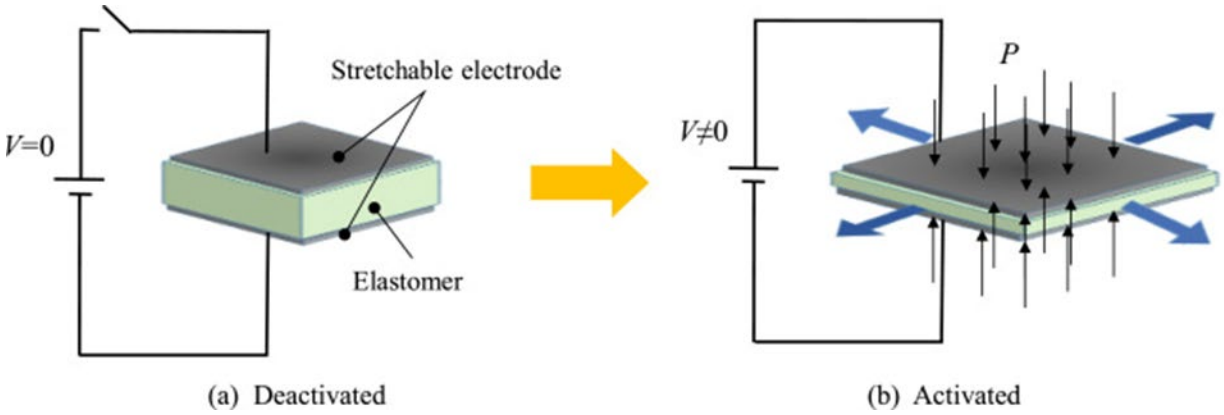

Figure 4-6 Structure and actuation of a dielectric elastomer actuator (Information obtained from © 2019 Itsuro Kajiwara, Shigeki Kitabatake, Naoki Hosoya, and Shingo Maeda. Published by Elsevier Ltd. [6]).

Plasticized PVC gels

PVC gels were first discovered to have electroactive properties by T. Hirai in 1999 (after previously being deemed electrically inactive), by adding a plasticizer to weaken the interchain dipole interactions. The mechanical properties of the gel are highly dependent on the amount of plasticizer used. Plasticized PVC gels differ from the Maxwell type deformations seen in dielectric elastomers because PVC gels experience an asymmetric deformation at the anode and cathode and a slight deformation in the direction of the electric field. The proposed mechanism of actuation is that charges injected from the cathode migrate toward and accumulate at the anode; this accumulation of charge promotes electrostatic forces between the gel and the anode, which results in deformation. Boundary conditions established by the electrodes determine the nature of this deformation. Figure 4-7 shows various types of actuation dynamics these devices can experience. Plasticized PVC gel actuators exhibit relatively fast actuation and achieve high maximum strain (~76%). However, they operate under high voltages (50-3500 V), experience hysteresis, and are often designed with rigid electrodes [4].

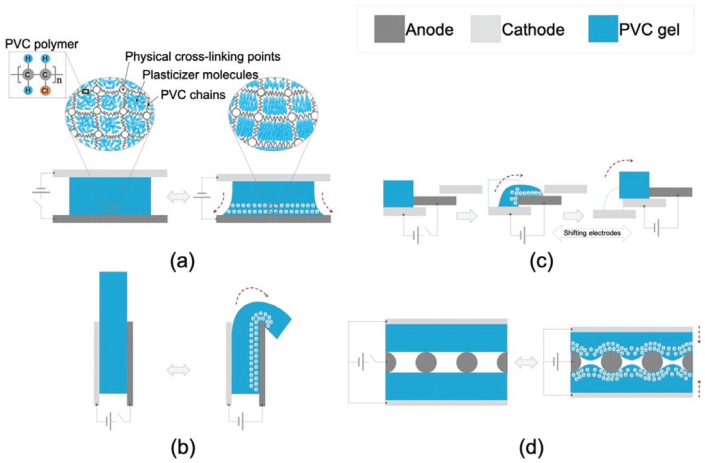

Figure 4-7 Different modes of actuation based on electrode arrangement. a) creep deformation. b) bending deformation. c) crawling deformation. d) contraction deformation (Information obtained from © 2019 The Royal Society of Chemistry [4]).

4.1.2.4 Summary

Vibrotactile displays must exceed the minimum frequency dependent force and displacement thresholds of human skin. Commercially available haptic technologies, such as electromagnetic motors and piezoelectric actuators are all rigid structures that easily generate high enough forces to deform skin. However, as we discussed in this analysis, each technology comes with limitations. Rigid structures are suitable for rigid surface haptic applications, such as in smart phones and gaming controllers. However, these devices are bulky and uncomfortable for applications that directly interact with the body, such as in wearable electronics, textiles, and biomedical devices. Emerging soft actuator technologies are more compact and able to contour to the body, making them more comfortable to wear for long periods of time. However, devices that have demonstrated that they can exceed to thresholds for human perception, such as EAPs and pneumonic actuators, experience limitations. EAPs require high voltages, which presents safety issues in wearable and biomedical devices. Pneumonic actuators require compressed air; therefore, while the tactor itself has a low profile, the technology in its entirety is bulky in impractical. Table

4-2 compares the different metrics for the various vibrotactile technologies in this space. and Table 4-3 summarizes the advantages and disadvantages of these devices.

Conducting polymer tri-layer actuators show promise in soft vibrotactile actuator applications. These devices are approximately 100 to 150 μm thick, operate under low voltages (<1 V), and can be fabricated from biocompatible materials. In addition, we are able modulate the frequency, wave form (i.e. square wave or sinusoidal), and amplitude (amplitude is proportional to voltage); this allows for more complex haptic communication beyond simple alert notifications. As we described in this section, most existing vibrotactile devices only oscillate within a narrow frequency range (i.e. LRA's) or are designed such that frequency and amplitude are coupled (i.e. ERM motors).

However, we still face the fundamental challenge with CP tri-layer actuators that they struggle to exceed the minimum force and displacement thresholds at frequencies needed for viable haptic technologies. Due to the low Young's modulus of these polymer structures, they generate blocking forces too small to deform skin. Therefore, the property that makes them adventurous as a new soft haptic technology, also creates a serious limitation. Additionally, these actuators operate at relatively low frequencies compared to the most sensitive frequency range of human skin (150-300 Hz). In Chapters 2 and 3, we discussed chemical treatments to increase the conductivity of the CP material and increase actuation speed. In this chapter, we developed a soft vibrotactile display from PEDOT:PSS/PVDF/PEDOT:PSS tri-layer actuators driven by EMITFSI ions. We treated the devices with MeOH+EMITFSI – the treatment that showed the greatest improvement to speed – and then characterized them. These preliminary results will help guide future development for viable tactor designs.

Table 4-2 Summary of quantitative comparison between commercially available vibrotactile actuators and emerging technologies.

Actuator	Solenoid	Voice Coil	LRA	ERM	Piezoelectric	Conducting Polymer	DEA	PVC Gel	Pneumatic
mechanism of actuation	linear	linear	linear	rotary	linear	bending/linear	linear	Linear/bending	linear
size	order of 10-mm	order of 10-mm	order of 10-mm	order of 10-mm	order of 10-mm (can be thin)	order of 100-µm	H: 10-700 µm D: 2-16 mm	H: 0.2-2 mm	order of 10-mm
waveform	DC	AC	AC	DC	AC	AC	DC	DC	n/a
frequency	20-500 Hz	1-300 Hz	175-235 Hz (fixed for device)	1-160 Hz (frequency and amplitude coupled to voltage)	< 200 kHz	< 100-Hz	< 3 kHz	up to 300 Hz (~5 Hz most common)	< 100-Hz
blocking force or vibrational acceleration	< 140 N	2-150 N	0.7-1.9 G	0.25-3.0 G	~ 20 N	< 10 µN	14-205 mN	not reported	1-9 N
strain or displacement	feelable	feelable	feelable	feelable	0.10%	typically < 2%	<120%	<76%	2-mm
voltage	1.5-3.3 V	~5-V	1.2-2.0 V	1.5-12 V	50-200 V	< 2-V	1-3.5 kV	50-3500 V	1-2 V
stiffness	rigid	rigid	rigid	rigid	rigid	flexible (~ 80 MPa)	flexible (0.1-1.0 MPa)	flexible (10-480 kPa -> Y variable depending on amount of plasticizer)	flexible (~3.5 MPa)

Table 4-3 Advantages and disadvantages of existing and emerging vibrotactile actuators.

Actuator	Electromagnetic	Piezoelectric	Electric EAPs	Ionic EAPs	Pneumatic
Advantages	• most common form of vibrotactile actuator (mature technology) • relatively inexpensive • come in a wide range of sizes and shapes • Work well for simple vibrations in rigid handheld devices	• High force-to-volume ratio • operate without gears • Can be made compact • non-magnetic components • Tunable by layer stacking • Short start-up time • Can create complex haptic effects	• Flexible • High strain • Thin • Force tunable through layer stacking • Low-cost materials • Relatively fast actuation	• Thin planar profile • Flexible • Low actuation voltage	• Not electrically driven • Applicable where there are geometric restrictions for sensitive regions of body
Disadvantages	• Rigid and bulky • Poor power efficiency • Heat and noise generation • Often requires complex design to achieve consistent vibrations • LRA motors can only be operated within ±2-Hz of spring resonant frequency • ERM motors couple frequency and amplitude with rotational speed. • ERM has slow start-up times	• Rigid and brittle to external shock • High driving voltage • High cost • Heat generation	• High voltage requirements • PVC gels experience hysteresis	• Relatively low speeds • Low force generation • High power requirements • Encapsulation needed	• Require high pressure air source (bulky) • Relatively slow speed.

4.2 Vibrotactile Design

We designed vibrotactile displays using our PEDOT:PSS/PVDF/PEDOT:PSS tri-layer actuators with various geometries. We specifically designed these displays to interact with the finger-tip due to the high concentration of mechanoreceptors and sensitivity of this region. Our goal was to prototype a preliminary device that could exceed the force and displacement thresholds for human perception. The following section summarizes the fabrication steps for designing these CP vibrotactile displays. These fabrication steps include the following:

1. Spray coating using a positive mask with the dimensions of the tactor.
2. Laser cutting to pattern the tri-layer films with cantilever beam arrays of varying lengths and widths.
3. Chemical post-treatment with MeOH+EMITFSI to improve the conductivity of PEDOT:PSS.
4. 3D printing of a holder to achieve tight electrical connection between the PEDOT:PSS and gold electrodes and secure to the perimeter of the device such that only the patterned area actuates.

4.2.1 Spray Coating Mask Design

We machined a new aluminum 9.1cm x 9.1 cm spray coating mask for fabricating tactile displays with dimensions that accommodated a fingertip. Figure 4-8 shows this mask design, which consists of four 1.5cm x 1.5 cm squares where PEDOT:PSS deposits on the PVDF membrane. The 1 mm diameter circles in the corners of each square facilitate an easier and more accurate machining process with a circular drill. Post-fabrication, these circular corners increase the contact area between the PEDOT:PSS and gold electrodes, which allows for a better electrical connection.

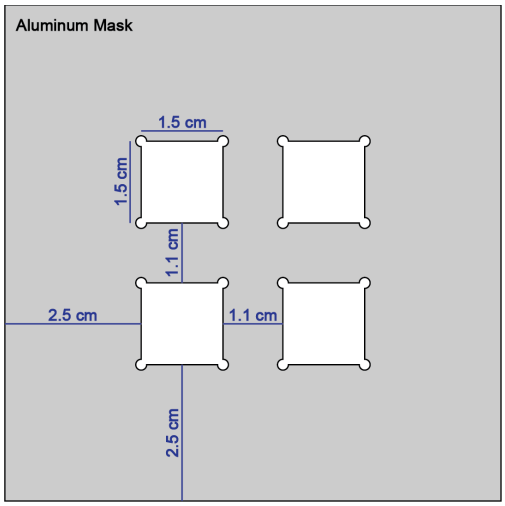

Figure 4-8 spray coating mask for vibrotactile displays.

We deposited 20 layers of PEDOT:PSS on PVDF using the methods described in Section 2.1.2.1 on spray coating. The conical spray pattern of the nozzle results in lower film thickness at the edges of the set patterning area. Therefore, we spaced each tactor square 2.5 cm from the edge of the mask to ensure the deposited PEDOT:PSS films had a uniform thickness. In previously described designs of our CP tri-layer actuators, we used a sharp razor blade to cut the PEDOT:PSS/PVDF/PEDOT:PSS samples post-deposition. However, we suspected that this damaged the edges of the PEDOT:PSS films and created an electrically conductive bridge across the PVDF membrane. To avoid this problem, we spaced each tactor square 1.1 cm apart to allow for a 0.55 cm PVDF border around each PEDOT:PSS electrode.

4.2.2 Laser Cutting

We used a laser cutter (Oxford Lasers) to pattern each tactor. This technique involves a non-contact process that thermally removes material. The removed thickness is proportional to the power, number of passes, and reciprocal of velocity. We first calibrated a recipe that removed the full thickness of material, without burning the edges of the sample, by etching small holes in spare material. Thibault *et al.* previously described the relationship between removed material,

thickness, and the three mentioned experimental parameters, which we used to guide the design of our protocol [143]. We set the relative laser intensity to 50% output. The laser passed over our samples 5 times at a dot moving speed of 1 mm/s. Figure 4-9 shows the four patterns we fabricated, which we referred to as the following:

1. Long/wide (6 beams: L = 0.5 cm & W = 0.25 cm)
2. Long/narrow (12 beams: L = 0.5 cm & W = 0.10 cm)
3. Short/wide (12 beams: L = 0.2 cm & W = 0.25 cm)
4. Short/narrow (24 beams: L = 0.2 cm & W = 0.0.10 cm)

Here, 'long' and 'short' refer to beam lengths of ~0.5 cm and ~0.2 cm, respectively. The 'wide' and 'narrow' labels refer to beam widths of 0.25 cm and 0.10 cm, respectively. Each pattern had outer dimensions of 1cm x 1cm. The 0.25 cm border provided an area for electrical contact between the PEDOT:PSS and gold electrodes.

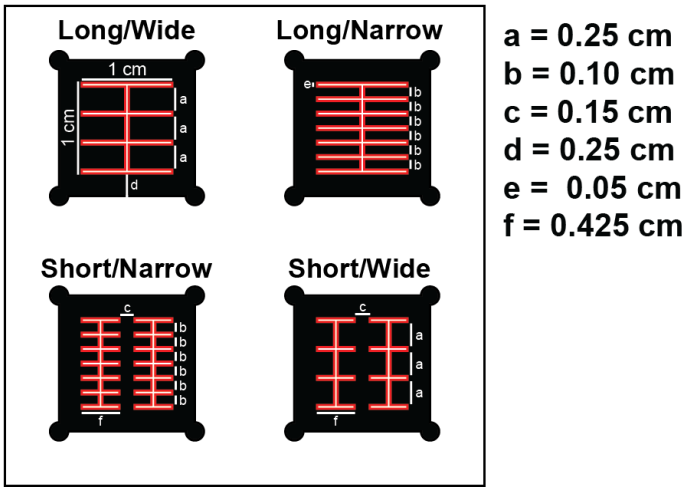

Figure 4-9 Laser cutter designs patterned into PEDOT:PSS/PVDF/PEDOT:PSS tactors.

4.2.3 Chemical Post-Treatment

Based on our analysis in Chapters 2 and 3, we concluded that MeOH+EMITFSI treatment most successfully improved actuation speed. Therefore, we applied this treatment to the tactors shown in Figure 4-10. We used the methods described in Section 2.1.2.2 on MeOH+EMITFSI solvent treatment.

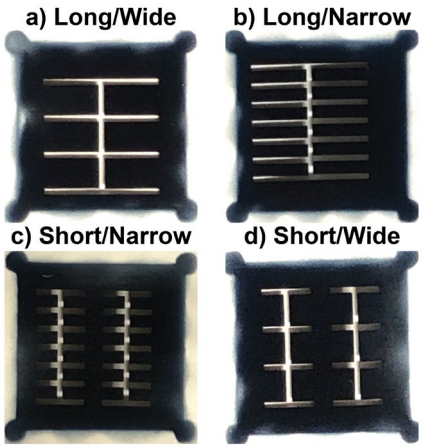

Figure 4-10 Patterned PEDOT:PSS/PVDF/PEDOT:PSS tr-layer actuator tactors.

4.2.4 Tactor Holder and Electrical Connection

We designed a holder for the tactor in Solidworks (3DS 2020) to allow for tight electrical connection between the PEDOT:PSS and gold electrodes. The holders were 3D printed using a Flashforge Dreamer 3D Printer. This design secured the 0.25 cm border of the tactors while allowing an open square space for the cantilever beam arrays to freely actuate. We used nylon flathead screws and washers to clamp the two sides of the holder together. We cut gold foil, described in Section 2.1.1.4 (on contact electrodes), into 0.30 cm wide strips and attached them to the holder such that they continuously bordered the actuators.

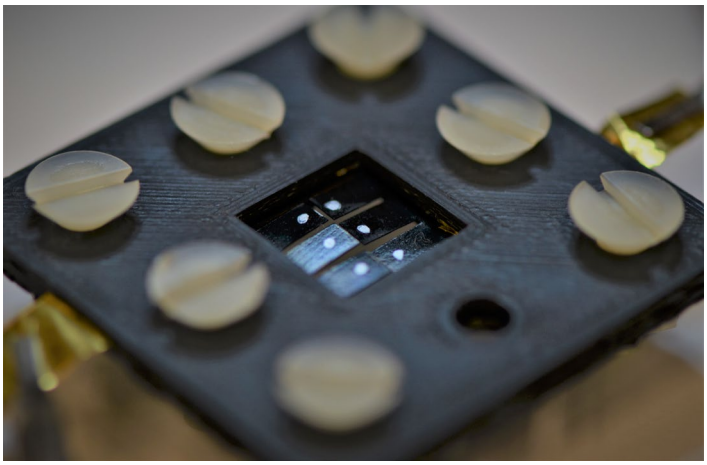

Figure 4-11 Vibrotactile display (Long/Wide) clamped in 3D printed holder with gold foil contact electrodes. Silver dots are applied to enable measurement of displacement.

4.3 Characterization

We performed actuation frequency response measurements, EIS, and force modelling on each of the actuators, based on the methods described in Sections 3.2.1, 3.3.1, and 3.4.1.1, respectively. We used these measurements to characterize the feasibility of our devices as vibrotactile displays.

4.3.1 Tactor Actuation Frequency Response

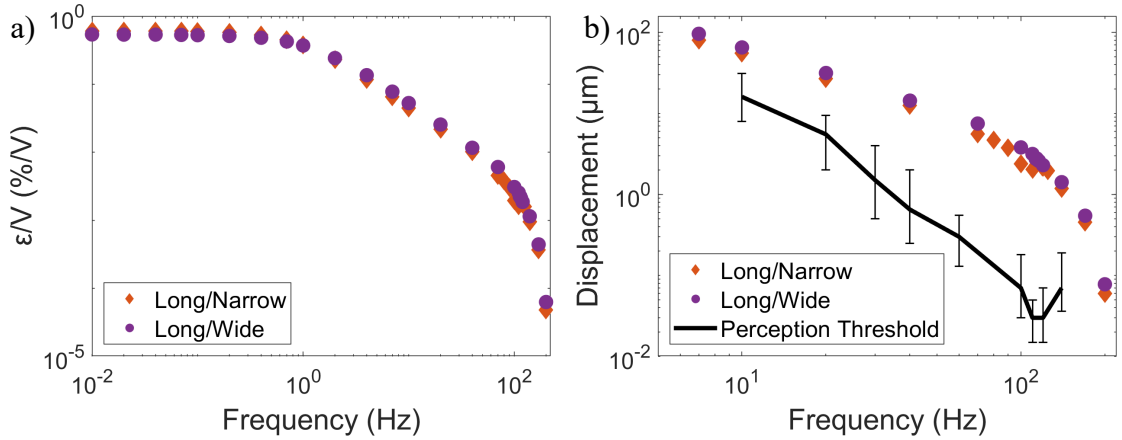

Figure 4-12 a) strain vs. frequency response for MeOH+EMITFSI treated tactors (Long/Narrow and Long/Wide) at ± 0.5V. b) Displacement vs. frequency response of MeOH+EMITFSI treated tactors (Long/Narrow and Long/Wide) compared to the frequency dependent minimum perception threshold of human glabrous skin on the finger (Adapted from © 1999 The American Physiological Society [1]).

We measured the displacement of a single beam on each tactor using a laser displacement sensor (Keyence LK-G32). We applied a sine wave voltage with an amplitude of 500 mV from 0.01 Hz to 220 Hz. Figure 4-12a shows the full actuation frequency response of the Long/Narrow and Long/Wide tactor. The long/narrow tactor achieved the highest displacement of 744.2 μm at 0.01 Hz, which corresponded to a free strain of 0.60%/V, based on Equation (3-5). The long/wide beam displaced 667.5 μm at 0.01 Hz and experienced free strain of 0.54 %/V. These displacements were over 2x larger than the maximum deflection of the 5 mm long MeOH+EMITFSI treated beam we described in Section 3.2.3.4. However, the tactors had a lower f_c of 1 Hz, compared to 4 Hz for MeOH+EMITFSI treated samples described in Section 3.2.3.3. Table 4-4 summarizes these results.

Table 4-4 Summary of measured parameters for MeOH+EMITFSI treated PEDOT:PSS/PVDF/PEDOT:PSS tri-layer tactors (Long/Narrow and Long/Wide). Free strain/voltage (ϵ/V) and strain-to-charge ratios (α) are also tabulated.

Tactor	D (μm) - measured at 500mV & f = 0.01 Hz	Mechanical f_c (Hz)	ϵ/V (%/V)	α (mm^3/C)
Long/Narrow	744.2	1	0.60	0.2
Long/Wide	667.5	1	0.54	0.2

Multiple factors likely contributed to this reduction in speed. Leakage between the two CP electrodes may have resulted from the laser cutting process, which thermally removed material and potentially carbonized the edges of the tactor pattern. However, as the Bode phase plot shows in Figure 4-13b, phase angle for both tactors reached nearly -90° and plateaued, which suggests leakage is not the main problem. Higher contact resistance, due to the experimental setup, is likely a large contributing factor to the higher resistance and lower cut-off frequency of the tactor system.

Both short samples exhibited highly resistive behavior and did not generate any measurable displacement. Therefore, we could not record their mechanical frequency response. We suspect the PEDOT:PSS electrodes were damaged during laser cutting. We observed the edges were discolored as a result of the thermal process burning the material. This resulted in a short between the CP electrodes. The proportion of undamaged active material remaining was too small to facilitate high enough charge transfer to generate actuation, due to the small dimensions of the short beams.

Figure 4-12b shows the free displacement of our long tactors compared to the threshold of human perception described by Brisben *et al.* and Israr *et al.* [1, 2]. At the most sensitive frequency range of skin, between 150 and 160 Hz, free beam deflection of the actuators was approximately two orders of magnitude above the minimum perceptible skin deflection threshold. However, beam deflection rapidly decreased and intercepted with the threshold plots around 200 Hz. At 10 Hz, skin exhibited lower sensitivity; however, our actuators' free deflection still exceeded the

perception threshold by about 4 times. However, despite the free displacement easily exceeding the minimum required to activate skin mechanoreceptors, the flexibility of the CP tri-layer actuators means that the skin impedes the devices from achieving maximum deflection when pushing against the fingertip. In Section 4.3.4 we use a viscoelastic model of skin to predict the extent of skin deformation our actuators achieve. First, though, we look at the impedances of the long tri-layers and compute the anticipated blocking forces.

4.3.2 Electrochemical Impedance Spectroscopy

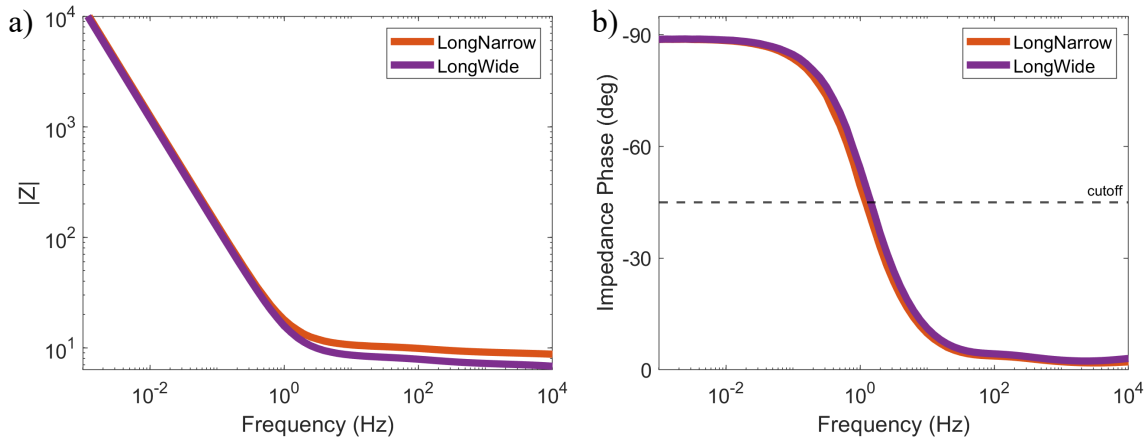

Figure 4-13 Bode a) magnitude and b) phase plots of the impedance for Long/Narrow and Long/Wide PEDOT:PSS/PVDF/PEDOT:PSS tri-layer tactors under an applied sinusoidal voltage with an amplitude of 10mV.

We performed EIS measurements by applying a sinusoidal voltage with an amplitude of 10 mV and frequency sweep from 10^6 Hz to 10^{-3} Hz, using a Solartron 1287A Potentiostat/Galvanostat (Hampshire, UK) with a Solartron 1260A Frequency Response Analyzer. For both tactors, impedance phase was close to zero at high frequencies, which indicated nearly pure resistive behavior. Figure 4-13b shows that impedance phase decreases as frequency of the applied voltage decreases, which indicates charging/discharging as the device becomes more capacitive.

At low frequencies the long/narrow and long/wide tactors reach phase angles of -88.8° and -88.9°, respectively. This near -90° phase shift indicated that the tactors behaved as almost ideal capacitors. The |Z| Bode plots in Figure 4-13a show that the slopes of the long/narrow and long/wide samples are -0.98 and -0.99, respectively. These results further demonstrated the near ideal capacitive nature of the tactors. The MeOH+EMITFSI treated tactors replicated the measurements for MeOH+EMTIFSI treated samples described in Section 3.3. This suggests that the fabrication technique we used to design the tactors did not damage them and cause leakage or a short circuit. Conversely, the short/narrow and short/wide samples exhibited purely resistive behavior, even at low frequencies.

We measured this f_c for the long/narrow and long/wide samples to equal 1.3 Hz and 1.6 Hz, respectively. These f_c values agree with the f_c values we measured from the actuation-frequency response. Table 4-5 summarizes these results.

Table 4-5 Summary of cut-off frequencies (at phase = -45°) and slope of Bode magnitude plot for pristine and treated PEDOT:PSS/PVDF/PEDOT:PSS tactors.

	Long/Narrow	Long/Wide
f_c (Hz)	1.3	1.6
Bode Slope	-0.98	-0.99

We applied the same equivalent circuit model consisting of a resistor in series with a Warburg open element, described in Section 3.3.2, to the Bode plots generate for the MeOH+EMITFSI treated long/narrow and long/wide samples. Table 4-6 summarizes these results. In both models, $\propto \approx 0.5$. This showed that the systems exhibited nearly ideal Warburg characteristics and were diffusion controlled. The τ values for long/narrow and long/wide tactors were 0.062s and 0.057s, respectively. These values corresponded to f_c values of 2.6 Hz and 2.8 Hz, which fall within the range of f_c values we previously calculated from the actuation-frequency response data for MeOH+EMITFSI treated samples.

We used this model to calculated capacitance (C) from the Warburg RC time constant (τ) and resistance (Z_0). These values were 11.7 mF and 12.4 mF for long/narrow and long/wide tactors, respectively. We also compared the R_s and Z_0 values obtained in this model to the R_i values we measured in Section 2.6.2 (Ionic Conductivity). R_i for these MeOH+EMITFSI treated samples was 2.8 Ω, which was lower than the modelled R_s and Z_0 values, for both tactors. We suspect contact resistance contributed significantly to the overall impedance of the system, which helps explain why we observed a decrease in f_c compared to previously described MeOH+EMITSI treated samples in Chapter 3. These values suggested that contact resistance, in addition to ionic resistance through the conducting polymer layers, dominated the RC time constant in these samples.

Table 4-6 Summary of EIS equivalent circuit modelling results of long/narrow and long/wide tactors for the following elements: solution resistance (R_s), Warburg open impedance (Z_0), Warburg open time constant (τ) and Warburg open phase (α). From these results, capacitance (C) and volumetric capacitance (C_v) were calculated based on the specific tactor geometry. Ionic resistance (R_i), based on the measured ionic conductivity and specific tactor geometry is also presented here.

Long/Narrow			Long/Wide		
Element	**Value**	**error**	**Element**	**Value**	**error**
Rs (Ω)	9.1	0.03	**Rs (Ω)**	7.1	0.02
Z_0 (Ω)	5.3	0.2	**Z_0 (Ω)**	4.6	0.1
τ (s)	0.062	0.002	**τ (s)**	0.057	0.002
α	0.49	0.0004	**α**	0.49	0.0004
C (mF)	11.7	0.05	**C (mF)**	12.4	0.05
C_v (F/cm^3)	10.9	-	**C_v (F/cm^3)**	11.5	-
R_i	2.8	-	**R_i**	2.8	-

4.3.3 Blocking Force Modelling

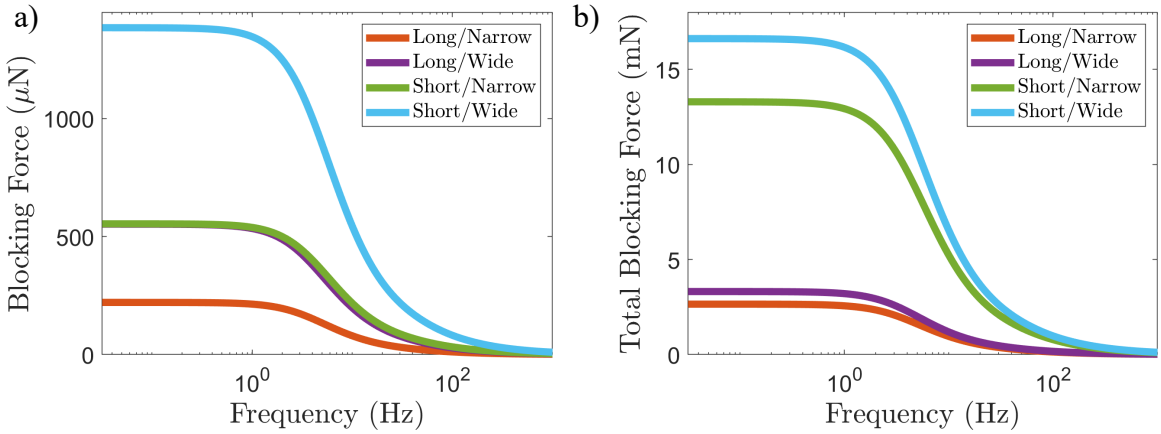

Figure 4-14 a) Modelled blocking force of an individual beam for each tactor design. b) total blocking force generated by each tactor based on the number of beams in the design.

We applied the Actuatool model described in Section 3.4.1 to predict F_B for each tactor design. We modelled beams with the dimensions described for long/narrow, long/wide, short/narrow, and short/wide tactors. Figure 4-14a illustrates these results. Based Equation (4-1),

$$\frac{F_B(f)}{V(f)} \approx \epsilon(f)\left[\frac{3W}{2L}E_p h_p\left(h_p + h_g\right)\right], \tag{4-1}$$

we know that width (W) is proportional, and length (L) is inversely proportional to F_B. We previously described this equation in Section 3.4.1. The modelled results reflected these trends; the short/wide sample generated the highest F_B across the entire frequency sweep, with a maximum value of 1.4 mN. Conversely, the long/narrow generated the lowest frequency dependent F_B, with a maximum value of 221 μm. The long/wide and short/narrow tactors exhibited approximately equal F_B versus frequency curves. The geometry of the beams did not appear to affect the speed of the devices. As we discussed in Section 3.5 on comparing cut-off frequencies, this is likely because the speed of the CP actuators is dominated by diffusion of ions through the thickness of the

PEDOT:PSS electrodes, rather than electrical charging along the length of the beam. Therefore, the main effect of electronic conductivity is only seen at $f > f_c$.

We then multiplied the F_B calculated by a single beam by the number of beams in each tactor design ($n_{long/narrow} = 12$, $n_{long/wide} = 6$, $n_{short/narrow} = 24$, $n_{short/wide} = 12$). Figure 4-14b shows that the short/wide and short/narrow tactors generated the highest F_B values across the frequency range, with maximum values of 16.6 mN and 13.2 mN, respectively. Despite these promising high theoretical F_B values calculated for short tactors, the reality of these designs is limited by the fabrication process. We need to develop a method of non-destructively patterning the tactors.

4.3.4 Viscoelastic Model for Skin Displacement

The softness and compliance of the skin plays a major role in the sense of touch. When skin contacts an object, it conforms and contours around the surface. This resultant skin deformation stimulates mechanoreceptors. Wiertlewski *et al.* applied a Kelvin-Voigt model to describe the frequency-dependent viscoelastic response of skin on the tip of the index finger [139]. This model represented the material as a purely viscous damper and purely elastic spring connected in parallel. Mechanical impedance (Z) is a measure of the resistance in a mechanical structure against an applied vibration [2]. Equation (4-2) represents the impedance of the system with the inertial effects also included in parallel:

$$Z(j\omega) = b + j\left(m\omega - \frac{k}{\omega}\right), \tag{4-2}$$

where m is the moving mass, b is the viscosity, k is the stiffness, and j is the imaginary component. Wiertlewski *et al.* found that skin predominantly behaved elastically up to about 100 Hz and was then damping dominated above this frequency; They neglected inertial contributions at frequencies below 500 Hz [139].

To capture the dynamic behavior in such a Kelvin-Voigt model (parallel spring and dashpot), we assumed that stress (σ) was a function of deformation described by Equation (4-3):

$$\sigma = E\varepsilon + \eta\dot{\varepsilon}\ , \tag{4-3}$$

where η is viscosity. We estimated the complex dynamic modulus from the effective stiffness (K^*) of the material, which is made up of real and imaginary parts according to Equation (4-4):

$$K^* = bj\omega + k\ , \tag{4-4}$$

where k is the real component of stiffness in the proximal-distal direction. Wiertlewski *et al.* measured k and b in a cohort of seven participants and found an average values of (1.33 ± 0.16) N/mm and (1.39 ± 0.17) N s/m, respectively [139]. Here, the effective stiffness is the integral of the impedance, which is obtained by multiplying Z in Equation (4-2) by $j\omega$. We assumed that the frequency dependent F_B generated by our tactors equaled the skin reaction force ($F_B = F_s$). Based on these values, we predicted the extent of skin displacement our four tactors generated and compared these with the minimum perceptible displacement found experimentally by Brisben *et al.* (black) and Israr *et al.* (grey) [1, 2]. Figure 4-15a shows these results, suggesting there are frequency regions where the cantilever actuation may be perceptible.

Due to the relatively low elastic modulus of the PEDOT:PSS/PVDF/PEDOT:PSS tri-layer actuators, the skin impeded displacement of these tactors. Based on the relatively high F_B values short tactors theoretically achieved, we predicted these actuators could exceed the minimum perception threshold at frequencies greater than ~30 Hz (assuming we can fabricate these without laser damage – which so far has been a challenge). The long tactors displaced the skin above the

perception threshold from 80 to 200 Hz, which is within the most sensitive frequency range for glabrous skin [1, 2, 138].

Figure 4-15b shows the estimated minimum frequency dependent force threshold our tactors need to exceed to sufficiently displace the skin. We calculated these values based on the viscoelastic model of skin described by Wiertlewski *et al.* and perception displacement threshold described by Brisben *et al.* (black) [1, 138, 139]. The plot also shows the experimentally measured force threshold, which was presented by Israr *et al.* (grey) [2]. The modelled force threshold is slightly lower than the experimentally determined values. However, we also observed this discrepancy between the displacement threshold data presented by each study, which helps to validate our viscoelastic model for skin. These results showed that the minimum specifications we need to meet for designing feelable CP tactors are ~56 µN at 150 Hz. However, as frequency decreases, minimum force requirements rapidly become much higher.

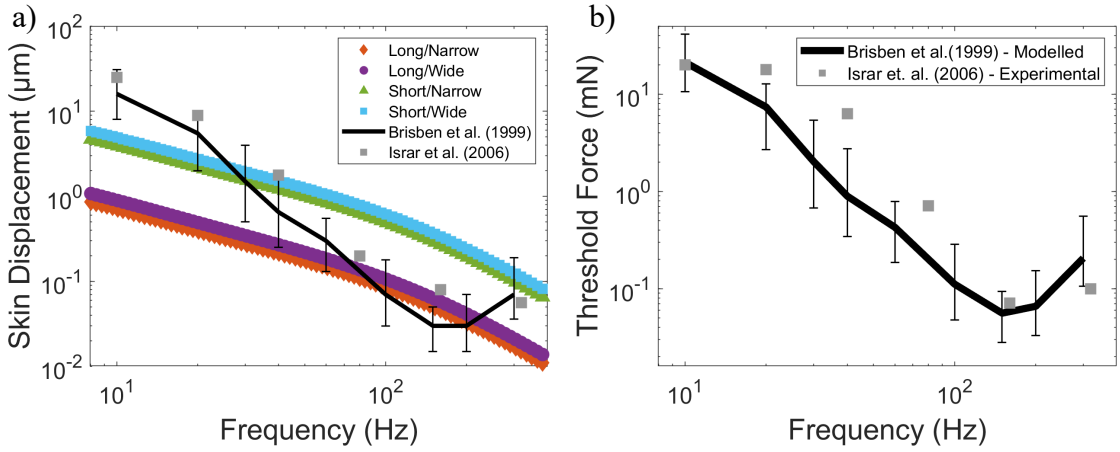

Figure 4-15 a) skin displacement of PEDOT:PSS/PVDF/PEDOT:PSS tri-layer tactors with four different geometries compared to the perception threshold of glabrous skin measured by Brisben *et al.* and Israr *et al.* b) Prediction of minimum frequency dependent F_B the tactors need to achieve to displace skin a perceptible amount, based on displacement threshold results presented by Brisben *et al.* and experimental force threshold results presented by Israr *et al.* (Adapted from © 1999, The American Physiological Society [1] and © 2006, IEEE [2]).

The estimates shown in Figure 4-15 will help guide our future designs, and indicate if we expect displacements and forces to exceed the perception thresholds. Based on our measurements

of free displacement in Figure 4-12, we achieved sufficient displacement but not force. Further work to optimize these two effects may allow us to find a design range for feelable tactors.

In very preliminary experimental observations, we found that the long/wide tactors were feelable for some of the research team when we applied a sinusoidal voltage with an amplitude of 500 mV at ~50 Hz. Each person placed their index finger over the tactor in the apparatus shown in Figure 4-11 and expressed whether they could feel the device vibrating against their skin. One member of our research team eloquently described the sensation as "a fly wing fluttering against the skin". However, we need to conduct formal human perception studies to better assess the feasibility of this technology in future work.

Not all members of the team could sense the tactors. Two members in their fifties did not sense any vibrations. This combination of just perceptible detection by three members of the team, and no detection by two others, supports our conclusions that we need to design tactors that generate higher forces. We predict that we can achieve this by shortening the actuator length to increase force and compromise free displacement, since our evaluation above suggests force, rather than displacement, limits viability of the technology as tactors.

4.4 Analysis of soft vibrotactile displays in the context of perception acuity

The biomechanical properties of skin widely differ between people based on various factors such as gender and age. However, the exact trends of skin elastic modulus as a function of age and gender are widely disputed in the literature [144]. Most generally, skin tends to stiffen and thicken with age, but at a lower rate in women than men [144]. Hall *et al.* suggested that this increase in Young's modulus resulted from a decrease in the ratio of chondroitin-sulfate and keratin-sulfate in the dermis, which diminished the collagen fibers' ability to deform [145]. Another study by Park *et al.* showed that water content in the skin decreased with age, which

caused the organ to lose elastic properties [146]. These physiological changes contribute to the decrease in perceptual acuity with age. Confounding variables, such as occupation, demographic, and socioeconomic status likely influence the large discrepancies in this area of research [144].

A study by Peters *et al.* showed that the number of mechanoreceptors in the finger was approximately constant between all subjects. Therefore, individuals with smaller hands tended to have more densely packed receptors and therefore exhibited higher perceptual acuity [147]. Since females are typically smaller, their fingers produce a finer-grained afferent neural image of an impressed tactile stimulus. This helps explain why women often exhibit a lower perceptual threshold. This study showed that finger size is the sole determinant of tactile acuity, regardless of gender. Interestingly, they did not find that women had more compliant skin than men, which refuted the study hypothesis that this was the reason for superior perceptual acuity in women.

The research in this space shows the wide variety of factors that contribute to the sense of touch. Therefore, while we did develop a predictive model that provided an estimate for the efficacy of our CP vibrotactile displays, there is no set of definitive parameters we can turn to, to establish a threshold for what will constitute a viable technology in this space. In future work, we plan to further prototype tactor designs to maximize F_B, strain, speed, and skin displacement. We plan to conduct in human studies to assess the viability of this technology as a thin flexible vibrotactile display.

Chapter 5: Conclusion

5.1 Summary of Work Done

The objective of this work was to optimize the electrical, ionic, and material properties of PEDOT:PSS to increase the charge storage capabilities of the material, and reduce the overall impedance of the system. The end goal was to increase the actuation speed of these CP tri-layer devices such that they achieved sufficient displacements and forces at physiologically relevant frequencies for applications such as vibrotactile haptic displays. As predicted, based on previous work to improve the electrical properties of PEDOT:PSS, we showed that post-treating PEDOT:PSS/PVDF/PEDOT:PSS tri-layer actuators with polar solvents and ionic liquid significantly increased the conductivity of the polymer material. Treatments with MeOH, MeOH+EMITFSI, EG, EG+EMITFSI, and DMSO all increased the electrical conductivity by one order of magnitude. To our knowledge, we reported the highest electrical conductivity values for PEDOT:PSS- or PEDOT-based conducting polymer actuators.

We also found that these chemical post-treatments improved ionic conductivity. Most significantly, MeOH+EMITFSI and EG+EMITFSI increased PEDOT:PSS ionic conductivity by at least two orders of magnitude. We proposed that this was due to the polar solvent removing hydrophilic PSS from the polymer structure, which created voids in the structure that were filled by the ionic liquid. Through this mechanism, the conducting polymer electrodes became more porous, which reduced the resistance to ion diffusion through the structure. A study by Liu *et al.* showed that polar solvent treatment increased porosity of PEDOT:PSS films, which resulted in improved electrochemical performance [105].

Cyclic voltammetry measurements showed symmetric and rectangular I-V response, which indicated that our systems behaved as capacitors and no redox processes occurred during

charging/discharging. From these results, we calculated the capacitance of the system. Pure polar solvent treatments nearly doubled volumetric capacitance, compared to untreated samples. Additionally, we analyzed the current rise times of the CV curves, which showed that all treatments increased the charging/discharging speed of the actuators. MeOH+EMITFSI treatment reduced the RC time constant from 0.29 s to 0.04 s. This treatment also had the largest effect on ionic conductivity, which suggested that ion diffusion through the PEDOT:PSS electrodes is the largest contributor to impedance of the tri-layer system.

Previous work that studied the mechanisms of how polar solvents improve electrical conductivity suggested that they dissolved out PSS. We performed three measurements to build a case that supported our hypothesis that we were removing PSS from our material. First we showed that, while pristine PEDOT:PSS sampled readily dissolved in water, treated samples were stable in an aqueous environment. Next, we showed that the mass of samples treated with polar solvents decreased, which suggested that we removed material. Finally, we used XPS analysis to measure the ratio of PSS to PEDOT on the surface of our samples. These results showed that the proportion of PSS on the surface of the samples decreased following chemical treatment. MeOH+EMTIFSI and EG+EMITFSI treatments exhibited the largest decrease.

Next we characterized the mechanical properties of our PEDOT:PSS/PVDF/PEDOT:PSS tri-layer actuators. We predicted that increasing electric and ionic conductivities of PEDOT:PSS would increase the displacement of tri-layer cantilever beams at high frequencies. Our results showed that MeOH+EMITFSI and EG+EMITFSI treatments increased the cut-off frequency by one order of magnitude. These results further supported our analysis that ionic resistance contributed most to limiting the speed of actuation, especially at low frequencies and for the geometry we investigated. If our tri-layers were significantly longer (about 2.5 times longer in the

pristine case, and 7 times longer for the treated material), or less conductive, we expect the electronic conductivity would dominate the frequency response [148].

EIS analysis showed that samples treated with polar solvent mixed with IL behaved as nearly ideal capacitors. At low frequencies, the phase angle was almost -90° and the bode slope was approximately -1. We represented these results using the equivalent circuit model of a resistor in series with a Warburg open element. Warburg impedance represents 1D diffusion behavior and further shows that the actuation of our devices was controlled by the rate at which ions migrate through the system. Samples treated purely with polar solvents exhibited multiple rises and plateaus across the frequency sweep. This suggested that they experience multiple time constants, possibly as a result of varying distribution gradient of PEDOT:PSS into the thickness of the PVDF membrane [100].

We also used a 2D transmission line analytical model to predict the blocking force generated by our treated tri-layer actuators. Compared to pristine samples, samples treated with polar solvents produced higher blocking forces at low frequencies. Conversely, actuators treated with the polar solvent and ionic liquid mixture exhibited a large drop in maximum blocking force. These trends directly correspond in the changes in Young's modulus. However, as with the displacement-frequency response, tri-layers treated with MeOH+EMITFSI and EG+EMITFSI maintained maximum blocking force at higher speeds. At frequencies relevant for vibrotactile devices, these samples exhibited the highest blocking force. Previous work by Temmer *et al.* showed that using PEDOT/Ppy composite electrodes increased the maximum force generation of CP tri-layers, while maintaining the actuation speed exhibited by pure PEDOT devices. In future work we plan to investigate way to increase force generation at the high speeds relevant for applications such as vibrotactile devices.

In the final chapter of this work, we explored the feasibility of our PEDOT:PSS/PVDF/PEDOT:PSS tri-layer actuators as vibrotactile displays. Human sense of touch is highly developed; the somatosensory system allows us to experience and interpret tactile stimuli. Fast adapting mechanoreceptors located in the dermis layer of skin are sensitive to vibrations. Vibrotactile haptic devices exploit these end organs to communicate messages to the body through vibration. Skin is a viscoelastic material and therefore exhibits a time-dependent modulus. Previous work in the field of psychophysics have characterized the absolute displacement and force thresholds of glabrous skin on the hand as a function of frequency [1, 2, 138].

We prototyped four designs of cantilever beam arrays with varying lengths and widths. Actuation frequency response measurements showed that free displacement of these tactors exceed the minimum perception threshold by up to two orders of magnitude (in the most sensitive frequency range). However, due to the compliant nature of these soft, flexible actuators, force generation was low. We presented a viscoelastic Kelvin-Voigt model for skin, based on a study by Wiertlewski *et al.* [139]. This allowed us to predict the extent of skin displacement our tactors could achieve. Our results showed that blocking force, rather than free displacement, at high frequencies limited the viability of our devices. Therefore, we concluded that we need to design short wide beams that optimize force output. Promising initial observations suggested that our devices are actuating right at the limit of human perception. Young members of our research team (<30 years old) were able to sense slight vibration against their fingertip.

5.2 Applications

Wearable vibrotactile devices have many potential and existing applications, such as non-invasive medical, assistive, and communication devices. Additionally, vibrotactile displays incorporated into virtual and augmented reality devices can provide closed loop sensory feedback, both for applications such as medical, rehabilitative, and recreational gaming devices. Most practical applications require actuators with small form factors that comfortably interface on the body [149]. Artificial muscle technologies, such as our conducting polymer tri-layer actuators, offer a novel alternative to the standard rigid, bulky electromagnetic motors typically employed. Vibrotactile displays have been incorporated into clothing and watches. They have also been suggested as an accessible communication channel for the hard-of-hearing [150] and visually impaired [151-153]. Previous studies have developed and described braille cells fabricated from polymeric materials, such as elastomers, which translate visual information into vibrotactile feedback for the visually impaired [154, 155].

Another application is vibrotactile haptic feedback to modulate grip force in minimally invasive robotic surgery. Robotic surgery offers advantages such as ease of operation and reduced procedure times. However, surgeons lose force feedback cues when they utilize these techniques. This loss of haptic feedback coupled with the inherent ability of robotic surgical systems to apply strong compressive and shear forces, have led to increased risk of tissue damage, reduced performance, and increased number of mistakes [156]. Vibrotactile devices that can modulate force and vibration to communicate complex information may provide a solution to these limitations [157].

Sensory feedback is important for prosthetic devices to provide users with a sense of limb embodiment. Advancements in myoelectric prosthetics have largely focused on augmenting lost

motor function. However, restoring sensory function remains an unresolved problem for these devices. Specifically, upper limb loss is one of the most difficult prosthetic replacements due to the complexity of fine sensory input and dexterous function of the hand. This type of injury is often devastating and can greatly reduce quality of life and independence. Currently, users are forced to rely heavily on vision, which increases the conscious attention needed to operate their prosthetic [137, 158]. Prothesis abandonment rates are between 23-39%, with many users reporting lack of physiologically relevant sensation as a major reason for rejecting their device [159, 160].

Vibrotactile stimulation strategically placed on the residual limb of an amputee can provide sensory feedback about their prosthetic hand, with training. Phantom hand mapping and targeted muscle reinnervation (TMR; a reconstructive procedure that strategically relocates residual nerves that once served the patients amputated hand to targeted muscle sites on the residual limb or chest) are the two primary methods used to identify regions on the residual limb that are associated with regions on the missing hand; these techniques restore the sensation of touch [161]. Conversely, several studies have shown that the kinesthetic illusion is elicited by vibrating actuators at specific frequencies (70-110Hz) and amplitudes (0.1-0.5mm) on musculotendinous regions, to communicate the positional state of prosthetic joints. This activation results in an illusionary sense of limb movement, while the joint itself remains stationary [135, 137, 162].

Previous studies on vibrational feedback and prosthetics have typically used small commercially available piezoelectric motors that activate Pacinian corpuscles (dermal mechanoreceptors sensitive to vibration) when applied to the skin [163]. These devices are stiff and bulky, which limits their applicability in commercial prosthetics. There is a small amount of space inside the socket because it typically must be vacuum sealed in place over the stump [137, 164]. Artificial muscle actuators fabricated from CPs are a promising alternative to traditional

tactors due to their comparably large strain (typically 2% or greater), high compliance, planar configuration, low cost, and low actuation voltage (<2 V) [3, 8, 32].

5.3 Future Work

In future work, we need to further improve the speed and force output of our conducting polymer tri-layer actuators, such that they can exceed the absolute thresholds for human perception within the physiologically relevant frequency range. We observed benefits and trade-offs to adjusting the electrochemical properties of our tri-layer actuators. Increasing electrical conductivity did not unanimously increase cut-off frequency; however, an increase in electrical conductivity did correspond to an increase in displacement amplitude at frequencies above the cut-off frequency. Treatment with polar solvents mixed with ionic liquid increased ionic conductivity by up to 300x, which increased cut-off frequency and high-speed displacement and force amplitudes. However, these treatments decreased stiffness of the conducting polymer, which reduced maximum displacement and force generation at low frequencies. Treatments with pure polar solvents nearly doubled the conducting polymer stiffness, which resulted in higher maximum displacement and blocking force. Pure polar solvents also increased the volumetric capacitance of the CP tri-layers. This further contributed to the increase in low-frequency displacement and blocking force, since charge is proportional to deformation. These results show that the trade-offs between conductivity and stiffness of PEDOT:PSS need to be optimized for the application specifications.

Increasing the width of each beam also increases blocking force but with little effect on beam deflection or speed. However, the width of the actuators is limited by the dimensions of the particular body part we are targeting. Thicknesses of the conducting polymer and separator layers are also parameters we can optimize to maximize displacement, speed and blocking force. As we

increase thickness, the structures generate higher forces, but also exhibit higher ionic resistance. We are also not limited to rectangular cantilever beam array designs. We plan to explore other patterns, such as spirals. We also may be able to increase displacement and force generation without compromising speed by stacking actuators, which is a technique commonly applied in piezoelectric and EAP actuators [166].

We also need to further investigate tactor fabrication techniques. In particular, laser cutting the tactor patterns into our samples caused damage. Parameters such as intensity, laser velocity and number of passes are all aspects of the recipe we can alter to prevent this from occurring. Physically cutting the samples presents challenges with regards to precision, due to the nature of this manual process. We also observed that using a sharp razor blade to cut the tri-layer samples sometimes resulted in short circuiting as the two conducting polymer electrodes were pushed together.

We also plan to explore alternative electrolytes. The PEDOT:PSS films became stable in water following polar solvent treatment, which opens up the opportunity to explore aqueous electrolytes. Previous work has shown that aqueous salts, such as KOH(aq) and Na2SO4(aq) increase actuation speed, due to lower solution resistance than ionic liquids [97]. This will also necessitate encapsulation, due to the volatile nature of aqueous electrolytes [165].

In summary, we showed that improving electrical and ionic conductivity improves the high-speed actuation frequency response. High-speed conducting polymer tri-layer actuators have potential in vibrotactile haptic display applications, due to their small geometry and compliant material properties. In future work we need to further develop this technology such that we achieve higher displacement and force outputs to overcome the absolute threshold of human perception within the physiologically relevant frequency range.

References

[1] A. J. Brisben, S. S. Hsiao, and K. O. Johnson, "Detection of vibration transmitted through an object grasped in the hand," *J Neurophysiol,* vol. 81, pp. 1548-58, Apr 1999.

[2] A. Israr, S. Choi, and H. Z. Tan, "Detection Threshold and Mechanical Impedance of the Hand in a Pen-Hold Posture," in *IEEE International Workshop on Intelligent Robots and Systems*, Beijing, China, 2006, pp. 472-477.

[3] S. Ebrahimi Takalloo, "Actualizing fast conducting polymer actuators: design optimization, fabrication, and encapsulation," Doctor of Philosophhy, Electrical and Computer Engineering, University of British Columbia, Vancouver, British Columbia, 2019.

[4] Y. Li, M. Guo, and Y. Li, "Recent advances in plasticized PVC gel for soft actuators and devices: A review," *Journal of Materials Chemistry C,* vol. 7, pp. 12991-13009, 11/14 2019.

[5] J. J. Huaroto, E. Suarez, H. I. Krebs, P. D. Marasco, and E. A. Vela, "A Soft Pneumatic Actuator as a Haptic Wearable Device for Upper Limb Amputees: Toward a Soft Robotic Liner," *IEEE Robotics and Automation Letters,* vol. 4, pp. 17-24, 2019.

[6] I. Kajiwara, S. Kitabatake, N. Hosoya, and S. Maeda, "Design of dielectric elastomer actuators for vibration control at high frequencies," *International Journal of Mechanical Sciences,* vol. 157-158, pp. 849-857, 2019/07/01/ 2019.

[7] E. R. Kandel, J. Koester, S. Mack, and S. Siegelbaum, *Principles of neural science*, Sixth ed. New York: McGraw Hill, 2021.

[8] S. Ebrahimi Takalloo, H. Seifi, and J. D. W. Madden, *Design of ultra-thin high frequency trilayer conducting polymer micro-actuators for tactile feedback interfaces* vol. 10163: SPIE, 2017.

[9] G. Spinks and G. Wallace, "Actuated Pins for Braille Displays," ed, 2009, pp. 265-277.

[10] G. Alici and N. N. Huynh, "Performance Quantification of Conducting Polymer Actuators for Real Applications: A Microgripping System," *IEEE/ASME Transactions on Mechatronics,* vol. 12, pp. 73-84, 2007.

[11] T. Shoa, J. D. Madden, N. R. Munce, and V. Yang, "Analytical modeling of a conducting polymer-driven catheter," *Polymer International,* vol. 59, pp. 343-351, 2010.

[12] A. Maziz, A. Concas, A. Khaldi, J. Stålhand, N.-K. Persson, and E. W. H. Jager, "Knitting and weaving artificial muscles," *Science Advances,* vol. 3, p. e1600327, 2017.

[13] B. Gupta, L. Zhang, A. Melvin, B. Goudeau, L. Bouffier, and A. Kuhn, "Designing Tubular Conducting Polymer Actuators for Wireless Electropumping," *Chemical Science,* vol. 12, 12/15 2020.

[14] M. Y. Coskun, C. Sancak, M. Itik, and G. Alici, "Hybrid force and position control of a conducting tri-layer electro-active polymer actuator," *Transactions of the Institute of Measurement and Control,* vol. 39, pp. 288-296, 2017/03/01 2016.

[15] K. Ikushima, S. John, A. Ono, and S. Nagamitsu, "PEDOT/PSS bending actuators for autofocus micro lens applications," *Synthetic Metals,* vol. 160, pp. 1877-1883, 2010/09/01/ 2010.

[16] S. McGovern, G. Alici, V.-T. Truong, and G. Spinks, "Finding NEMO (novel electromaterial muscle oscillator): a polypyrrole powered robotic fish with real-time

wireless speed and directional control," *Smart Material Structures,* vol. 18, p. 095009, September 01, 2009 2009.

[17] T. Goettsche and S. Haeberle, "Integrated Oral Drug Delivery System with Valve Based on Polypyrrole," ed, 2009, pp. 301-316.

[18] F. Hu, Y. Xue, J. Xu, and B. Lu, "PEDOT-Based Conducting Polymer Actuators," *Frontiers in Robotics and AI,* vol. 6, 2019-November-19 2019.

[19] M. Shi and E. M. Yeatman, "A comparative review of artificial muscles for microsystem applications," *Microsystems & Nanoengineering,* vol. 7, p. 95, 2021/11/23 2021.

[20] V. Woehling, G. T. M. Nguyen, C. Plesse, Y. Petel, Y. Dobashi, J. D. W. Madden*, et al.*, "Study of the piezoionic effect and influence of electrolyte in conducting polymer based soft strain sensors," *Multifunctional Materials,* vol. 2, p. 45002, 2019.

[21] G. Alici and M. J. Higgins, "Normal stiffness calibration of microfabricated tri-layer conducting polymer actuators," *Smart materials and structures,* vol. 18, p. 065013, 2009.

[22] G. Alici, A. Punning, and H. R. Shea, "Enhancement of actuation ability of ionic-type conducting polymer actuators using metal ion implantation," *Sensors and actuators. B, Chemical,* vol. 157, pp. 72-84, 2011.

[23] A. Maziz, C. Plesse, C. Soyer, C. Eric, and F. Vidal, "Demonstrating kHz Frequency Actuation for Conducting Polymer Microactuators," *Advanced Functional Materials,* vol. 24, 08/01 2014.

[24] R. H. Baughman, "Applications Of Conducting Polymers In Redox Devices And Intelligent Materials Systems," pp. 1785-1786.

[25] S. D. Deshpande, J. Kim, and S.-R. Yun, "New electro-active paper actuator using conducting polypyrrole: actuation behaviour in LiClO4 acetonitrile solution," *Synthetic Metals,* vol. 149, pp. 53-58, 2005/02/28/ 2005.

[26] G. Alici, "An effective modelling approach to estimate nonlinear bending behaviour of cantilever type conducting polymer actuators," *Sensors and Actuators B: Chemical,* vol. 141, pp. 284-292, 2009/08/18/ 2009.

[27] A. Fannir, C. Plesse, G. T. M. Nguyen, and F. Vidal, "Electro-interpenetration as tool for high strain trilayer conducting polymer actuator," *Smart materials and structures,* vol. 30, p. 025041, 2021.

[28] T. Shoa, J. D. Madden, C. W. E. Fok, and T. Mirfakhrai, "Rate Limits in Conducting Polymers," *Advances in Science and Technology,* vol. 61, pp. 26-33, 2009.

[29] T. Shoa, J. D. Madden, N. Fekri, N. R. Munce, and V. X. Yang, "Conducting polymer based active catheter for minimally invasive interventions inside arteries," *Annu Int Conf IEEE Eng Med Biol Soc,* vol. 2008, pp. 2063-6, 2008.

[30] T. Shoa, D. S. Yoo, K. Walus, and J. D. W. Madden, "A Dynamic Electromechanical Model for Electrochemically Driven Conducting Polymer Actuators," *IEEE/ASME Transactions on Mechatronics,* vol. 16, pp. 42-49, 2011.

[31] T. Mirfakhrai, J. D. W. Madden, and R. H. Baughman, "Polymer artificial muscles," *Materials Today,* vol. 10, pp. 30-38, 2007/04/01/ 2007.

[32] M. Farajollahi, V. Woehling, C. Plesse, G. T. M. Nguyen, F. Vidal, F. Sassani*, et al.*, "Self-contained tubular bending actuator driven by conducting polymers," *Sensors and Actuators A: Physical,* vol. 249, pp. 45-56, 2016/10/01/ 2016.

[33] B. Gaihre, G. Alici, G. Spinks, and J. Cairney, "Pushing the Limits for Microactuators Based on Electroactive Polymers," *Journal of Microelectromechanical Systems,* vol. 21, p. 574, 06/01 2012.

[34] D. Kongahage and J. Foroughi, "Actuator Materials: Review on Recent Advances and Future Outlook for Smart Textiles," *Fibers,* vol. 7, p. 21, 2019.

[35] J. D. W. Madden, "Conducting polymer actuators," PhD, Department of Mechanical Engineering, Massachusetts Institute of Technology, 2000.

[36] T. Shoa, "Engineering Aspects of Polypyrrole Actuators and their Application in Active Catheters," Doctor of Philosophy Doctor of Philosophy, Department of Electrical and Computer Engineering, The University of British Columbia, Vancouver, 2010.

[37] N. T. Nguyen, Y. Dobashi, C. Soyer, C. Plesse, G. T. M. Nguyen, F. Vidal*, et al.*, "Nonlinear dynamic modeling of ultrathin conducting polymer actuators including inertial effects," *Smart Materials and Structures,* vol. 27, p. 115032, 2018/10/25 2018.

[38] R. Temmer, A. Maziz, C. Plesse, A. Aabloo, F. Vidal, and T. Tamm, "In search of better electroactive polymer actuator materials: PPy versus PEDOT versus PEDOT–PPy composites," *Smart Materials and Structures,* vol. 22, p. 104006, 2013/09/19 2013.

[39] A. Simaite, B. Tondu, P. Souères, and C. Bergaud, "Hybrid PVDF/PVDF-graft-PEGMA Membranes for Improved Interface Strength and Lifetime of PEDOT:PSS/PVDF/Ionic Liquid Actuators," *ACS Applied Materials & Interfaces,* vol. 7, pp. 19966-19977, 2015/09/16 2015.

[40] I. Põldsalu, K. Rohtlaid, T. M. G. Nguyen, C. Plesse, F. Vidal, M. S. Khorram*, et al.*, "Thin ink-jet printed trilayer actuators composed of PEDOT:PSS on interpenetrating polymer

networks," *Sensors and Actuators B: Chemical,* vol. 258, pp. 1072-1079, 2018/04/01/ 2018.

[41] D. Zhou, G. Spinks, G. Wallace, C. Tiyapiboonchaiya, D. MacFarlane, M. Forsyth*, et al.*, "Solid state actuators based on polypyrrole and polymer-in-ionic liquid electrolytes," *Electrochimica Acta,* vol. 48, pp. 2355-2359, 06/01 2003.

[42] Y. Wu, G. Alici, G. Spinks, and G. Wallace, "Fast trilayer polypyrrole bending actuators for high speed applications," *Synthetic Metals,* vol. 156, pp. 1017-1022, 08/01 2006.

[43] S. W. John, G. Alici, and C. D. Cook, "Inversion-Based Feedforward Control of Polypyrrole Trilayer Bender Actuators," *IEEE/ASME Transactions on Mechatronics,* vol. 15, pp. 149-156, 2010.

[44] R. Minato, G. Alici, S. McGovern, and G. Spinks, *Tri-layer conducting polymer actuators with variable dimensions* vol. 6524: SPIE, 2007.

[45] B. Gaihre, G. Alici, G. M. Spinks, and J. M. Cairney, "Effect of electrolyte storage layer on performance of PPy-PVDF-PPy microactuators," *Sensors and Actuators B: Chemical,* vol. 155, pp. 810-816, 2011/07/20/ 2011.

[46] N. Festin, A. Maziz, C. Plesse, D. Teyssié, C. Chevrot, and F. Vidal, "Robust solid polymer electrolyte for conducting IPN actuators," *Smart Materials and Structures,* vol. 22, p. 104005, 2013/09/19 2013.

[47] U. Lang, N. Naujoks, and J. Dual, "Mechanical characterization of PEDOT:PSS thin films," *Synthetic Metals,* vol. 159, pp. 473-479, 2009/03/01/ 2009.

[48] A. Maziz, C. Plesse, C. Soyer, E. Cattan, and F. Vidal, "High speed electromechanical response of ionic microactuators," pp. 94300O-94300O-8.

[49] B. Cho, K. S. Park, J. Baek, H. S. Oh, Y.-E. Koo Lee, and M. M. Sung, "Single-Crystal Poly(3,4-ethylenedioxythiophene) Nanowires with Ultrahigh Conductivity," *Nano Letters,* vol. 14, pp. 3321-3327, 2014/06/11 2014.

[50] Y. W. Park, A. J. Heeger, M. A. Druy, and A. G. MacDiarmid, "Electrical transport in doped polyacetylene," *The Journal of chemical physics,* vol. 73, pp. 946-957, 1980.

[51] Y. W. Park, C. Park, Y. S. Lee, C. O. Yoon, H. Shirakawa, Y. Suezaki*, et al.*, "Electrical conductivity of highly-oriented-polyacetylene," *Solid State Communications,* vol. 65, pp. 147-150, 1988/01/01/ 1988.

[52] F. Jonas and J. T. Morrison, "3,4-polyethylenedioxythiophene (PEDT): Conductive coatings technical applications and properties," *Synthetic Metals,* vol. 85, pp. 1397-1398, 1997/03/15/ 1997.

[53] M. N. Gueye, A. Carella, J. Faure-Vincent, R. Demadrille, and J.-P. Simonato, "Progress in understanding structure and transport properties of PEDOT-based materials: A critical review," *Progress in Materials Science,* vol. 108, p. 100616, 2020/02/01/ 2020.

[54] G. Heywang and F. Jonas, "Poly(alkylenedioxythiophene)s—new, very stable conducting polymers," *Advanced Materials,* vol. 4, pp. 116-118, 1992.

[55] Y. Xu, Y. Jia, P. Liu, Q. Jiang, D. Hu, and Y. Ma, "Poly(3,4-ethylenedioxythiophene) (PEDOT) as Promising Thermoelectric Materials and Devices," *Chemical Engineering Journal,* vol. 404, p. 126552, 2021.

[56] S. K. M. Jönsson, J. Birgerson, X. Crispin, G. Greczynski, W. Osikowicz, A. W. Denier van der Gon*, et al.*, "The effects of solvents on the morphology and sheet resistance in poly(3,4-ethylenedioxythiophene)–polystyrenesulfonic acid (PEDOT–PSS) films," *Synthetic Metals,* vol. 139, pp. 1-10, 2003/08/08/ 2003.

[57] N. P. S. Chauhan, S. Jadoun, B. S. Rathore, M. Barani, and P. Zarrintaj, "Redox polymers for capacitive energy storage applications," *Journal of Energy Storage,* vol. 43, p. 103218, 2021/11/01/ 2021.

[58] H. Shi, C. Liu, Q. Jiang, and J. Xu, "Effective Approaches to Improve the Electrical Conductivity of PEDOT:PSS: A Review," *Advanced Electronic Materials,* vol. 1, p. 1500017, 2015.

[59] S. R. S. Kumar, N. Kurra, and H. N. Alshareef, "Enhanced high temperature thermoelectric response of sulphuric acid treated conducting polymer thin films," *Journal of Materials Chemistry C,* vol. 4, pp. 215-221, 2016.

[60] H. Machrafi, I. Bobinac, P. Dongo, V. Gallo, F. Iermano, and C. S. Iorio, "Chemical stability and reversibility of PEDOT:PSS electrodes in view of low-cost biocompatible cellulose-assisted biosensors," *Materials Today Communications,* vol. 27, p. 102437, 2021/06/01/ 2021.

[61] L. Ouyang, C. Musumeci, M. J. Jafari, T. Ederth, and O. Inganäs, "Imaging the Phase Separation Between PEDOT and Polyelectrolytes During Processing of Highly Conductive PEDOT:PSS Films," *ACS Applied Materials & Interfaces,* vol. 7, pp. 19764-19773, 2015/09/09 2015.

[62] N. Kim, S. Kee, S. H. Lee, B. H. Lee, Y. H. Kahng, Y.-R. Jo*, et al.*, "Highly Conductive PEDOT:PSS Nanofibrils Induced by Solution-Processed Crystallization," *Advanced Materials,* vol. 26, pp. 2268-2272, 2014.

[63] A. G. MacDiarmid and A. J. Epstein, "The concept of secondary doping as applied to polyaniline," *Synthetic Metals,* vol. 65, pp. 103-116, 1994/08/01/ 1994.

[64] J. Y. Kim, J. H. Jung, D. E. Lee, and J. Joo, "Enhancement of electrical conductivity of poly(3,4-ethylenedioxythiophene)/poly(4-styrenesulfonate) by a change of solvents," *Synthetic Metals,* vol. 126, pp. 311-316, 2002/02/14/ 2002.

[65] X. Wang, X. Zhang, L. Sun, D. Lee, S. Lee, M. Wang*, et al.*, "High electrical conductivity and carrier mobility in oCVD PEDOT thin films by engineered crystallization and acid treatment," *Science Advances,* vol. 4, p. eaat5780, 2018.

[66] J. Huang, P. F. Miller, J. C. de Mello, A. J. de Mello, and D. D. C. Bradley, "Influence of thermal treatment on the conductivity and morphology of PEDOT/PSS films," *Synthetic Metals,* vol. 139, pp. 569-572, 2003/10/09/ 2003.

[67] Y.-J. Lin, F.-M. Yang, C.-Y. Huang, W.-Y. Chou, J. Chang, and Y.-C. Lien, "Increasing the work function of poly(3,4-ethylenedioxythiophene) doped with poly(4-styrenesulfonate) by ultraviolet irradiation," *Applied Physics Letters,* vol. 91, p. 092127, 08/29 2007.

[68] A. Moujoud, S. H. Oh, H. S. Shin, and H. J. Kim, "On the mechanism of conductivity enhancement and work function control in PEDOT:PSS film through UV-light treatment," *physica status solidi (a),* vol. 207, pp. 1704-1707, 2010.

[69] Y. Shi, Y. Zhou, R. Shen, F. Liu, and Y. Zhou, "Solution-based synthesis of PEDOT:PSS films with electrical conductivity over 6300 S/cm," *Journal of Industrial and Engineering Chemistry,* vol. 101, pp. 414-422, 2021/09/25/ 2021.

[70] J. Luo, D. Billep, T. Waechtler, T. Otto, M. Toader, O. Gordan*, et al.*, "Enhancement of the thermoelectric properties of PEDOT:PSS thin films by post-treatment," *Journal of Materials Chemistry A,* vol. 1, pp. 7576-7583, 2013.

[71] N. K. Unsworth, I. Hancox, C. Argent Dearden, P. Sullivan, M. Walker, R. S. Lilley*, et al.*, "Comparison of dimethyl sulfoxide treated highly conductive poly(3,4-ethylenedioxythiophene):poly(styrenesulfonate) electrodes for use in indium tin oxide-free organic electronic photovoltaic devices," *Organic Electronics,* vol. 15, pp. 2624-2631, 2014/10/01/ 2014.

[72] D. Alemu, H.-Y. Wei, K.-C. Ho, and C.-W. Chu, "Highly conductive PEDOT:PSS electrode by simple film treatment with methanol for ITO-free polymer solar cells," *Energy & environmental science,* vol. 5, pp. 9662-9671, 2012.

[73] F. Ely, A. Matsumoto, B. Zoetebier, V. S. Peressinotto, M. K. Hirata, D. A. de Sousa*, et al.*, "Handheld and automated ultrasonic spray deposition of conductive PEDOT:PSS films and their application in AC EL devices," *Organic Electronics,* vol. 15, pp. 1062-1070, 2014/05/01/ 2014.

[74] N. Sankir, "Selective deposition of PEDOT/PSS on to flexible substrates and tailoring the electrical resistivity by post treatment," *Circuit World,* vol. 34, pp. 32-37, 11/21 2008.

[75] J. Ouyang, Q. Xu, C.-W. Chu, Y. Yang, G. Li, and J. Shinar, "On the mechanism of conductivity enhancement in poly(3,4-ethylenedioxythiophene):poly(styrene sulfonate) film through solvent treatment," *Polymer,* vol. 45, pp. 8443-8450, 2004/11/01/ 2004.

[76] N. K. Unsworth, I. Hancox, C. A. Dearden, P. Sullivan, M. Walker, R. S. Lilley*, et al.*, "Comparison of dimethyl sulfoxide treated highly conductive poly electrodes for use in indium tin oxide-free organic electronic photovoltaic devices," *Organic electronics,* vol. 15, p. 2624, 2014.

[77] D. A. Mengistie, H.-Y. Wei, K.-C. Ho, and C. W. Chu, "Highly conductive PEDOT:PSS electrode by simple film treatment with methanol for ITO-free polymer solar cells," *Energy Environ. Sci.,* vol. 5, pp. 9662-9671, 10/18 2012.

[78] A. M. Nardes, R. A. J. Janssen, and M. Kemerink, "A Morphological Model for the Solvent-Enhanced Conductivity of PEDOT:PSS Thin Films," *Advanced Functional Materials,* vol. 18, pp. 865-871, 2008.

[79] X. Crispin, F. L. E. Jakobsson, A. Crispin, P. C. M. Grim, P. Andersson, A. Volodin*, et al.*, "The Origin of the High Conductivity of Poly(3,4-ethylenedioxythiophene)−Poly(styrenesulfonate) (PEDOT−PSS) Plastic Electrodes," *Chemistry of Materials,* vol. 18, pp. 4354-4360, 2006/09/01 2006.

[80] Y. He, B. Zhu, and Y. Inoue, "Hydrogen bonds in polymer blends," *Progress in Polymer Science,* vol. 29, pp. 1021-1051, 2004/10/01/ 2004.

[81] C. M. Palumbiny, F. Liu, T. P. Russell, A. Hexemer, C. Wang, and P. Müller-Buschbaum, "The Crystallization of PEDOT:PSS Polymeric Electrodes Probed In Situ during Printing," *Advanced materials (Weinheim),* vol. 27, pp. 3391-3397, 2015.

[82] K. Pattanarat, N. Petchsang, T. Osotchan, Y.-H. Kim, and R. Jaisutti, "Wash-Durable Conductive Yarn with Ethylene Glycol-Treated PEDOT:PSS for Wearable Electric Heaters," *ACS Applied Materials & Interfaces,* vol. 13, pp. 48053-48060, 2021/10/13 2021.

[83] A. L. Oechsle, J. E. Heger, N. Li, S. Yin, S. Bernstorff, and P. Müller-Buschbaum, "Correlation of Thermoelectric Performance, Domain Morphology and Doping Level in PEDOT:PSS Thin Films Post-Treated with Ionic Liquids," *Macromol Rapid Commun,* vol. 42, p. e2100397, Oct 2021.

[84] J. Atoyo, M. R. Burton, J. McGettrick, and M. J. Carnie, "Enhanced Electrical Conductivity and Seebeck Coefficient in PEDOT:PSS via a Two-Step Ionic liquid and NaBH4 Treatment for Organic Thermoelectrics," *Polymers,* vol. 12, p. 559, 2020.

[85] S. K. Lee and K. K. Lee, "Conductivity Enhancement of PEDOT/PSS Films with Ionic Liquids as Dopants," *Advanced materials research,* vol. 93-94, pp. 501-504, 2010.

[86] A. de Izarra, S. Park, J. Lee, Y. Lansac, and Y. H. Jang, "Ionic Liquid Designed for PEDOT:PSS Conductivity Enhancement," *Journal of the American Chemical Society,* vol. 140, pp. 5375-5384, 2018/04/25 2018.

[87] M. Y. Teo, N. Kim, S. Kee, B. S. Kim, G. Kim, S. Hong*, et al.*, "Highly Stretchable and Highly Conductive PEDOT:PSS/Ionic Liquid Composite Transparent Electrodes for Solution-Processed Stretchable Electronics," *ACS Applied Materials & Interfaces,* vol. 9, pp. 819-826, 2017/01/11 2017.

[88] J. Luo, D. Billep, T. Waechtler, T. Otto, M. Toader, O. Gordan*, et al.*, "Enhancement of the thermoelectric properties of PEDOT:PSS thin films by post-treatment," *Journal of Materials Chemistry A,* 06/11 2013.

[89] Y. Xia and J. Ouyang, "Significant Conductivity Enhancement of Conductive Poly(3,4-ethylenedioxythiophene): Poly(styrenesulfonate) Films through a Treatment with Organic Carboxylic Acids and Inorganic Acids," *ACS Applied Materials & Interfaces,* vol. 2, pp. 474-483, 2010/02/24 2010.

[90] K. Rohtlaid, G. T. M. Nguyen, C. Soyer, E. Cattan, F. Vidal, and C. Plesse, "Poly(3,4-ethylenedioxythiophene):Poly(styrene sulfonate)/Polyethylene Oxide Electrodes with Improved Electrical and Electrochemical Properties for Soft Microactuators and Microsensors," *Advanced Electronic Materials,* vol. 5, p. 1800948, 2019.

[91] "CRC handbook of chemistry and physics," 1977.

[92] S. Zhang, P. Kumar, A. S. Nouas, L. Fontaine, H. Tang, and F. Cicoira, "Solvent-induced changes in PEDOT:PSS films for organic electrochemical transistors," *APL Materials,* vol. 3, p. 014911, 2015.

[93] J. Lin, Y. Liu, and Q. M. Zhang, "Charge dynamics and bending actuation in Aquivion membrane swelled with ionic liquids," *Polymer,* vol. 52, pp. 540-546, 2011/01/21/ 2011.

[94] K. Rohtlaid, G. Nguyen, C. Soyer, C. Eric, F. Vidal, and C. Plesse, "Poly(3,4-ethylenedioxythiophene):Poly(styrene sulfonate)/Polyethylene Oxide Electrodes with Improved Electrical and Electrochemical Properties for Soft Microactuators and Microsensors," *Advanced Electronic Materials,* vol. 5, 03/01 2019.

[95] T. N. Nguyen, K. Rohtlaid, C. Plesse, G. T. M. Nguyen, C. Soyer, S. Grondel*, et al.*, "Ultrathin electrochemically driven conducting polymer actuators: fabrication and electrochemomechanical characterization," *Electrochimica Acta,* vol. 265, pp. 670-680, 2018/03/01/ 2018.

[96] M. Döbbelin, R. Marcilla, C. Tollan, J. A. Pomposo, J.-R. Sarasua, and D. Mecerreyes, "A new approach to hydrophobic and water-resistant poly(3,4-ethylenedioxythiophene):poly(styrenesulfonate) films using ionic liquids," *Journal of materials chemistry,* vol. 18, pp. 5354-5358, 2008.

[97] K. O. Oyedotun, T. M. Masikhwa, S. Lindberg, A. Matic, P. Johansson, and N. Manyala, "Comparison of ionic liquid electrolyte to aqueous electrolytes on carbon nanofibres supercapacitor electrode derived from oxygen-functionalized graphene," *Chemical Engineering Journal,* vol. 375, p. 121906, 2019/11/01/ 2019.

[98] S. Naficy, N. Stoboi, P. G. Whitten, G. M. Spinks, and G. G. Wallace, "Evaluation of encapsulating coatings on the performance of polypyrrole actuators," *Smart Materials and Structures,* vol. 22, p. 075005, 2013/05/28 2013.

[99] A. Maziz, C. Plesse, C. Soyer, E. Cattan, and F. Vidal, "Top-down Approach for the Direct Synthesis, Patterning, and Operation of Artificial Micromuscles on Flexible Substrates," *ACS Applied Materials & Interfaces,* vol. 8, pp. 1559-1564, 2016/01/27 2016.

[100] Y. Dobashi, A. Fannir, M. Farajollahi, A. Mahmoudzadeh, A. Usgaocar, D. Yao*, et al.*, "Ion Transport in Polymer Composites with Non-Uniform Distributions of Electronic Conductors," *Electrochimica acta,* vol. 247, pp. 149-162, 2017.

[101] J. H. Cho, J. Lee, Y. He, B. S. Kim, T. P. Lodge, and C. D. Frisbie, "High-Capacitance Ion Gel Gate Dielectrics with Faster Polarization Response Times for Organic Thin Film Transistors," *Advanced materials (Weinheim),* vol. 20, pp. 686-690, 2008.

[102] M. Ishikawa, T. Sugimoto, M. Kikuta, E. Ishiko, and M. Kono, "Pure ionic liquid electrolytes compatible with a graphitized carbon negative electrode in rechargeable lithium-ion batteries," *Journal of power sources,* vol. 162, pp. 658-662, 2006.

[103] H. Tokuda, K. Hayamizu, K. Ishii, M. A. B. H. Susan, and M. Watanabe, "Physicochemical Properties and Structures of Room Temperature Ionic Liquids. 2. Variation of Alkyl Chain Length in Imidazolium Cation," *The Journal of Physical Chemistry B,* vol. 109, pp. 6103-6110, 2005/04/01 2005.

[104] N. Abdullayeva and M. Sankir, "Influence of Electrical and Ionic Conductivities of Organic Electronic Ion Pump on Acetylcholine Exchange Performance," *Materials (Basel, Switzerland),* vol. 10, p. 586, 2017.

[105] Y. Liu, B. Weng, J. M. Razal, Q. Xu, C. Zhao, Y. Hou*, et al.*, "High-Performance Flexible All-Solid-State Supercapacitor from Large Free-Standing Graphene-PEDOT/PSS Films," *Scientific reports,* vol. 5, pp. 17045-17045, 2015.

[106] J. Rivnay, P. Leleux, M. Ferro, M. Sessolo, A. Williamson, D. A. Koutsouras*, et al.*, "High-performance transistors for bioelectronics through tuning of channel thickness," *Science advances,* vol. 1, pp. e1400251-e1400251, 2015.

[107] G. Greczynski and L. Hultman, "X-ray photoelectron spectroscopy: Towards reliable binding energy referencing," *Progress in Materials Science,* vol. 107, p. 100591, 2020/01/01/ 2020.

[108] F. Moulder John, *Handbook of x-ray photoelectron spectroscopy : a reference book of standard spectra for identification and interpretation of XPS data*: Eden Prairie, Minn. : Physical Electronics, [1995] ©1995, 1995.

[109] S. Tougaard, "Quantitative analysis of the inelastic background in surface electron spectroscopy," *Surface and Interface Analysis,* vol. 11, pp. 453-472, 1988.

[110] G. Beamson and D. R. Briggs, "High Resolution XPS of Organic Polymers: The Scienta ESCA300 Database," 1992.

[111] D. A. Shirley, "High-Resolution X-Ray Photoemission Spectrum of the Valence Bands of Gold," *Physical Review B,* vol. 5, pp. 4709-4714, 06/15/ 1972.

[112] S. Tougaard, "Practical algorithm for background subtraction," *Surface Science,* vol. 216, pp. 343-360, 1989/06/02/ 1989.

[113] A. Herrera-Gomez, M. Bravo-Sanchez, O. Ceballos-Sanchez, and M. O. Vazquez-Lepe, "Practical methods for background subtraction in photoemission spectra," *Surface and Interface Analysis,* vol. 46, pp. 897-905, 2014.

[114] A. V. Lubenchenko, D. A. Ivanov, and D. S. Lukiantsev, "Application of MatLab for Processing X-ray Photoelectron Spectroscopy Spectra," in *2020 V International Conference on Information Technologies in Engineering Education (Inforino)*, 2020, pp. 1-4.

[115] J. Végh, "The analytical form of the Shirley-type background," *Journal of Electron Spectroscopy and Related Phenomena,* vol. 46, pp. 411-417, 1988/01/01/ 1988.

[116] A. Lubenchenko, O. I. Lubenchenko, D. A. Ivanov, and I. V. Ivanova, *Application of MatLab for Solid Surface Analysis by Means of X-Ray Photoelectron Spectroscopy*, 2018.

[117] Y. Wu, G. Alici, G. M. Spinks, and G. G. Wallace, "Fast trilayer polypyrrole bending actuators for high speed applications," *Synthetic Metals,* vol. 156, pp. 1017-1022, 2006/08/01/ 2006.

[118] S. John, G. Alici, and C. Cook, "Validation of Resonant Frequency Model for Polypyrrole Trilayer Actuators," *Mechatronics, IEEE/ASME Transactions on,* vol. 13, pp. 401-409, 09/01 2008.

[119] G. Alici, V. Devaud, P. Renaud, and G. Spinks, "Conducting polymer microactuators operating in air," *J. Micromech. Microeng.,* vol. 19, 02/01 2009.

[120] S. John, G. Alici, and C. Cook, *Frequency response of polypyrrole trilayer actuator displacement* vol. 6927: SPIE, 2008.

[121] I. Põldsalu, M. Harjo, T. Tamm, M. Uibu, A.-L. Peikolainen, and R. Kiefer, "Inkjet-printed hybrid conducting polymer-activated carbon aerogel linear actuators driven in an organic electrolyte," *Sensors and Actuators B: Chemical,* vol. 250, pp. 44-51, 2017/10/01/ 2017.

[122] E. P. Randviir and C. E. Banks, "Electrochemical impedance spectroscopy: an overview of bioanalytical applications," *Analytical methods,* vol. 5, p. 1098, 2013.

[123] N. O. Laschuk, E. B. Easton, and O. V. Zenkina, "Reducing the resistance for the use of electrochemical impedance spectroscopy analysis in materials chemistry," *RSC advances,* vol. 11, pp. 27925-27936, 2021.

[124] C. H. Nguyen, G. Alici, and G. G. Wallace, "Modelling trilayer conjugated polymer actuators for their sensorless position control," *Sensors and Actuators A: Physical,* vol. 185, pp. 82-91, 2012/10/01/ 2012.

[125] A. A. Amiri Moghadam, W. Hong, A. Kouzani, A. Kaynak, R. Zamani, and R. Montazami, "Nonlinear Dynamic Modeling of Ionic Polymer Conductive Network Composite Actuators Using Rigid Finite Element Method," *Sensors and Actuators A Physical,* vol. 217, 09/01 2014.

[126] Y. H. Jung, J.-H. Kim, and J. A. Rogers, "Skin-Integrated Vibrohaptic Interfaces for Virtual and Augmented Reality," *Advanced Functional Materials,* vol. n/a, p. 2008805.

[127] S. Choi and K. J. Kuchenbecker, "Vibrotactile Display: Perception, Technology, and Applications," *Proceedings of the IEEE,* vol. 101, pp. 2093-2104, 2013.

[128] C. Basdogan, F. Giraud, V. Levesque, and S. Choi, "A Review of Surface Haptics: Enabling Tactile Effects on Touch Surfaces," *IEEE Trans Haptics,* vol. 13, pp. 450-470, Jul-Sep 2020.

[129] J. Yin, R. Hinchet, H. Shea, and C. Majidi, "Wearable Soft Technologies for Haptic Sensing and Feedback," *Advanced Functional Materials,* vol. 31, p. 2007428, 2021.

[130] C. Hatzfeld, T. A. Kern, SpringerLink, and L. e. C. S. Springer, *Engineering Haptic Devices: A Beginner's Guide*, 2nd 2014. ed. London: Springer London, 2014.

[131] J. C. Quindlen, H. K. Stolarski, M. D. Johnson, and V. H. Barocas, "A multiphysics model of the Pacinian corpuscle," *Integr Biol (Camb),* vol. 8, pp. 1111-1125, Nov 7 2016.

[132] S. R. Williams and A. M. Okamura, "Body-Mounted Vibrotactile Stimuli: Simultaneous Display of Taps on the Fingertips and Forearm," *IEEE Trans Haptics,* vol. 14, pp. 432-444, Apr-Jun 2021.

[133] E. P. Gardner and J. H. Martin, "Coding of Sensory Information," 2010.

[134] C. Hatzfeld, "Haptics as an Interaction Modality," in *Engineering Haptic Devices: A Beginner's Guide*, C. Hatzfeld and T. A. Kern, Eds., ed London: Springer London, 2014, pp. 29-100.

[135] J. S. Schofield, M. R. Dawson, J. P. Carey, and J. S. Hebert, "Characterizing the effects of amplitude, frequency and limb position on vibration induced movement illusions: Implications in sensory-motor rehabilitation," *Technol Health Care,* vol. 23, pp. 129-41, 2015.

[136] P. D. Marasco, J. S. Hebert, J. W. Sensinger, C. E. Shell, J. S. Schofield, Z. C. Thumser*, et al.*, "Illusory movement perception improves motor control for prosthetic hands," *Sci Transl Med,* vol. 10, Mar 14 2018.

[137] J. S. Schofield, "Engineering Kinesthetic Perceptions: The Restoration of Movement Sense in Upper Limb Prosthetic Use," Doctor of Philosophy Doctor of Philosophy, Department of Mechanical Engineering, University of Alberta, 2017.

[138] S. J. J. Bolanowski, G. A. Gescheider, R. T. Verrillo, and C. M. Checkosky, "Four channels mediate the mechanical aspects of touch," *The Journal of the Acoustical Society of America,* vol. 84, pp. 1680-1694, 1988.

[139] M. Wiertlewski and V. Hayward, "Mechanical behavior of the fingertip in the range of frequencies and displacements relevant to touch," *J Biomech,* vol. 45, pp. 1869-74, Jul 26 2012.

[140] W. McMahan and K. J. Kuchenbecker, "Dynamic modeling and control of voice-coil actuators for high-fidelity display of haptic vibrations," in *2014 IEEE Haptics Symposium (HAPTICS)*, 2014, pp. 115-122.

[141] S. Gao, S. Yan, H. Zhao, and A. Nathan, "Haptic Feedback," in *Touch-Based Human-Machine Interaction: Principles and Applications*, ed Cham: Springer International Publishing, 2021, pp. 91-108.

[142] P. Olsson, F. Nysjo, I. B. Carlbom, and S. Johansson, "Comparison of Walking and Traveling-Wave Piezoelectric Motors as Actuators in Kinesthetic Haptic Devices," *IEEE Trans Haptics,* vol. 9, pp. 427-31, Jul-Sep 2016.

[143] T. Delhaye, C. Ge, L. Francis, E. Cretu, and D. Flandre, "One-Day Fast-Prototyping Process for Functionalized Membrane Array on Flexible Substrate," in *45th International Conference on Micro & Nano Engineering*, Rhodes, Greece, 2019.

[144] A. Kalra and A. Lowe, "An Overview of Factors Affecting the Skins Youngs Modulus," *Journal of Aging Science,* vol. 4, 01/01 2016.

[145] D. A. Hall, "The ageing of connective tissue," *Exp Gerontol,* vol. 3, pp. 77-89, Aug 1968.

[146] A. C. Park and C. B. Baddiel, "Rheology of stratum corneum--I: A molecular interpretation of the stress-strain curve," 1972.

[147] R. M. Peters, E. Hackeman, and D. Goldreich, "Diminutive digits discern delicate details: fingertip size and the sex difference in tactile spatial acuity," *The Journal of neuroscience : the official journal of the Society for Neuroscience,* vol. 29, pp. 15756-15761, 2009.

[148] F. Hik, E. Taatizadeh, S. Ebrahimi Takalloo, and J. Madden, *The effects of improved conductivity on actuation* vol. 12042: SPIE, 2022.

[149] A. Dementyev, P. Getreuer, D. Kanevsky, M. Slaney, and R. F. Lyon, "VHP: Vibrotactile Haptics Platform for On-body Applications," presented at the The 34th Annual ACM Symposium on User Interface Software and Technology, Virtual Event, USA, 2021.

[150] S. Goodman, S. Kirchner, R. Guttman, D. Jain, J. Froehlich, and L. Findlater, "Evaluating Smartwatch-based Sound Feedback for Deaf and Hard-of-hearing Users Across Contexts," pp. 1-13.

[151] G. Flores, S. Kurniawan, R. Manduchi, E. Martinson, L. M. Morales, and E. A. Sisbot, "Vibrotactile Guidance for Wayfinding of Blind Walkers," *IEEE Transactions on Haptics,* vol. 8, pp. 306-317, 2015.

[152] S. Mann, J. Huang, R. Janzen, R. Lo, V. Rampersad, A. Chen*, et al.*, "Blind navigation with a wearable range camera and vibrotactile helmet," pp. 1325-1328.

[153] J. Kangas, J. Rantala, and R. Raisamo, "Gaze Cueing with a Vibrotactile Headband for a Visual Search Task," *Augmented human research,* vol. 2, pp. 1-12, 2017.

[154] Y. Kato, T. Sekitani, M. Takamiya, M. Doi, K. Asaka, T. Sakurai*, et al.*, "Sheet-Type Braille Displays by Integrating Organic Field-Effect Transistors and Polymeric Actuators," *IEEE Transactions on Electron Devices,* vol. 54, pp. 202-209, 2007.

[155] Y. Bar-Cohen, "Electroactive polymers for refreshable Braille displays," *SPIE newsroom,* 2009.

[156] C. R. Wagner, N. Stylopoulos, and R. D. Howe, "The role of force feedback in surgery: analysis of blunt dissection," in *Proceedings 10th Symposium on Haptic Interfaces for Virtual Environment and Teleoperator Systems. HAPTICS 2002*, 2002, pp. 68-74.

[157] A. Abiri, J. Pensa, A. Tao, J. Ma, Y.-Y. Juo, S. J. Askari*, et al.*, "Multi-Modal Haptic Feedback for Grip Force Reduction in Robotic Surgery," *Scientific Reports,* vol. 9, p. 5016, 2019/03/21 2019.

[158] J. S. Schofield, K. R. Evans, J. P. Carey, and J. S. Hebert, "Applications of sensory feedback in motorized upper extremity prosthesis: a review," *Expert review of medical devices* vol. 11, p. 499, 2014.

[159] S. M. Engdahl, B. P. Christie, B. Kelly, A. Davis, C. A. Chestek, and D. H. Gates, "Surveying the interest of individuals with upper limb loss in novel prosthetic control techniques," *Journal of NeuroEngineering and Rehabilitation,* vol. 12, 2015/06/13/ // 2015.

[160] P. F. Pasquina, B. N. Perry, M. E. Miller, G. S. F. Ling, and J. W. Tsao, "Recent advances in bioelectric prostheses," *Neurology. Clinical practice,* vol. 5, pp. 164-170, 2015.

[161] U. Wijk, P. Svensson, C. Antfolk, I. K. Carlsson, A. Björkman, and B. Rosén, "Touch on predefined areas on the forearm can be associated with specific fingers: Towards a new principle for sensory feedback in hand prostheses," *J Rehabil Med,* vol. 51, pp. 209-216, Mar 13 2019.

[162] M. D. Rinderknecht, Y. Kim, L. Santos-Carreras, H. Bleuler, and R. Gassert, "Combined tendon vibration and virtual reality for post-stroke hand rehabilitation," in *2013 World Haptics Conference (WHC)*, 2013, pp. 277-282.

[163] B. Stephens-Fripp, G. Alici, and R. Mutlu, "A Review of Non-Invasive Sensory Feedback Methods for Transradial Prosthetic Hands," *IEEE Access,* vol. 6, pp. 6878-6899, 2018.

[164] G. Pirouzi, N. A. Abu Osman, A. Eshraghi, S. Ali, H. Gholizadeh, and W. A. Wan Abas, "Review of the socket design and interface pressure measurement for transtibial prosthesis," *ScientificWorldJournal,* vol. 2014, p. 849073, 2014.

[165] S. Ebrahimi Takalloo, A. Fannir, G. T. M. Nguyen, C. Plesse, F. Vidal, and J. D. W. Madden, "Impermeable and Compliant: SIBS as a Promising Encapsulant for Ionically Electroactive Devices," *Robotics,* vol. 8, p. 60, 2019.

[166] Farajollahi, M., S. Ebrahimi Takallo, V. Woehling, A. Fannir, C. Plesse, F. Vidal, F. Sassani and J. D. Madden, (2015). "Stacking trilayers to increase force generation," Proc. *SPIE*, vol. 9430, 2015.

Appendices

Appendix A : Tri-Layer Actuator Literature Review Supplemental Information

In Appendix A we present additional supplementary results on details from the conducting polymer tri-layer actuator literature review described in Section 1.6.

Table A-1 Key parameters of conducting polymer tri-layer actuators published up to August 2020.

Reference	CP Layer	Separator Layer	L, L' (mm)	W (mm)	h_p (µm)	h_g (µm)	F_B (mN)	$2D$ (mm)	f_c (Hz)
Nguyen *et al.* (2018)	PEDOT	PEO:NBR	6	1	3.4	11.5	0.011	8.4	0.2
Maziz *et al.* (2015)	PEDOT	PEO:NBR	0.16	0.03	1.3	3.4	0.0026	0.05	0.3
Maziz *et al.* (2014)	PEDOT	PEO:NBR	0.69	0.045	1.3	3.4	0.0015	0.121	40
Maziz *et al.* (2014)	PEDOT	PEO:NBR	0.69	0.045	2.2	7.6	0.0045	0.178	10
Maziz *et al.* (2014)	PEDOT	PEO:NBR	0.69	0.045	3	13	0.0052	0.18	15
Temmer *et al.* (2013)	PEDOT/PEDOT	PVDF	20, 5	4	6.5	110	2	0.12	0.5
Okuzaki *et al.* (2014)	PEDOT:PSS	IL/PU	15	5	14	100	2.18	7.6	0.5
Ebrahimi T. (2019)	PEDOT:PSS	PVDF	10.5, 10	2	3.5	125	0.64	4.35	2.2
Gaihre *et al.* (2012)	PPy	PVDF	0.85	0.25	8	110	0.033	0.8	0.05
Gaihre *et al.* (2012)	PPy	PVDF	0.85	0.25	8	32	0.52	0.074	0.05
Gaihre *et al.* (2012)	PPy	PVDF	0.2	0.05	8	32	0.468	0.25	0.09
Gaihre *et al.* (2012)	PPy	PVDF	0.85	0.25	11	32	0.12	0.17	0.05
Gaihre *et al.* (2011)	PPy	PVDF	0.85	0.25	11	32	0.1	0.146	0.01
Gaihre *et al.* (2011)	PPy	PVDF	0.85	0.25	11	110	0.49	0.053	0.05
John *et al.* (2008)	PPy	PVDF	10, 9.5	2	25	110	0.62	7.1	0.2
Alici *et al.* (2007)	PPy	PVDF	5	1	30	110	1.1	8	0.1
Temmer *et al.* (2013)	PPy/PPy	PVDF	20, 5	4	17	110	2.5	1.65	0.7
Temmer *et al.* (2013)	PEDOT/PPy	PVDF	20, 5	4	6.35	110	4	0.42	0.5
Temmer *et al.* (2013)	PPy PEDOT	PVDF	20, 5	4	13.8	110	1.5	0.5	2

Appendix B : Standard Operating Procedures

Appendix B includes the standard operating procedures for spray coating (Section 2.1.2.1) and actuation frequency response measurements (Section 3.2.1)

B.1 Spray Coating SOP

B.1.1 Summary of Fabrication Steps

1. Add 5% DMSO by volume to aqueously dispersed PEDOT:PSS solution and stir vigorously for at least 15 minutes.
2. Load PEDOT:PSS solution into 25 mL syringe.
3. Fix a 6 cm x 6 cm PVDF membrane on the spray coating substrate using an aluminum frame with dimensions of 5 cm x 5 cm.
4. Set the substrate temperature to 130°C to facilitate water evaporation and prevent PEDOT:PSS from diffusing into the PVDF bulk.
5. Spray *n* number of successive PEDOT:PSS coats on the two sides of the PVDF membrane.

*Adapt this procedure as need to for conducting polymer and substrate materials and/or thickness of films.

B.1.2 Spray Coater Settings

- Nozzle to substrate distance = 9 cm
- Nozzle speed = 20 mm/s
- Shaping air pressure = 4 PSIG
- Flow rate = 0.13 mL/min
- Spacing of serpent path = 2 mm

B.1.3 Experimental Procedure

Solution Preparation

These steps describe the procedure for preparing 20 mL of 5%(v/v) DMSO to PEDOT:PSS aqueous solution.

1. Pipet 1mL of DMSO into 19mL of PEDOT:PSS
2. Stir for at least 15 minutes

Start-up

1. Turn red dial to “on” on the side of the spray coater.
2. Switch on manual syringe control screen.
3. Turn on computer and open ExactaCoat program (in this sequential order).
4. Ensure PEDOT tubes are connected to correct ports as shown in Figure B-1. Ensure the small white rubber seals are inside connections when connecting the hoses to their respective ports.

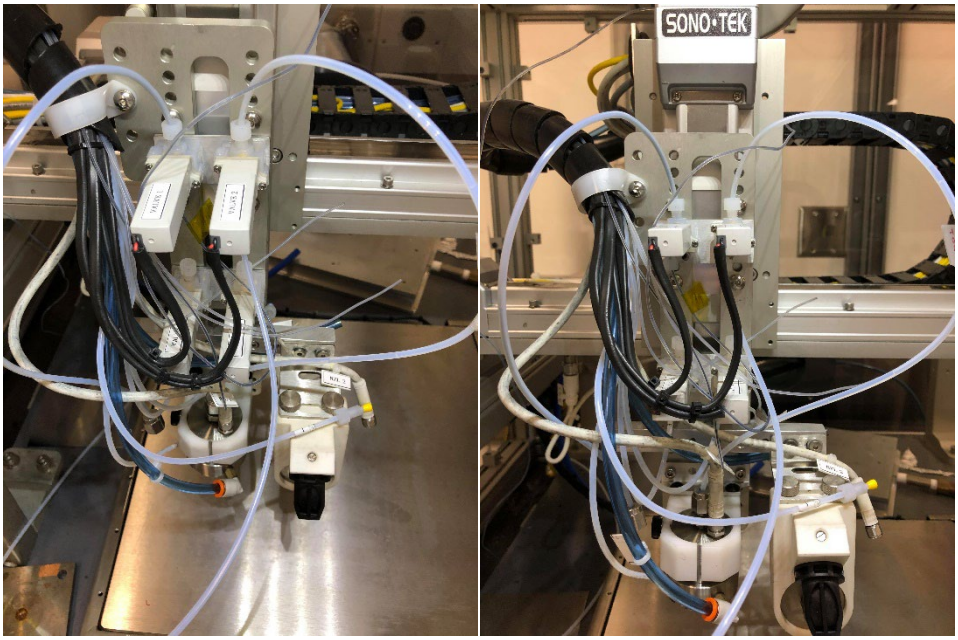

Figure B-1 Set-up of lines and nozzle in spray coater chamber.

Pre-cleaning

1. Place collection flask under nozzle to contain liquid.
2. Clean with **IPA 3x**
    a. Manual I/O in the Analog output (tab) in the software.
    b. Open ISO valve 2.
    c. Pump full syringe of IPA through line.
    d. Close ISO valve 2.
    e. After the last round, draw out all IPA remaining in line back into syringe, disconnect the syringe and clean with water (if water is the solvent).
3. Clean with solvent **(DI water) 3x**
    a. Repeat steps a to d in step 2.
    b. After last round, draw out all DI water remaining in line into syringe, disconnect the syringe and dry using a fibreless cloth.

Notes:

- For these steps, syringe is **controlled manually**. Move syringe back and forth to fully clean the nozzle and line.
- Make sure to close valve 2 before disconnecting line from syringe when refilling.
- Fill syringe to max 23mL, otherwise it will not fit in the mount.

Fabrication

1. Heat hot plate and PVDF membrane to 130°C. Once this temperature is reached, weigh the membrane.
2. Tape down aluminum foil over hot plate. Sandwich the PVDF membrane between two aluminum foil masks and ensure good alignment. Centre the PVDF-mask sandwich on the

hotplate, as shown in Figure B-2a. Place weights around metal frame to hold it in place. Place a flask in top corner (x_{max},y_{max}).

3. Load the syringe with aqueous PEDOT:PSS solution as shown in Figure B-2b
4. Specify number of coats (n) in "Saeedeh process 3" and load process. For n_{total}=20*, do initial run at n=5.
5. Ensure flow rate is set to 0.13mL/min on the manual control screen shown in Figure B-2b.
6. Initially run process dry to ensure nozzle moves correctly.
7. Run process wet with a fibreless cloth over the sample to ensure that the process and nozzle are working properly (ensure that there is no droplet at the end of the nozzle or PEDOT:PSS will not spray properly).
8. Record initial volume of PEDOT:PSS in the syringe.
9. Remove fibreless cloth and run the process wet.
10. Once finished flip membrane over and set up apparatus again. Run for n=20. Then flip over and run for n=15. (This is for n_{total} = 20 – adjust accordingly)

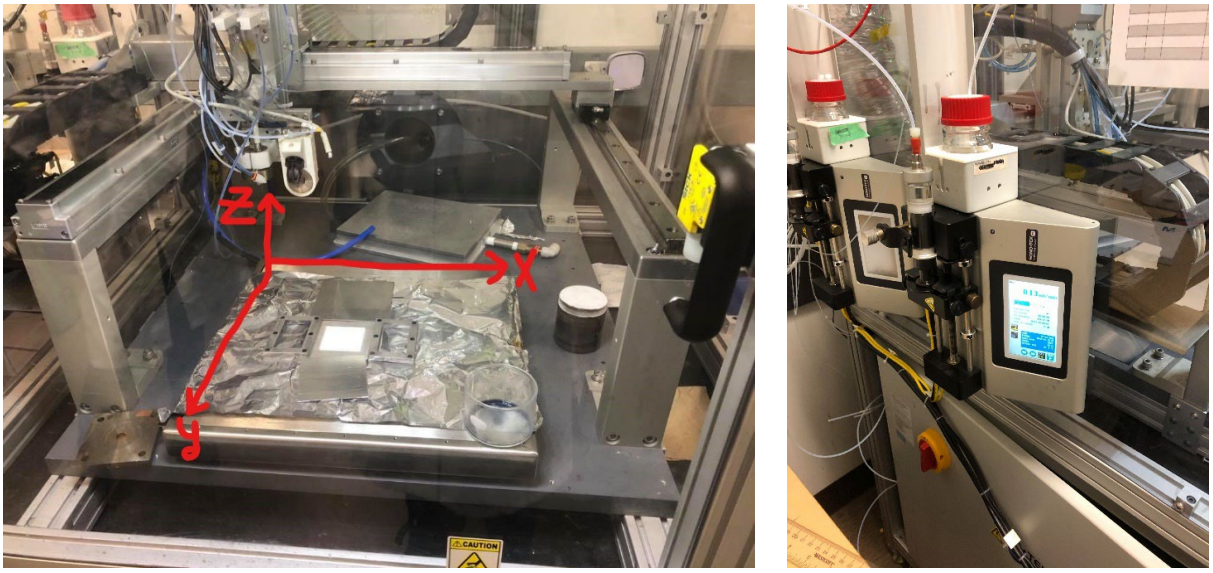

Figure B-2 a) Set-up of membrane on substrate in spray coater chamber. b) Syringe and manual pump set-up.

11. After deposition, weigh the PEDOT:PSS/PVDF:PEDOT:PSS while hot. Record final volume pumped into the syringe.

Post-Cleaning and Shutdown

1. Turn off the heater
2. Manual I/O, withdraw the remaining PEDOT:PSS solution from the tubes with syringe pump.
3. Perform spray coater pre-cleaning in reverse (3x DI water followed by 3x IPA).
4. After Final IPA pass run automated cleaning process **(nozzel2 valve1 cleaning)** before drawing IPA from line.
5. Click Home, then **safe shutdown**.
6. Clean and sanitize all experiment equipment and surfaces.

B.2 Displacement-Frequency Response

B.2.1 Equipment Specification

- Controller model: Keyence LK-G3001P
- Laser Model: Keyence LK-G32
- Software: Keyence LK-Navigator
- Displacement sensitivity = 50-nm
- Frequency sensitivity = 50 kHz

B.2.2 Laser Senser Set-up

1. Connect laser to controller and plug controller USB into computer. **Laser should be connected to head A on the controller.**
2. Connect controller to power (**order of start-up is very important because computer grounds controller, do not connect to power if controller is not connected to sensor, if you need to disconnect sensor and controller, always unplug from power source first**).

3. Clamp the laser in the stand, as shown in Figure B-3.
4. Clamp CP tri-layer cantilever beam between gold contacts and position it such that the actuator is within the range of the sensor at maximum +/- displacements. The light on controller turns green when the object is centered in range and solid yellow when detectable but off center. The numbers on the controller display are green when the sensor can detect an object. Figure 0-3 shows this experimental set-up.
5. The peak-peak displacement of the actuator must remain within the detectable range of the sensor. Actuate the device at a low frequency (i.e. ~0.1 Hz) to ensure the sensor records the full period.
6. Use duct tape and double-sided sticky tape to hold the stage and clamp in place, respectively.

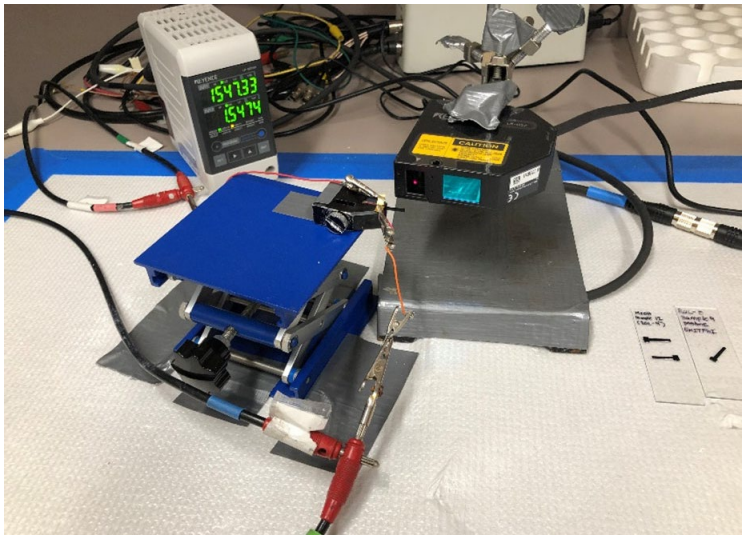

Figure B-3 Experimental set-up of displacement sensor.

B.2.3 ZPlot Set-up for Displacement Measurements

Displacement measurements are performed using a two-electrode set-up. The tri-layer device actuates under the application of sinusoidal voltage at constant frequency.

1. Connect the working electrode (WE) and counter electrode (CE) to their corresponding reference electrodes (RE) and connect each electrode to the gold contacts using small alligator clips.
2. Measure the contact resistance at each contact point using a multimeter. High contact resistance can result from salt contamination and oxide build-up on the clips and significantly affect results. Additionally, ensure that there is no connection between the gold contacts in the clamp; this results in current leakage.
3. EIS is applied using ZPlot to control the Solartron.
4. Perform displacement measurements at [0.01, 0.02, 0.04, 0.07, 0.1, 0.2, 0.4, 0.7, 1, 2, 4, 7, 10, 20, 40, 70, 100, 110, 120, 140, 170, and 200] Hz or until displacement amplitude is below the detectable limit of the laser sensor (~50-nm). Additionally, as the device approaches resonance frequency, increase the frequency measurements by increments of 1 to 5 Hz. For example, the resonance frequency of pristine PEDOT:PSS actuators is ~80 Hz; therefore measure peak-peak displacement at 65-95 Hz increasing by increments of 5 Hz.

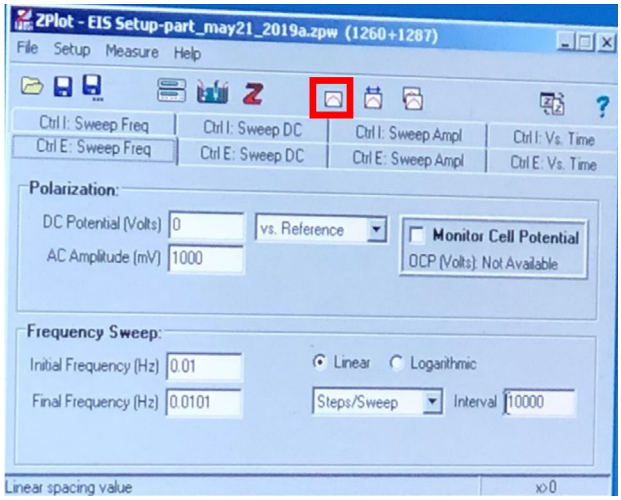

Figure B-4 ZPlot – EIS setup for displacement measurements at 0.01 Hz. Frequency increases in increments each test, all other parameters are held constant throughout displacement measurements. Apply voltage using linear step/sweep. Interval value is not particularly important (set to value >1000).

5. Run the EIS by clicking on the button indicated by the red box in Figure B-4. The program takes several seconds to load.

B.2.4. LK-Navigator Set-up

LK-Navigator is the GUI that controls the laser displacement sensor.

1. Before recording data go to the OUT1 tab and under “Display, Analog(N)” ensure that the minimum display unit (Y) is set to 0.01 µm (Figure 0-6a). Under the common settings tab, set the “Sample cycle(A)” to 20-µs (Figure B-5b).

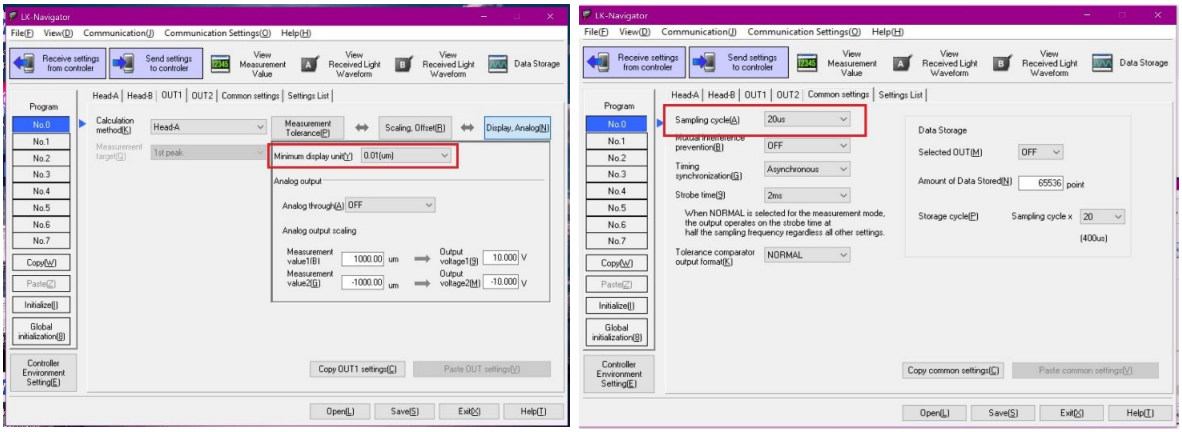

Figure B-5 a) Minimum display unit setting in LK-Navigator. b) Sample cycle setting in LK-Navigator.

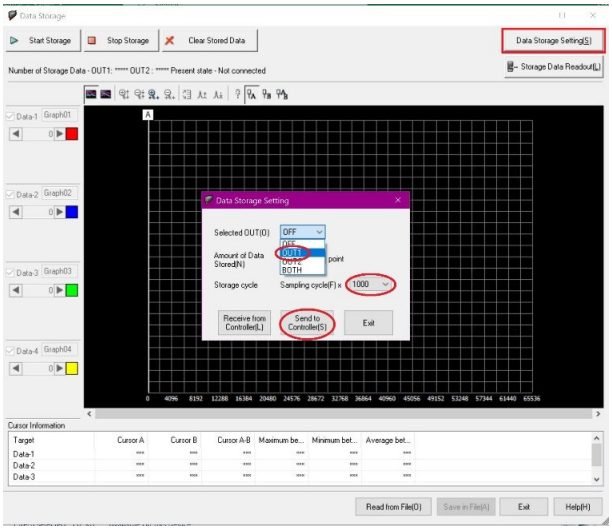

Figure B-6 Adjust data storage settings. 1. Select OUT1 in selected OUT(0) dropdown menu. For low frequency measurements, set storage cycle to 1000x and progressively decrease value as frequency increases. All setting changes must be manually sent to controller.

2. Select “Data Storage’ button in the top right corner. Select OUT1 from the “Selected OUT(0) drop down menu. Adjust storage cycling based on the actuation frequency such that data is recorded as a smooth and continuous sine wave. **All setting adjustments must be manually sent to the controller** (Figure B-6).
3. Select “Start Storage” to begin recording data. The software can store a maximum of 65,536 data points and will automatically stop recording at this point. Pressing “Stop Storage” stops recording data manually. The actuators can undergo hysteresis, so it is recommended to record multiple full cycles.
4. Select “Storage Data Redout(L)” then “Readout(R)” to display data from OUT1. A/B cursors can be adjusted to determine the peak-peak displacement of the actuators, as shown in Figure B-7. Select “Save in File(A)” to save the raw data. Clear the stored data before starting the next measurement.

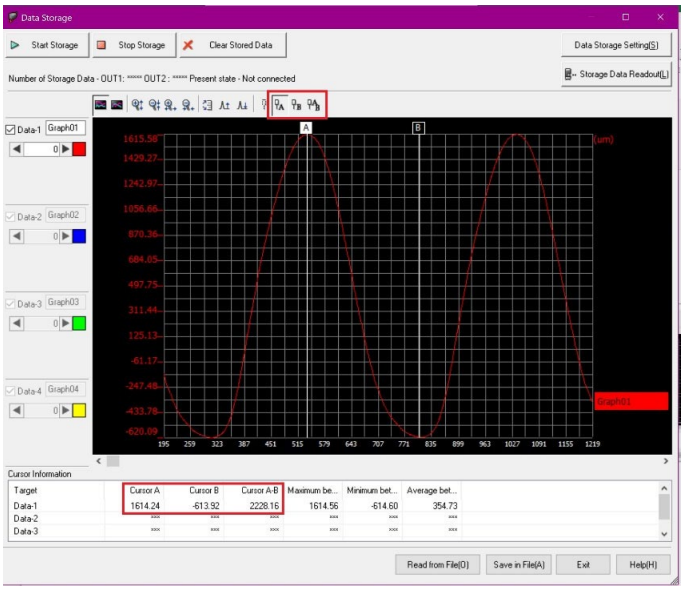

Figure B-7 LK-Navigator data analysis interface to determine the peak-to-peak displacement using the A/B cursor.

Appendix C : Supplementary Results

In Appendix C, we present supplemental results and figures.

C.1 Fabrication

We observed that while polar solvents improved the electrical and ionic properties of PEDOT:PSS films, they could also cause structural damage to the tri-layers. Figure C-1a shows samples treated with DMSO that delaminated. Figure C-1b shows a DMSO-treated sample that failed during uniaxial tensile testing described in Section 3.1.1.

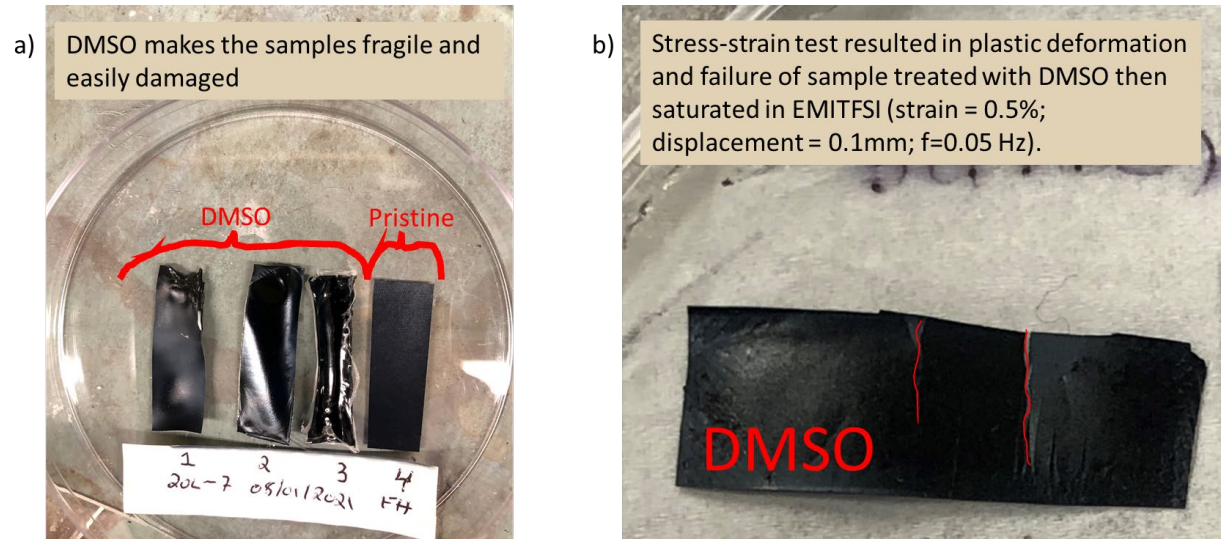

Figure C-1 Treatment with DMSO causes delamination and decreases the structural integrity of PEDOT:PSS/PVDF/PEDOT:PSS tri-layer actuators.

C.2 Ionic Conductivity

In This section we show supplementary figures for Galvanostatic ionic conductivity measurements described in Section 2.6.

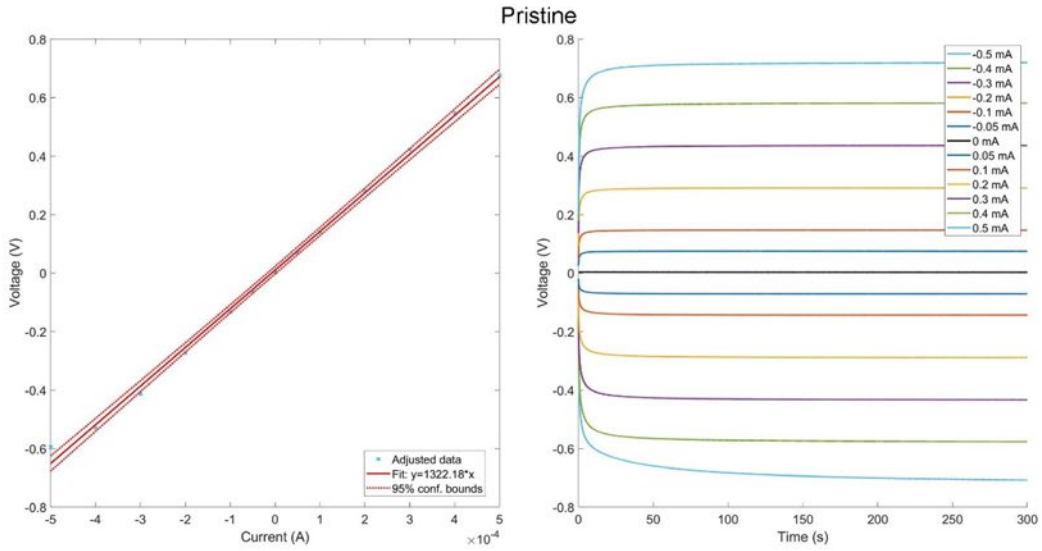
Pristine
Voltage (V)
Current (A)
×10^-4
Adjusted data
Fit: y=1322.18*x
95% conf. bounds
Time (s)
-0.5 mA
-0.4 mA
-0.3 mA
-0.2 mA
-0.1 mA
-0.05 mA
0 mA
0.05 mA
0.1 mA
0.2 mA
0.3 mA
0.4 mA
0.5 mA

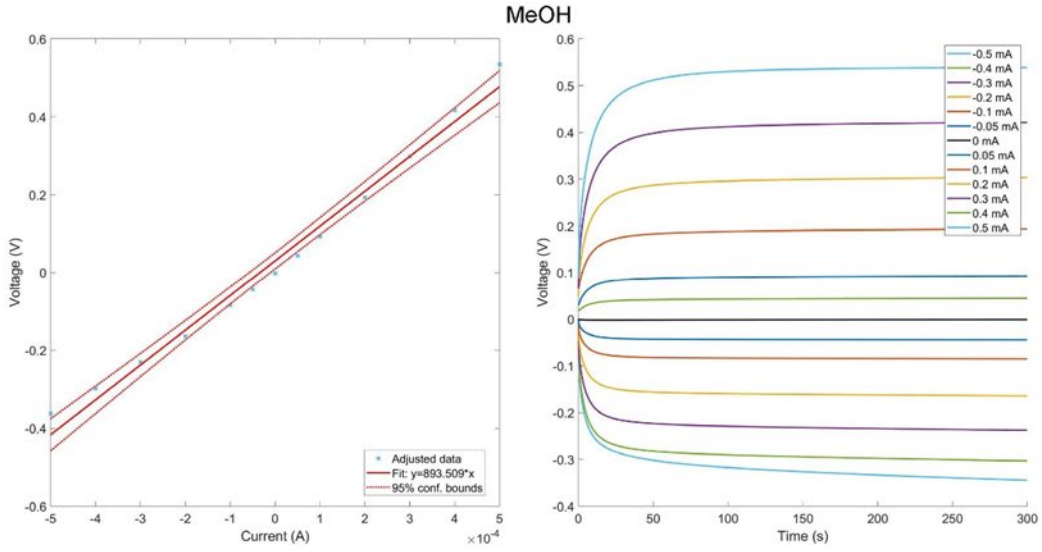
MeOH
Voltage (V)
Current (A)
×10^-4
Adjusted data
Fit: y=893.509*x
95% conf. bounds
Time (s)
-0.5 mA
-0.4 mA
-0.3 mA
-0.2 mA
-0.1 mA
-0.05 mA
0 mA
0.05 mA
0.1 mA
0.2 mA
0.3 mA
0.4 mA
0.5 mA

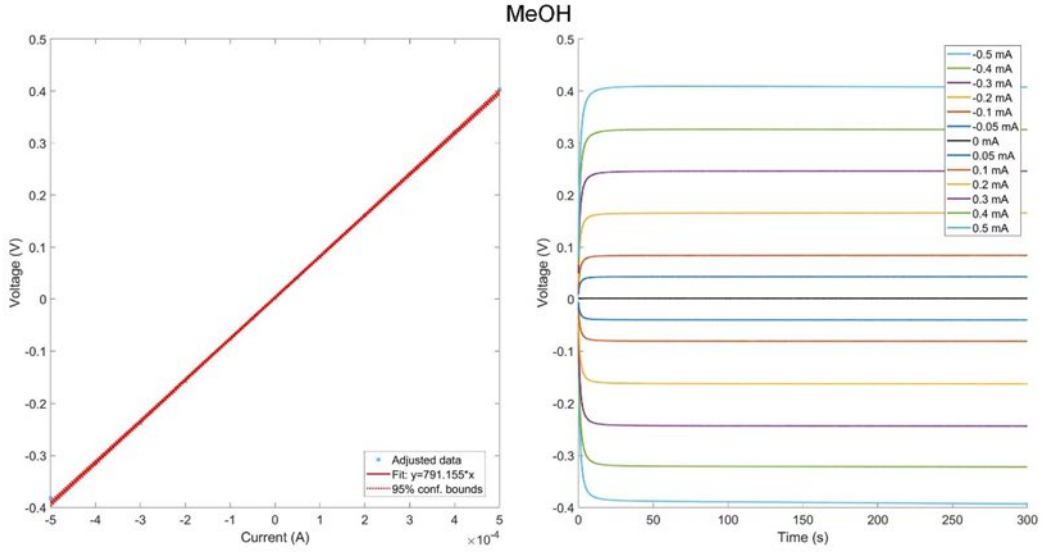
MeOH
Voltage (V)
Current (A)
×10^-4
Adjusted data
Fit: y=791.155*x
95% conf. bounds
Time (s)
-0.5 mA
-0.4 mA
-0.3 mA
-0.2 mA
-0.1 mA
-0.05 mA
0 mA
0.05 mA
0.1 mA
0.2 mA
0.3 mA
0.4 mA
0.5 mA

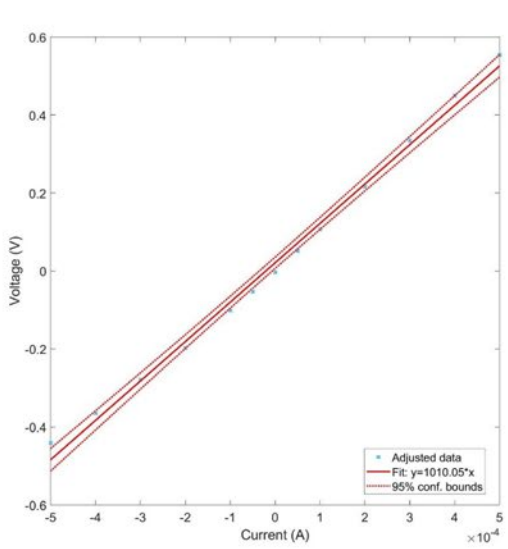
Voltage (V)
Current (A)
×10^-4
Adjusted data
Fit: y=1010.05*x
95% conf. bounds

EG

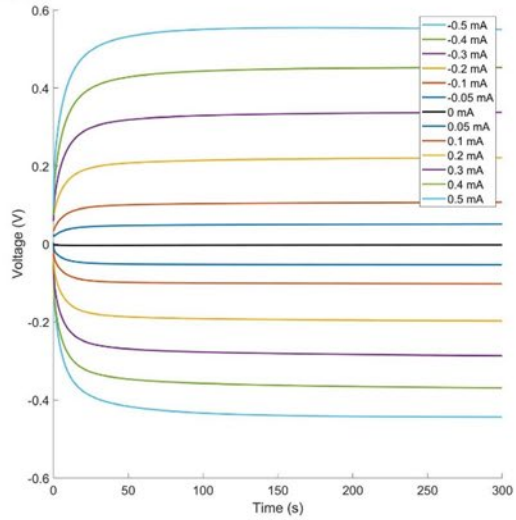
Voltage (V)
Time (s)
-0.5 mA
-0.4 mA
-0.3 mA
-0.2 mA
-0.1 mA
-0.05 mA
0 mA
0.05 mA
0.1 mA
0.2 mA
0.3 mA
0.4 mA
0.5 mA

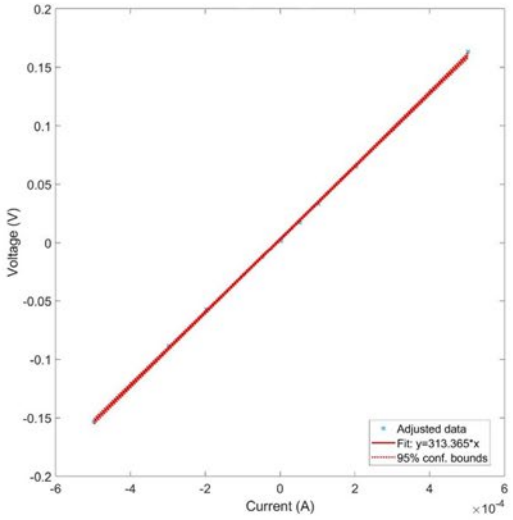
Voltage (V)
Current (A)
×10^-4
Adjusted data
Fit: y=313.365*x
95% conf. bounds

EG

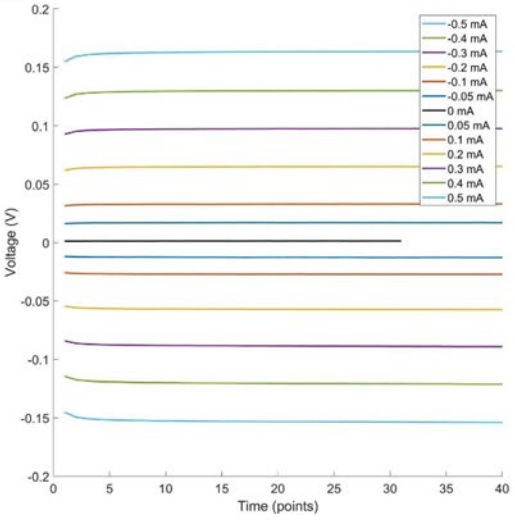
Voltage (V)
Time (points)
-0.5 mA
-0.4 mA
-0.3 mA
-0.2 mA
-0.1 mA
-0.05 mA
0 mA
0.05 mA
0.1 mA
0.2 mA
0.3 mA
0.4 mA
0.5 mA

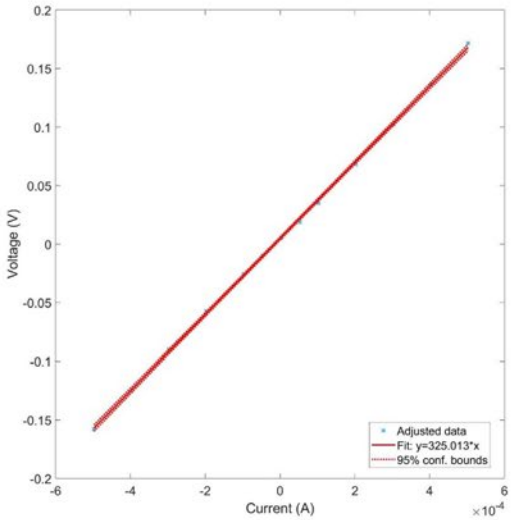
Voltage (V)
Current (A)
×10^-4
Adjusted data
Fit: y=325.013*x
95% conf. bounds

EG

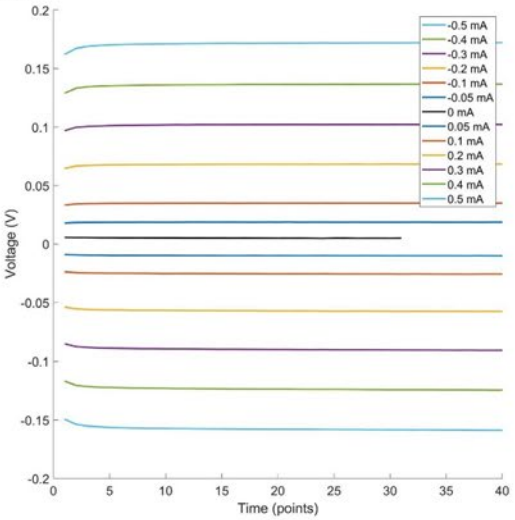
Voltage (V)
Time (points)
-0.5 mA
-0.4 mA
-0.3 mA
-0.2 mA
-0.1 mA
-0.05 mA
0 mA
0.05 mA
0.1 mA
0.2 mA
0.3 mA
0.4 mA
0.5 mA

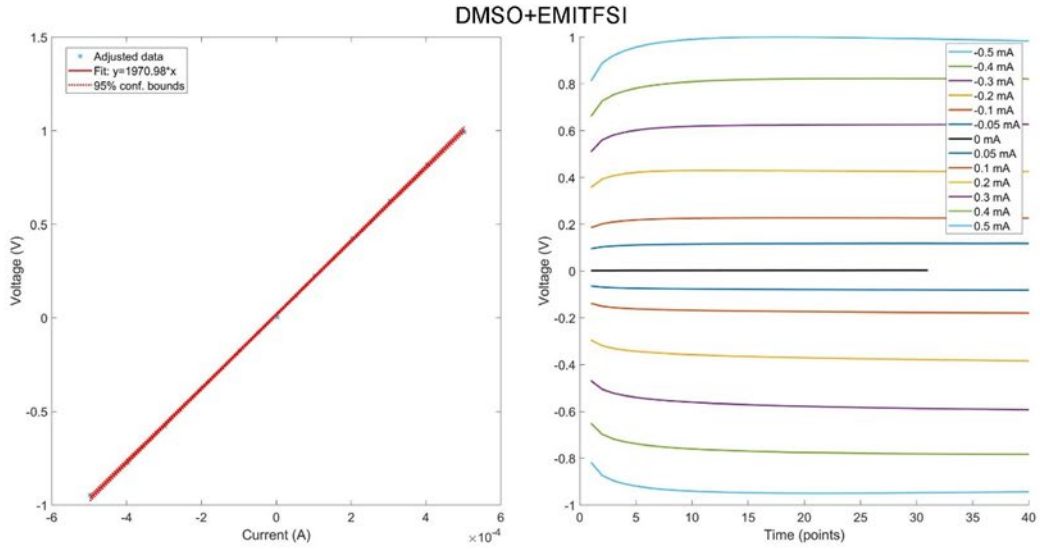
DMSO+EMITFSI
Adjusted data
Fit: y=1970.98*x
95% conf. bounds
Voltage (V)
Current (A)
×10^-4
-0.5 mA
-0.4 mA
-0.3 mA
-0.2 mA
-0.1 mA
-0.05 mA
0 mA
0.05 mA
0.1 mA
0.2 mA
0.3 mA
0.4 mA
0.5 mA
Time (points)

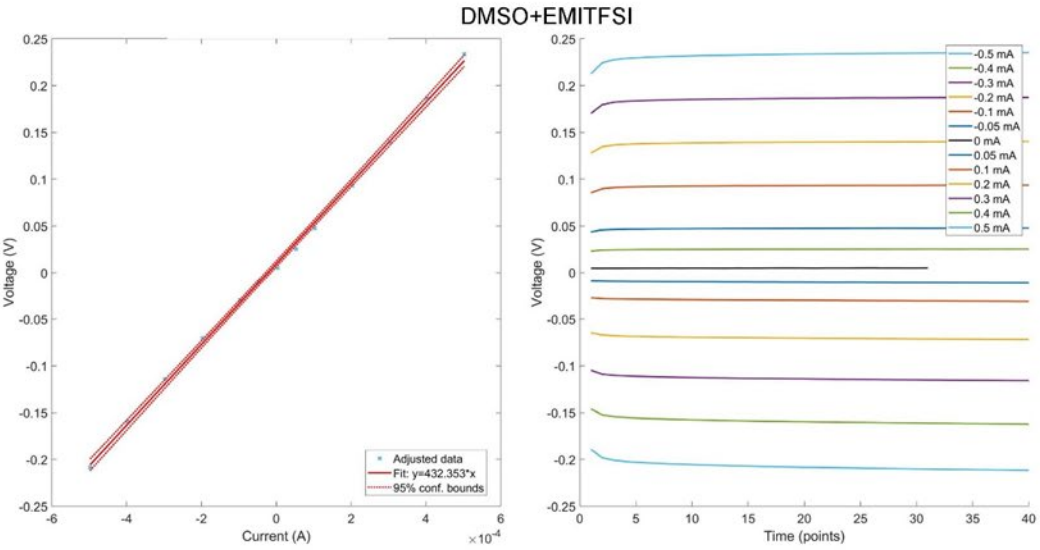
DMSO+EMITFSI
Adjusted data
Fit: y=432.353*x
95% conf. bounds
Voltage (V)
Current (A)
×10^-4
-0.5 mA
-0.4 mA
-0.3 mA
-0.2 mA
-0.1 mA
-0.05 mA
0 mA
0.05 mA
0.1 mA
0.2 mA
0.3 mA
0.4 mA
0.5 mA
Time (points)

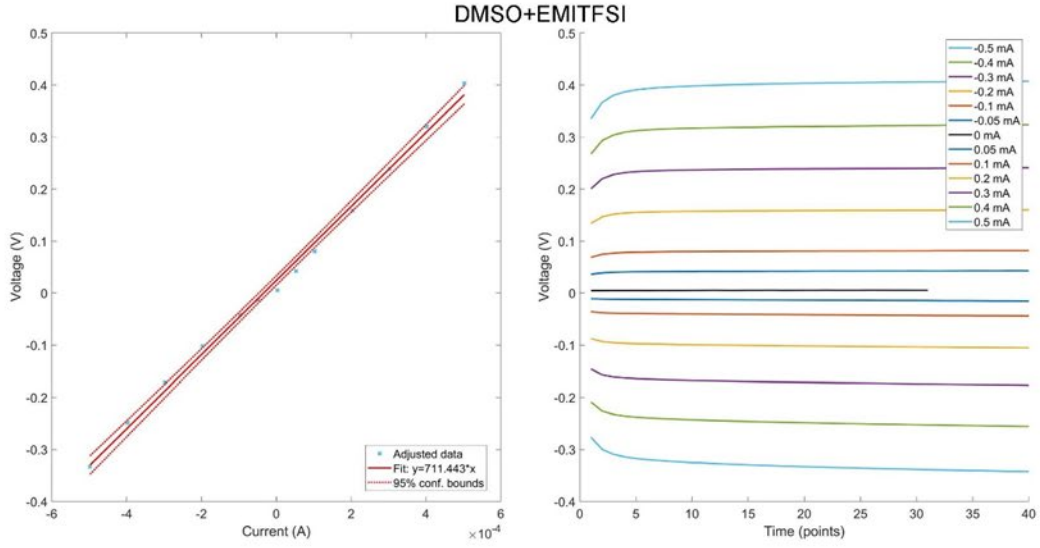
DMSO+EMITFSI
Adjusted data
Fit: y=711.443*x
95% conf. bounds
Voltage (V)
Current (A)
×10^-4
-0.5 mA
-0.4 mA
-0.3 mA
-0.2 mA
-0.1 mA
-0.05 mA
0 mA
0.05 mA
0.1 mA
0.2 mA
0.3 mA
0.4 mA
0.5 mA
Time (points)

DMSO

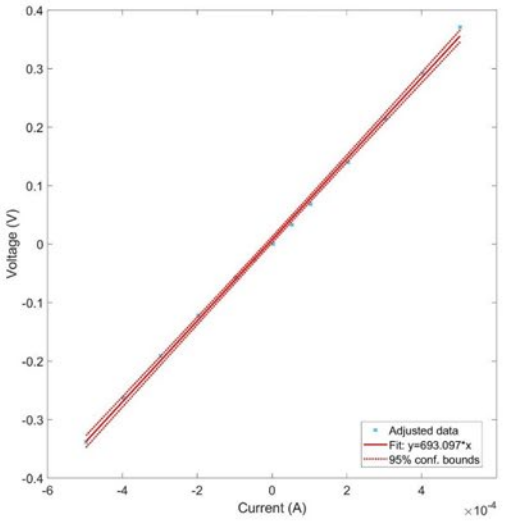

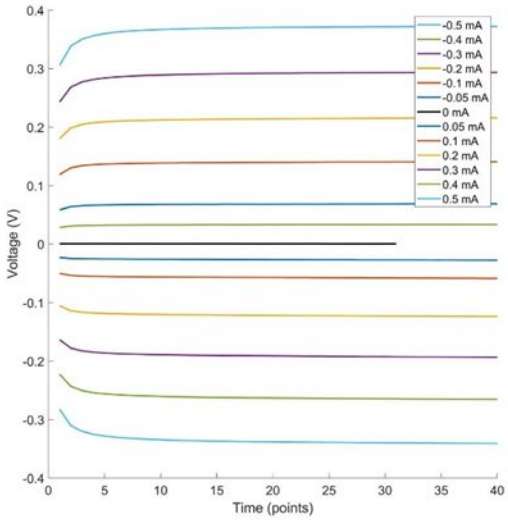

DMSO

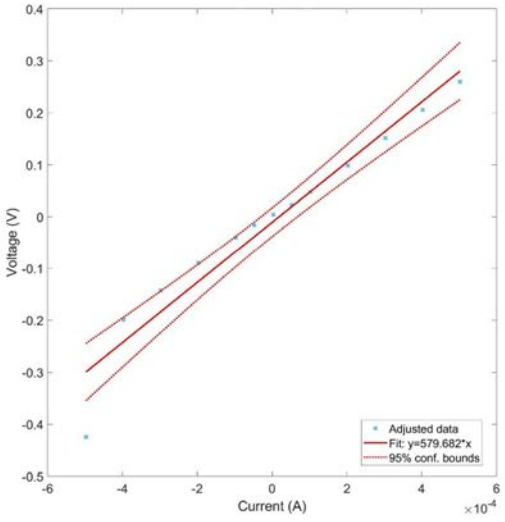

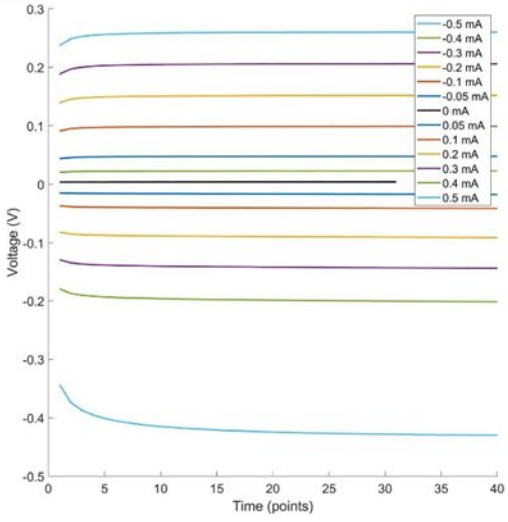

DMSO

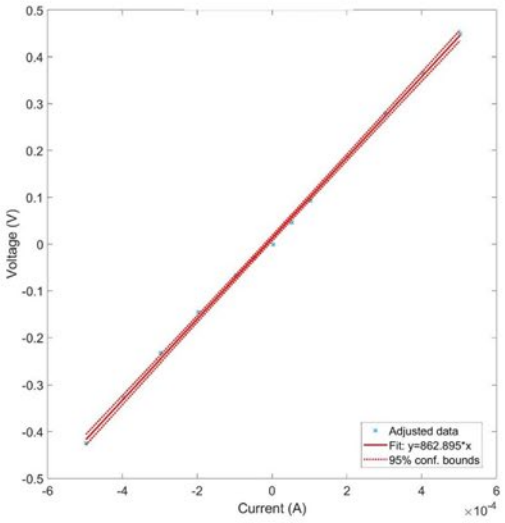

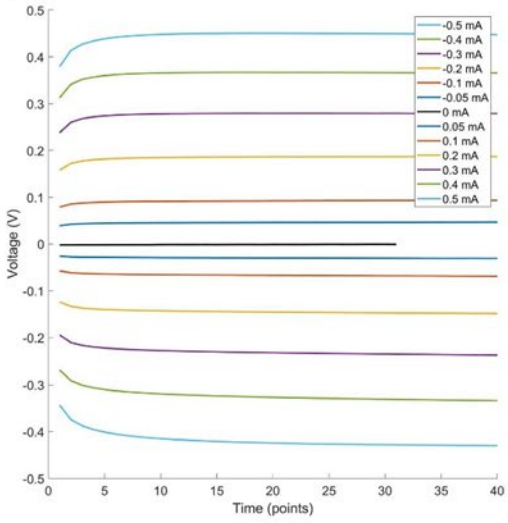

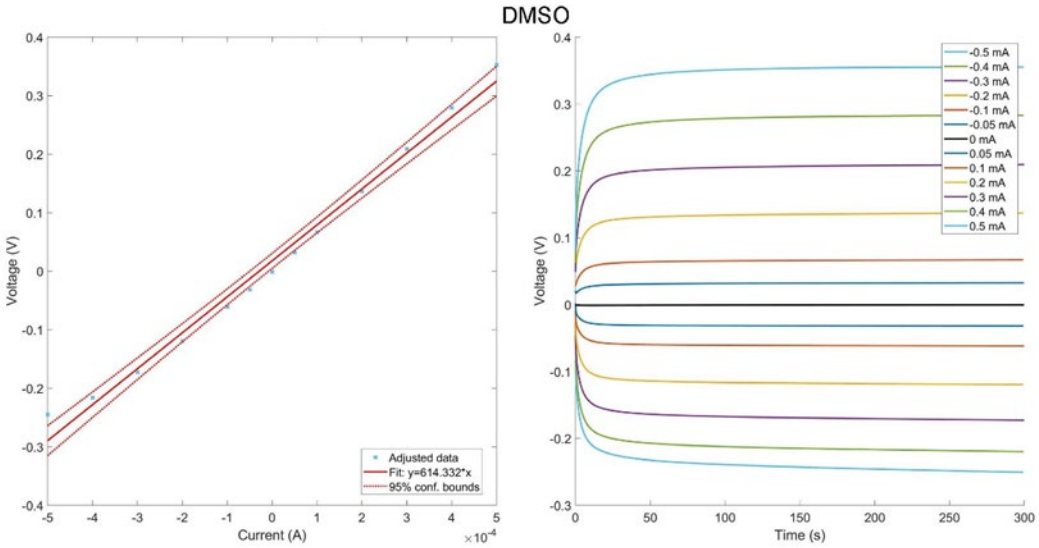

Figure C-2 Galvanostatic ionic conductivity measurements of Pristine, MeOH, EG, DMSO+EMITFSI, and DMSO samples.

C.3 Mechanical Testing

Here, we show the linear force-displacement curves we obtained from uniaxial tensile measurements, described in Section 3.1.2. We determined stiffness from the slope of these curves.

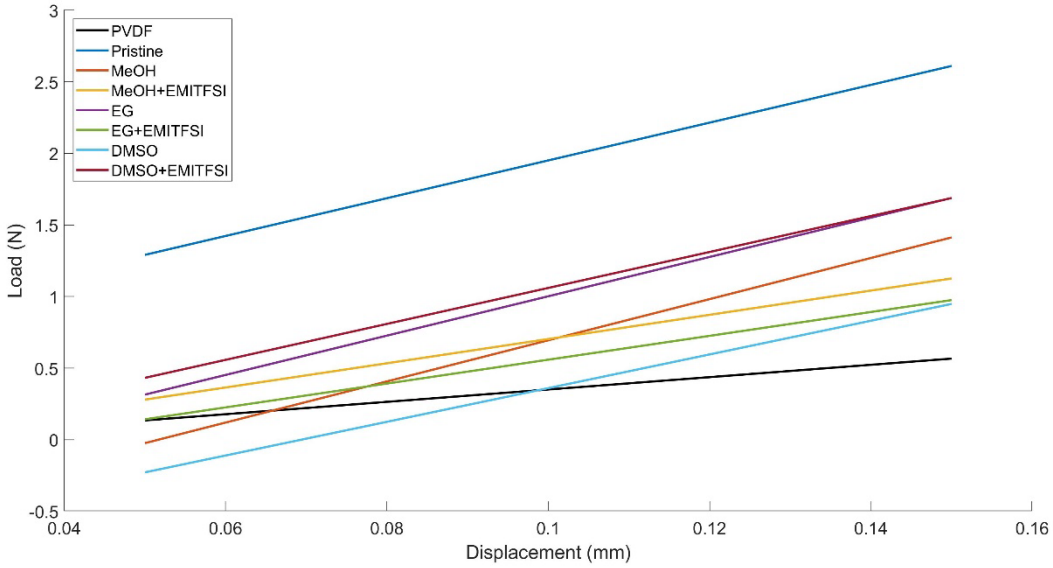

Figure C-3 Stiffness curve generated from tensile loading measurement using a Bose ElectroForce®-3100 system in tension mode (a strain of 0.5% at 0.1 Hz for 5 cycles).

C.4 XPS Supplementary Figures

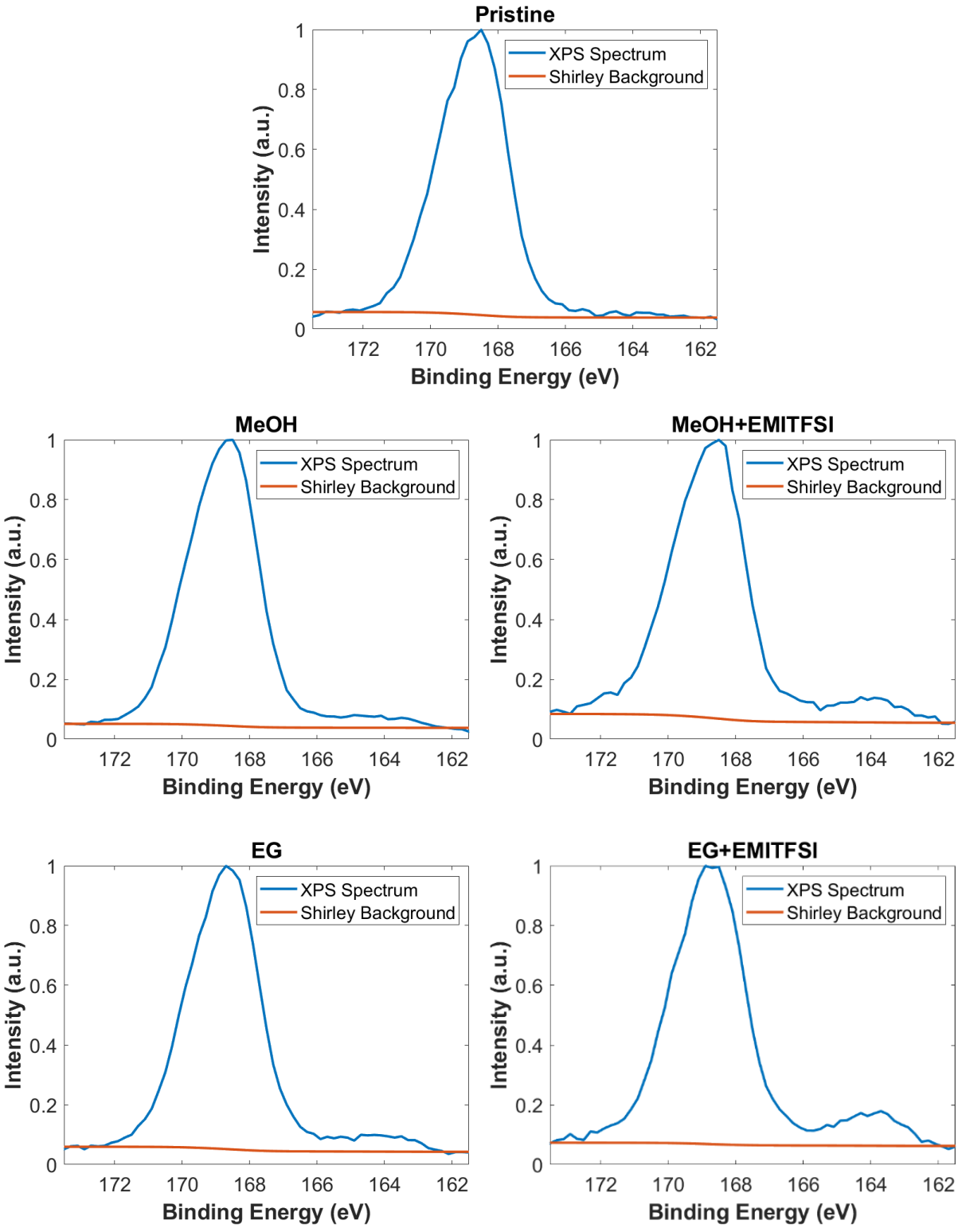

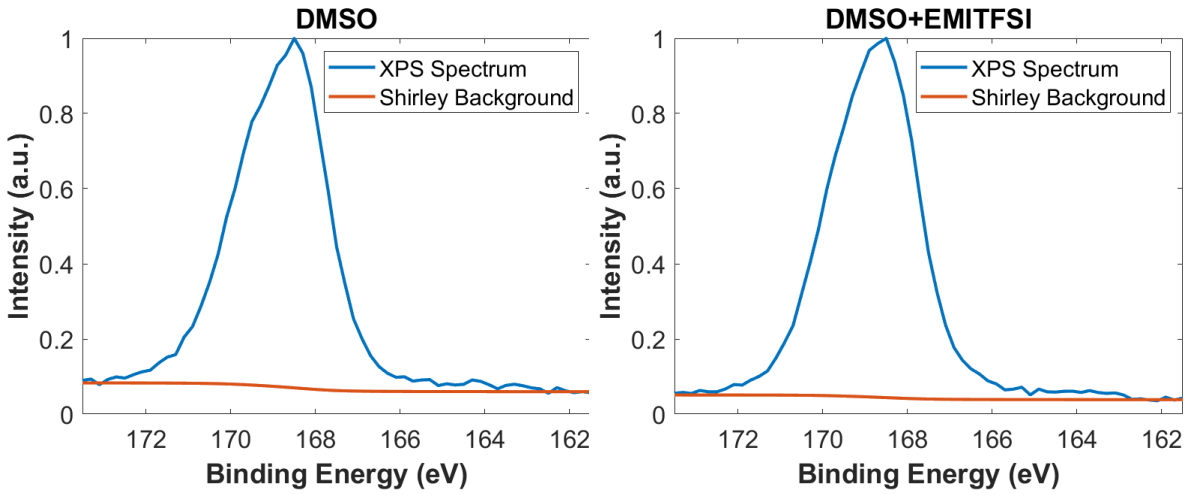

Figure C-4 Raw XPS data normalized to intensity (a.u.) from [0 1] plotted with Shirley Background for a) Pristine b) MeOH c) MeOH+EMITFSI d) EG e) EG+EMITFSI f) DMSO g) DMSO+EMITFSI.

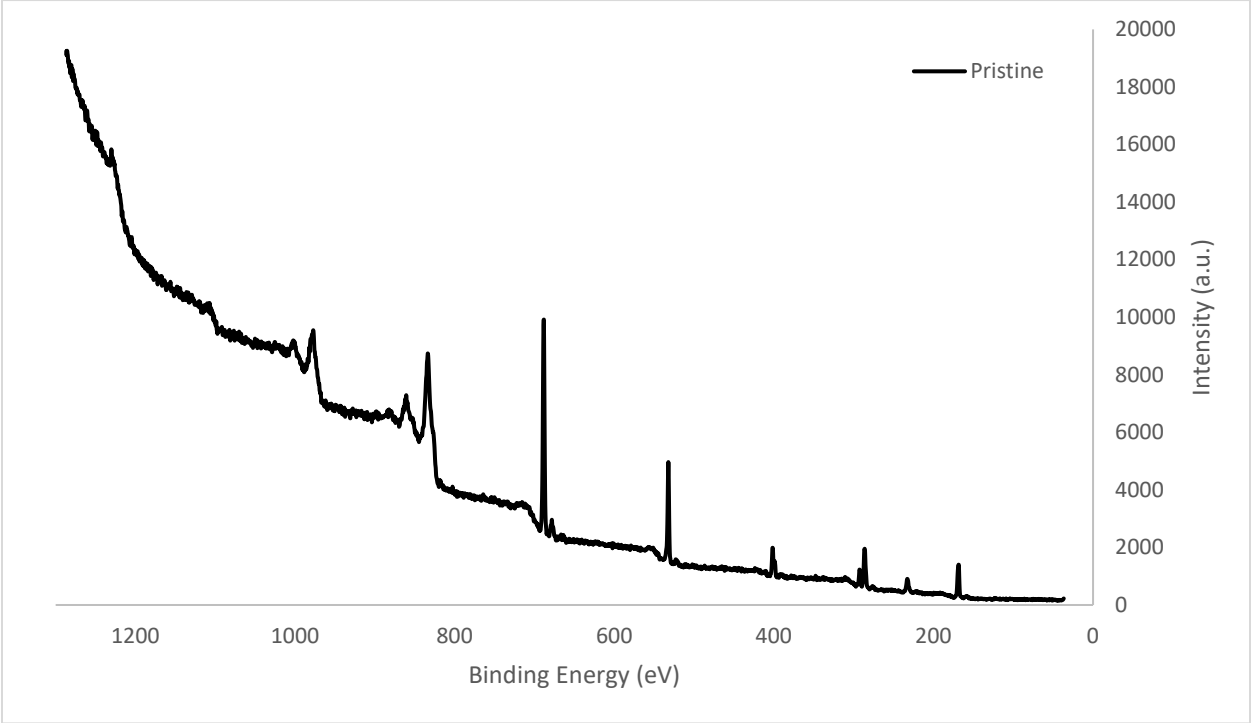

Figure C-5 Example of a broad spectrum XPS sweep for the Pristine PEDOT:PSS/PVDF/PEDOT:PSS tri-layer actuator sample.

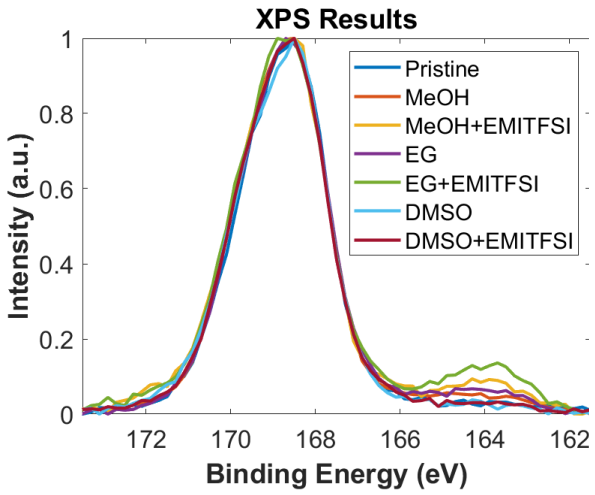
XPS Results
Intensity (a.u.)
Binding Energy (eV)
Pristine
MeOH
MeOH+EMITFSI
EG
EG+EMITFSI
DMSO
DMSO+EMITFSI

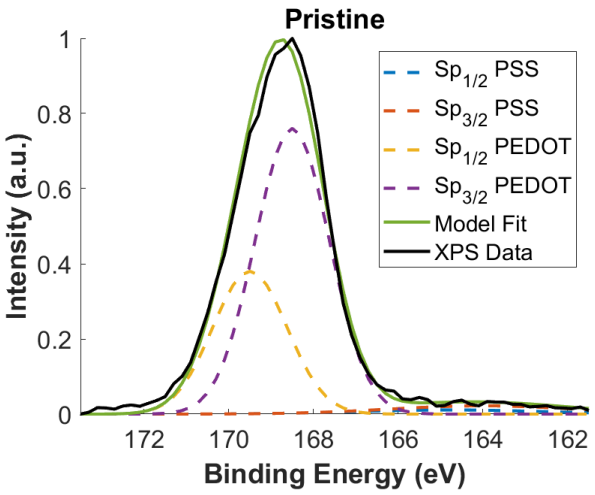
Pristine
Intensity (a.u.)
Binding Energy (eV)
Sp1/2 PSS
Sp3/2 PSS
Sp1/2 PEDOT
Sp3/2 PEDOT
Model Fit
XPS Data

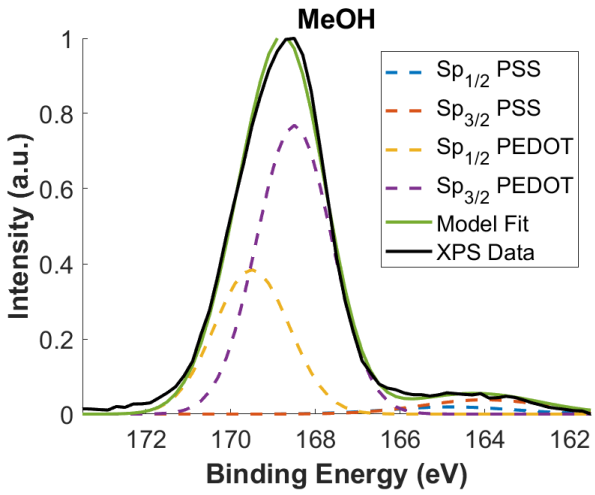
MeOH
Intensity (a.u.)
Binding Energy (eV)
Sp1/2 PSS
Sp3/2 PSS
Sp1/2 PEDOT
Sp3/2 PEDOT
Model Fit
XPS Data

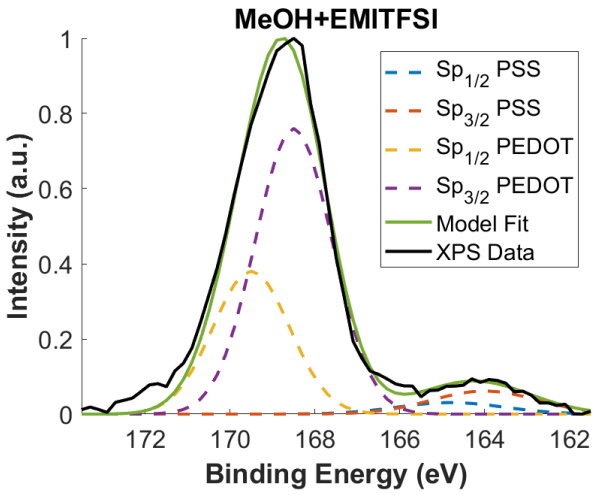
MeOH+EMITFSI
Intensity (a.u.)
Binding Energy (eV)
Sp1/2 PSS
Sp3/2 PSS
Sp1/2 PEDOT
Sp3/2 PEDOT
Model Fit
XPS Data

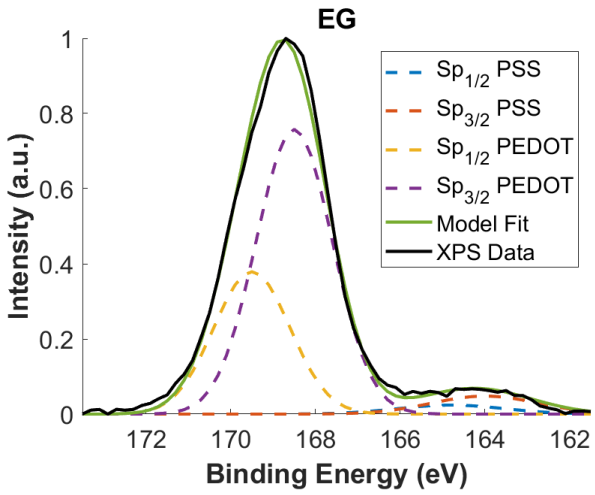
EG
Intensity (a.u.)
Binding Energy (eV)
Sp1/2 PSS
Sp3/2 PSS
Sp1/2 PEDOT
Sp3/2 PEDOT
Model Fit
XPS Data

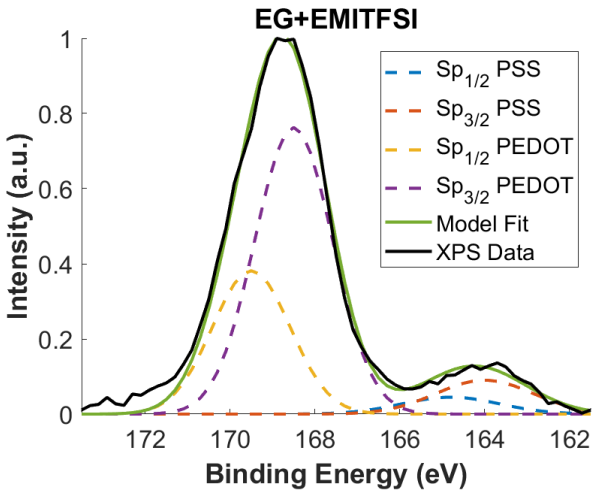
EG+EMITFSI
Intensity (a.u.)
Binding Energy (eV)
Sp1/2 PSS
Sp3/2 PSS
Sp1/2 PEDOT
Sp3/2 PEDOT
Model Fit
XPS Data

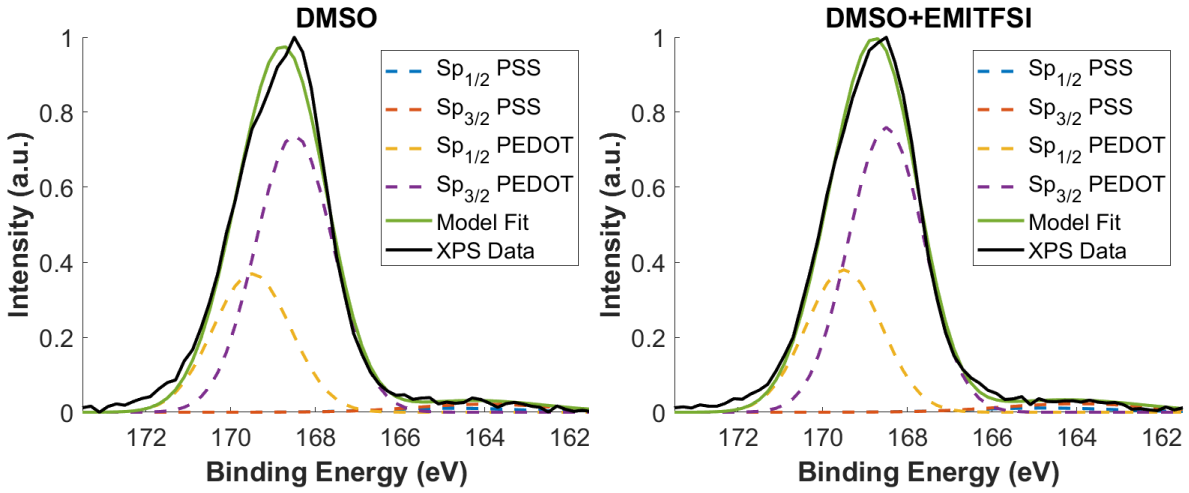

Figure C-6 a) XPS spectra results for untreated and post-treated samples. b-h) XPS spectra Gaussian model fit for S 2p in PEDOT:PSS. The peaks show two main chemical species, which are assigned to PSS^- (at 168.7 eV) and $PEDOT^+$ (164.7 eV). These peaks correspond to contributions from the spin orbitals S $2p_{3/2}$ and S $2p_{1/2}$ in a 2:1 ratio, respectively. The treatments analyzed include: b) Pristine, c) MeOH d) MeOH+EMITFSI, e) EG, f) EG+EMITFSI, g) DMSO, and h) DMSO+EMITFSI.

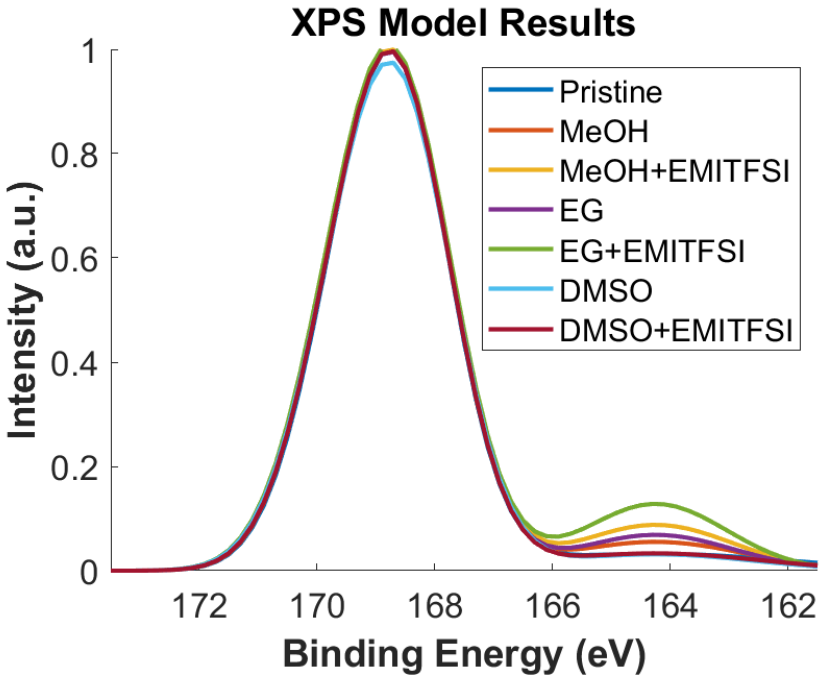

Figure C-7 Gaussian models fit to XPS spectra normalized to intensities values from [0 1], for untreated and treated PEDOT:PSS samples.

Appendix D : Modelling Supplementary Results

In this Appendix D we present the displacement-frequency response Actuatool model results.

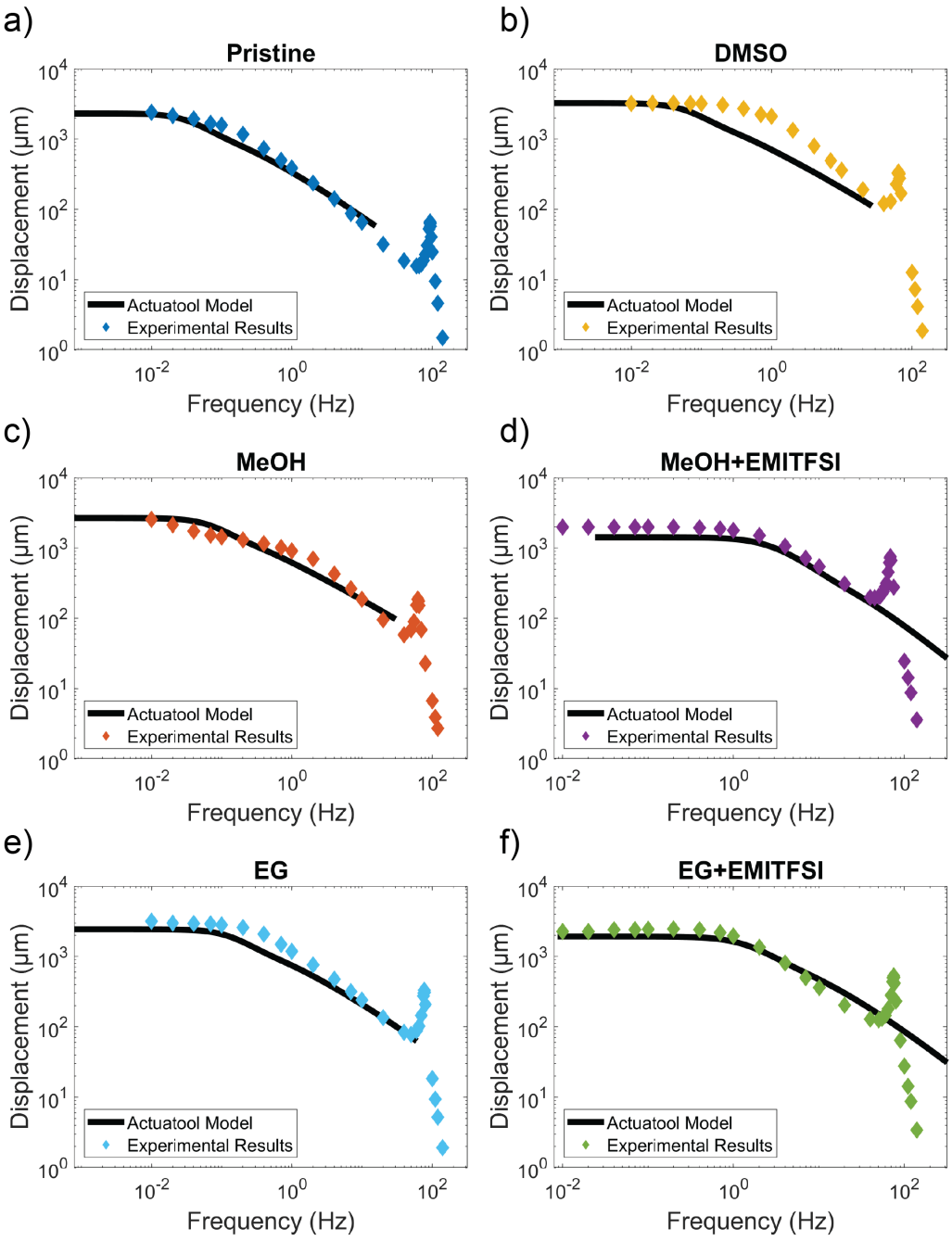

Figure D-1 Actuatool model comparison to displacement-frequency response.